Contributions to the Anisotropic Elasto-Plastic Analysis of Shells

by

Do-Nyun Kim

Bachelor of Science in Mechanical and Aerospace Engineering
Seoul National University, February 2000

Master of Science in Mechanical and Aerospace Engineering
Seoul National University, February 2002

Submitted to the Department of Mechanical Engineering
in partial fulfillment of the requirements for the degree of

Doctor of Philosophy in Mechanical Engineering

at the

MASSACHUSETTS INSTITUTE OF TECHNOLOGY

June 2009

Author ....
Department of Mechanical Engineering
May 16, 2009

Certified by ....
Klaus-Jürgen Bathe
Professor of Mechanical Engineering
Thesis Supervisor

Accepted by ....
David E. Hardt
Chairman, Department Committee on Graduate Students

Contributions to the Anisotropic Elasto-Plastic Analysis of Shells

by

Do-Nyun Kim

Submitted to the Department of Mechanical Engineering
on May 16, 2009, in partial fulfillment of the
requirements for the degree of
Doctor of Philosophy in Mechanical Engineering

Abstract

Shells are probably the most widely used structural component in engineering and also in nature due to their high efficiency and excellent performance when properly designed. On the other hand, they can be very sensitive to changes in geometries, thicknesses, applied loads and boundary conditions. Hence much research effort has been devoted to the reliable and efficient analysis of shells. This work contributes to the anisotropic elasto-plastic analysis of shells by addressing key issues in developing shell elements for finite element analysis and an elasto-plasticity model considering anisotropy and its evolution.

First we develop a shell element that models the three-dimensional (3D) effects of surface tractions. The element is the widely used MITC4 shell element enriched by the use of a fully 3D stress-strain description, appropriate through-the-thickness displacements to model surface tractions, and pressure degrees of freedom for incompressible analyses. The element formulation avoids instabilities and ill-conditioning.

We also develop a triangular 6-node shell element that represents an important improvement over a recently published element. The element is spatially isotropic, passes the membrane and bending patch tests, contains no spurious zero energy mode, and is formulated without an artificial constant. In particular, the improved element does not show the instability sometimes observed with the earlier published element.

Finally we review a constitutive model for anisotropic elasto-plastic analysis which takes into account the anisotropy of both the elastic and plastic material behaviors, as well as their evolution with plastic strains. It is based on continuum energy considerations, the Lee decomposition of deformations and a stored energy function of the logarithmic strains. The present work focuses on giving some physical insight into the parameters of the model and their effects on the predictions in proportional and in non-proportional loading conditions.

Thesis Supervisor: Klaus-Jürgen Bathe
Title: Professor of Mechanical Engineering

Acknowledgments

Thank God, my father in heaven, for giving me a wonderful opportunity to study at MIT and meet great people. You always leads me and my family into the right path. May your name be honored.

I would like to thank my thesis supervisor, Prof. Klaus-Jürgen Bathe, for his excellent support and encouragement throughout my doctoral research. His insight and passion for research and teaching have led me to the right places. In particular, he inspires me to be happy at myself, my work and my life under any circumstance.

I am thankful to my committee members, Prof. Tomasz Wierzbicki and Prof. Eduardo A. Kausel, for their valuable comments and suggestions. I am grateful to Prof. Francisco J. Montáns for his collaboration in anisotropic elasto-plasticity models and to Prof. Phill-Seung Lee for sharing his experiences in developing triangular shell elements.

I would also like to thank my colleagues in the Finite Element Research Group at MIT, Jared Craig Ahern, Samar Malek, Reza Sharifi Sedeh, Haining Zheng, and Christian Deilmann, for their help, encouragement and friendship. I appreciate help and friendship of Korean graduate students in MechE and Aero-Astro at MIT.

I am very thankful to friends and families in First Korean Church in Cambridge and especially to all those who have prayed for me even without knowing who I am.

I acknowledge that this work has been partially supported by Korea Science and Engineering Foundation and by John Oak Scholarship.

My utmost gratitude is due to my family. My special thanks go to my parents and brother for their endless love, support, encouragement and prayer whatever I do. I am also truly grateful to my parents-in-law and brothers- and sister-in-law for their priceless support and prayer. Special thanks are due to my precious daughter and son, Yeji and Yeil, for cheering me up through their world best smiles. I would like to give *my last and most valuable thanks to my wife, Hye-Lim*, for her unconditional love, sacrifice, trust, support and encouragement.

Contents

List of Figures

List of Tables

Introduction

Thin-walled structures or shells are well recognized as a basic building block found abundantly in nature ranging from small to large scale systems. Shells carry applied loads in an impressively effective way while securing a relatively large space inside them in spite of their thinness and lightness.

Shells are probably the most widely used structural component in engineering practice. They, when properly designed, provide a comparatively light and large structure that can hold applied loads very effectively with a small amount of materials, i.e. at a low cost. However shells, especially thin shells, can be extremely sensitive to imperfections and changes in geometries, thicknesses, applied loads and boundary conditions. Hence a reliable analysis is the key to design an effective shell structure.

To a large extent, shell structures are now solved in practice using finite element procedures since it is almost impossible to obtain solutions analytically when the geometry and boundary conditions of shells are not simple. The finite element analysis of shells has now matured to the extent that it sometimes seems any complex shell can be accurately analyzed. In fact, however, there are still a number of outstanding difficulties. These relate to the development of more effective shell finite elements, the design of better contact algorithms to accurately model frictional forces applied on a shell's top and bottom surfaces, as needed for example in metal forming analysis, and the development of better constitutive models for existing and new materials, just to name a few only.

The present work focuses on the anisotropic elasto-plastic analysis of shells by addressing key issues in obtaining improved shell elements for finite element analysis and an elasto-plasticity model considering anisotropy and its evolutions.

In chapter 1, we present a shell element that models the three-dimensional (3D) effects of surface tractions, like needed when a shell is confined between other solid media. The element is the widely used MITC4 shell element enriched by the use of a fully 3D stress-strain description, appropriate through-the-thickness displacements to model surface tractions, and pressure degrees of freedom for incompressible analyses. The element formulation avoids instabilities and ill-conditioning. Various example solutions are presented to illustrate the capabilities of the element.

In chapter 2, we present a triangular 6-node shell element that represents an important improvement over a recently published element [1]. The shell element is formulated, like the original element, using the MITC procedure. The element has the attributes to be spatially isotropic, to pass the membrane and bending patch tests, to contain no spurious zero energy mode, and is formulated without an artificial constant. In particular, the improved element does not show the instability sometimes observed with the earlier published element. We give the convergence behavior of the element in discriminating membrane- and bending-dominated benchmark problems. These tests show the effectiveness of the element.

In chapter 3, we review a constitutive model for anisotropic elasto-plastic analysis which takes into account the anisotropy of both the elastic and plastic material behaviors, as well as their evolution with plastic strains. The model is based on continuum energy considerations, the Lee decomposition of elastic and plastic deformations and a stored energy function of the logarithmic strains. We give some physical insight into the parameters of the model and their effects on the predictions in both proportional and in non-proportional loading conditions.

Finally we present our conclusions.

Chapter 1

A 4-node 3D-shell element to model shell surface tractions and incompressible behavior

The finite element analysis of shells has now matured to the extent that it sometimes seems any complex shell can be accurately analyzed. In fact, however, there are still a number of outstanding difficulties. These relate to the more accurate modeling of shell structures to include 3D effects, the development of still more effective shell finite elements, in particular triangular elements, and the mathematical analyses to ensure optimality of the finite element solutions [2, 6]. To a large extent, shell structures are now solved in practice using 4-node shell elements. Among those available, the MITC4 shell element is probably the most effective element, in particular when linear and nonlinear analyses are to be performed [2, 6–10]. However, the other MITC shell elements can be more effective for specific analyses [1, 9, 11, 12].

The formulation of the MITC4 shell element is based on the Reissner-Mindlin assumptions of "material fibers originally straight and normal to the shell mid-surface do not stretch and remain straight" and "zero stress normal to the shell mid-surface" [2, 6]. The MITC elements can be formulated using a continuum representation or the 'basic shell model' identified by Chapelle and Bathe [2, 6, 13, 14]. While the Reissner-Mindlin assumptions are widely applicable, they cannot model the application of shell surface stresses as needed in the analysis of a shell confined between solid media. For example, in metal forming, the normal and shear tractions applied to thin sheet surfaces can be large and the accurate modeling of normal stresses and shear stresses can be important. Of course, in addition, large strain elastic-plastic (almost incompressible) conditions need be represented.

To model the effects of surface tractions, it appears that 3D shell-solid elements are most appropriate, see [15–19] and the references therein. In the formulation of these elements, the top and bottom surfaces of the shell are represented geometrically and their positions are updated through the displacement degrees of freedom, just like in a fully 3D analysis of solids but with only one element layer through the shell thickness [2, 6]. Since the bending strains vary linearly, clearly, for consistency with bending theory including the Poisson ratio coupling, the through-the-thickness normal strain must also be allowed to vary linearly. This requires a quadratic interpolation of displacements through the shell thickness. The shear, membrane and pinching locking can be relieved using MITC strain interpolations.

While sometimes effective, these elements display severe ill-conditioning when the shell becomes thin and when the shell is an (almost) incompressible medium [20, 21]. To improve the element behavior and computational effectiveness, instead of displacement degrees of freedom, enhanced strains have been used, see for example Refs. [15, 22, 23], and the references therein. However, enhanced strain formulations can be unstable, see Refs. [24,25], and are therefore best avoided. Hence, a more effective approach is to build on the basic MITC4 shell element, for which all shell actions are represented using the shell mid-surface, use the three-dimensional stress-strain description, and enrich the shell element formulation 'judiciously' by appropriate displacement and pressure interpolations. These interpolations need to be selected to not introduce instabilities or ill-conditioning. This approach was used in Ref. [26] to enrich the MITC4 shell element by two element degrees of freedom corresponding to thickness stretching (a constant and a linear term) in order to represent large strain effects.

The objective in this chapter is to present the MITC4 shell element enriched by the

3D stress-strain law, and by displacements and pressure used to represent accurately the effects of shell surface normal and tangential tractions, and incompressible conditions. The enrichment in displacements is achieved by simply adding displacement interpolations with corresponding degrees of freedom at the 4 nodes. The resulting displacements are compatible across element boundaries. To render the element also applicable to (almost) incompressible conditions, the u/p formulation with an assumption on the pressure is used [6]. All these degrees of freedom, including the pressure degrees of freedom, can be invoked hierarchically as desired. This hierarchical feature of the element is very attractive, obviously from a modeling point of view, but also from a practical point of view. Namely, the pre- and post-processing capabilities of the classical MITC4 element are directly applicable by simply increasing the number of degrees of freedom allowed for the element.

The element presented in this chapter is largely based on concepts previously published but in this chapter we have synthesized various ideas in an aim to obtain an overall effective formulation. In particular, this 3D-shell element formulation does not show ill-conditioning. In the following sections, we first present the formulation of the continuum shell model, then the finite element discretization, and finally we give the results of various illustrative example solutions.

1.1 The shell model

In this section, we present the shell model that we will solve by our finite element discretization. We follow the notation used in Ref. [6].

The initial geometry at time 0 is described by

$$ {}^{0}\vec{x} = {}^{0}\vec{x}_M + \frac{\xi}{2}\, {}^{0}a\, {}^{0}\vec{V}_n \tag{1.1} $$

where ξ is the natural coordinate in the thickness direction, ${}^{0}\vec{x}_M$ is the position vector of material particles in the shell mid-surface, ${}^{0}a$ is the thickness and ${}^{0}\vec{V}_n$ is the director vector.

In the deformed configuration, an initially straight fiber may be curved with the assumption shown in Figs. 1-1 and 1-2. The assumed deformed geometry at time t is

$$\begin{aligned} {}^{t}\vec{x} = {}^{t}\vec{x}_M + \frac{\xi}{2}\,{}^{t}a\,{}^{t}\vec{V}_n + \xi^2\,{}^{0}a\,{}^{t}Q_n\,{}^{t}\vec{V}_n \\ + \xi^2\,{}^{0}a\left({}^{t}Q_1\,{}^{t}\vec{V}_1 + {}^{t}Q_2\,{}^{t}\vec{V}_2\right) \\ + \xi^3\,{}^{0}a\left({}^{t}C_1\,{}^{t}\vec{V}_1 + {}^{t}C_2\,{}^{t}\vec{V}_2\right) \end{aligned} \tag{1.2}$$

Here ${}^{t}\vec{V}_n$ is the director vector at time t, ${}^{t}a$ is the shell thickness at time t, ${}^{t}\vec{V}_1$ and ${}^{t}\vec{V}_2$ are are unit vectors orthogonal to ${}^{t}\vec{V}_n$ and to each other, ${}^{t}Q_n$ is the degree of freedom corresponding to a quadratic displacement function in the direction ${}^{t}\vec{V}_n$, and ${}^{t}Q_\alpha$ and ${}^{t}C_\alpha$ represent degrees of freedom corresponding to quadratic and cubic displacement functions in the directions ${}^{t}\vec{V}_\alpha$, with $\alpha = 1, 2$. The left superscripts 0 and t always denote that a quantity is given at time 0 and t. With these assumptions, the fiber originally normal to the mid-surface can strain linearly and become curved, and the transverse shear stresses have a quadratic distribution through the shell thickness. This enables the element to precisely capture the effect of in-plane tractions, like normal and frictional forces, applied on the top and bottom shell surfaces. Note that ${}^{0}a$, the initial thickness, is employed in front of each higher order function. This is a scaling factor in order to avoid ill-conditioning of the global stiffness matrix as the thickness becomes small. It is more natural to use the current thickness but we use the initial thickness because this leads to a simpler formulation.

In the same way, the deformed geometry at time $t + \Delta t$ is defined by

$$\begin{aligned} {}^{t+\Delta t}\vec{x} = {}^{t+\Delta t}\vec{x}_M + \frac{\xi}{2}\,{}^{t+\Delta t}a\,{}^{t+\Delta t}\vec{V}_n + \xi^2\,{}^{0}a\,{}^{t+\Delta t}Q_n\,{}^{t+\Delta t}\vec{V}_n \\ + \xi^2\,{}^{0}a\left({}^{t+\Delta t}Q_1\,{}^{t+\Delta t}\vec{V}_1 + {}^{t+\Delta t}Q_2\,{}^{t+\Delta t}\vec{V}_2\right) \\ + \xi^3\,{}^{0}a\left({}^{t+\Delta t}C_1\,{}^{t+\Delta t}\vec{V}_1 + {}^{t+\Delta t}C_2\,{}^{t+\Delta t}\vec{V}_2\right) \end{aligned} \tag{1.3}$$

From these geometric positions, we can obtain the corresponding incremental dis-

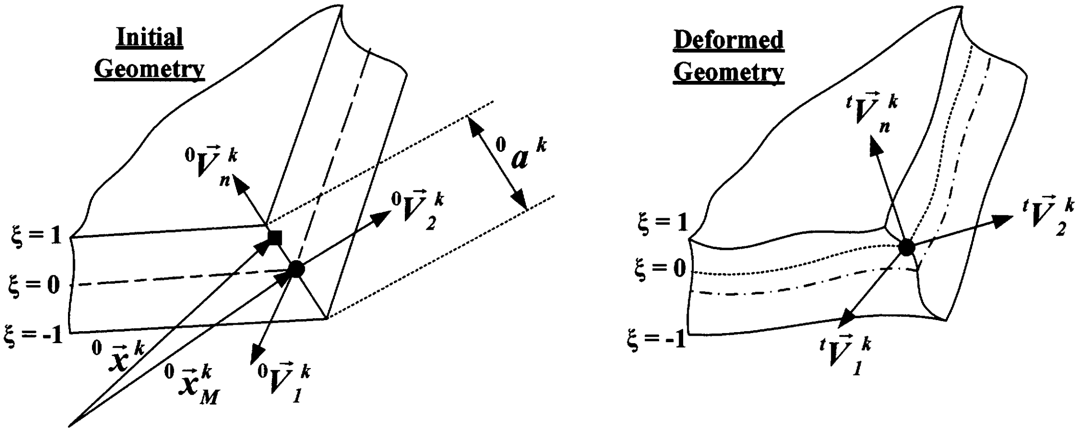

Figure 1-1: Shell geometries in the initial and deformed configurations.

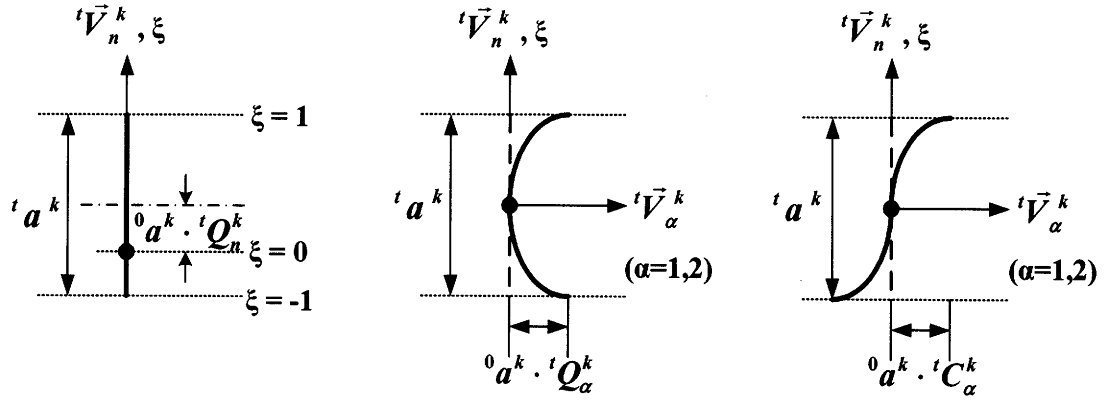

Figure 1-2: The quadratic and cubic displacement functions at node k.

placement field as follows.

$$\vec{u} = {}^{t+\Delta t}\vec{u} - {}^{t}\vec{u} = {}^{t+\Delta t}\vec{x} - {}^{t}\vec{x} \tag{1.4}$$

Then we have

$$\begin{aligned}\vec{u} = \left({}^{t+\Delta t}\vec{x}_M - {}^{t}\vec{x}_M\right) &+ \frac{\xi}{2}\left({}^{t+\Delta t}a\ {}^{t+\Delta t}\vec{V}_n - {}^{t}a\ {}^{t}\vec{V}_n\right) + \xi^2\ {}^{0}a\left({}^{t+\Delta t}Q_n\ {}^{t+\Delta t}\vec{V}_n - {}^{t}Q_n\ {}^{t}\vec{V}_n\right)\\ &+\xi^2\ {}^{0}a\left({}^{t+\Delta t}Q_1\ {}^{t+\Delta t}\vec{V}_1 - {}^{t}Q_1\ {}^{t}\vec{V}_1\right) + \xi^2\ {}^{0}a\left({}^{t+\Delta t}Q_2\ {}^{t+\Delta t}\vec{V}_2 - {}^{t}Q_2\ {}^{t}\vec{V}_2\right)\\ &+\xi^3\ {}^{0}a\left({}^{t+\Delta t}C_1\ {}^{t+\Delta t}\vec{V}_1 - {}^{t}C_1\ {}^{t}\vec{V}_1\right) + \xi^3\ {}^{0}a\left({}^{t+\Delta t}C_2\ {}^{t+\Delta t}\vec{V}_2 - {}^{t}C_2\ {}^{t}\vec{V}_2\right)\end{aligned} \tag{1.5}$$

This field can be expressed in terms of degrees of freedom at time t for the incremental displacements using the following relations.

$${}^{t+\Delta t}\vec{x}_M - {}^{t}\vec{x}_M = \vec{u}_M = u\vec{e}_1 + v\vec{e}_2 + w\vec{e}_3 \tag{1.6a}$$

$${}^{t+\Delta t}a - {}^{t}a = {}^{0}a \cdot \Delta_a \tag{1.6b}$$

$${}^{t+\Delta t}Q_n - {}^{t}Q_n = q_n \tag{1.6c}$$

$${}^{t+\Delta t}Q_1 - {}^{t}Q_1 = q_1 \tag{1.6d}$$

$${}^{t+\Delta t}Q_2 - {}^{t}Q_2 = q_2 \tag{1.6e}$$

$${}^{t+\Delta t}C_1 - {}^{t}C_1 = c_1 \tag{1.6f}$$

$${}^{t+\Delta t}C_2 - {}^{t}C_2 = c_2 \tag{1.6g}$$

Here Eq. (1.6a) represents three translations in the global Cartesian coordinate system given by the unit vectors $\vec{e}_i$, with $i = 1, 2, 3$, Eq. (1.6b) gives a thickness change and Eqs. (1.6c)–(1.6g) define displacement increments. Note that, in Eq. (1.6b), the incremental thickness change is normalized by the initial thickness to circumvent ill-conditioning.

For the shell element, two rotational degrees of freedom have been generally used to describe the rotation of a director vector. We, instead, adopt three rotational degrees of freedom at this point and use

$$
\begin{aligned}
{}^{t+\Delta t}\vec{V}_n - {}^{t}\vec{V}_n &\simeq \left(\frac{1}{2}\gamma\alpha + \beta\right){}^{t}\vec{V}_1 + \left(\frac{1}{2}\beta\gamma - \alpha\right){}^{t}\vec{V}_2 - \frac{1}{2}\left(\alpha^2 + \beta^2\right){}^{t}\vec{V}_n && \text{(1.7a)}\\
{}^{t+\Delta t}\vec{V}_1 - {}^{t}\vec{V}_1 &\simeq \left(\frac{1}{2}\alpha\beta + \gamma\right){}^{t}\vec{V}_2 + \left(\frac{1}{2}\gamma\alpha - \beta\right){}^{t}\vec{V}_n - \frac{1}{2}\left(\beta^2 + \gamma^2\right){}^{t}\vec{V}_1 && \text{(1.7b)}\\
{}^{t+\Delta t}\vec{V}_2 - {}^{t}\vec{V}_2 &\simeq \left(\frac{1}{2}\beta\gamma + \alpha\right){}^{t}\vec{V}_n + \left(\frac{1}{2}\alpha\beta - \gamma\right){}^{t}\vec{V}_1 - \frac{1}{2}\left(\gamma^2 + \alpha^2\right){}^{t}\vec{V}_2 && \text{(1.7c)}
\end{aligned}
$$

where α, β and γ are the incremental rotations about the vectors ${}^{t}\vec{V}_1$, ${}^{t}\vec{V}_2$ and ${}^{t}\vec{V}_n$, respectively. Once we have obtained α, β and γ, the director vectors are updated with the following relationship.

$$
{}^{t+\Delta t}\vec{V}_i = \mathbb{Q}\ {}^{t+\Delta t}\vec{V}_i \quad (i = 1, 2, n) \tag{1.8}
$$

where

$$
\begin{aligned}
\mathbb{Q} &= \mathbb{I} + \frac{\sin\theta}{\theta}\mathbb{S} + \frac{1}{2}\left(\frac{\sin(\theta/2)}{\theta/2}\right)^2 \mathbb{S}^2 && \text{(1.9a)}\\
\theta &= \sqrt{\alpha^2 + \beta^2 + \gamma^2} && \text{(1.9b)}\\
\mathbb{S} &= \begin{bmatrix} 0 & -\gamma & \beta \\ \gamma & 0 & -\alpha \\ -\beta & \alpha & 0 \end{bmatrix} && \text{(1.9c)}
\end{aligned}
$$

Note that Eqs. (1.7) are obtained from Eqs. (1.8) and (1.9). Using Eqs. (1.6) and (1.7) with Eq. (1.5), the incremental displacement field becomes

$$
\vec{u} = \vec{u}_L + \vec{u}_Q \tag{1.10}
$$

where $\vec{u}_L$ and $\vec{u}_Q$ denote the linear and quadratic terms of incremental displacements, respectively,

$$\begin{aligned}\vec{u}_L = \vec{u}_M &+ \frac{\xi}{2}\left({}^0a\ {}^t\vec{V}_n\ \Delta_a - {}^ta\ {}^t\vec{V}_2\ \alpha + {}^ta\ {}^t\vec{V}_1\ \beta\right) + \xi^2\ {}^0a\left({}^t\vec{V}_n\ q_n - {}^tQ_n\ {}^t\vec{V}_2\ \alpha + {}^tQ_n\ {}^t\vec{V}_1\ \beta\right)\\ &+\xi^2\ {}^0a\left({}^t\vec{V}_1\ q_1 - {}^tQ_1\ {}^t\vec{V}_n\ \beta + {}^tQ_1\ {}^t\vec{V}_2\ \gamma\right) + \xi^2\ {}^0a\left({}^t\vec{V}_2\ q_2 - {}^tQ_2\ {}^t\vec{V}_1\ \gamma + {}^tQ_2\ {}^t\vec{V}_n\ \alpha\right)\\ &+\xi^3\ {}^0a\left({}^t\vec{V}_1\ c_1 - {}^tC_1\ {}^t\vec{V}_n\ \beta + {}^tC_1\ {}^t\vec{V}_2\ \gamma\right) + \xi^3\ {}^0a\left({}^t\vec{V}_2\ c_2 - {}^tC_2\ {}^t\vec{V}_1\ \gamma + {}^tC_2\ {}^t\vec{V}_n\ \alpha\right)\end{aligned} \tag{1.11}$$

$$\begin{aligned}\vec{u}_Q = &\frac{\xi}{2}\left[-{}^0a\ {}^t\vec{V}_2\ \Delta_a\ \alpha + {}^0a\ {}^t\vec{V}_1\ \Delta_a\ \beta + \frac{1}{2}{}^ta\ {}^t\vec{V}_2\ \beta\ \gamma + \frac{1}{2}{}^ta\ {}^t\vec{V}_1\ \gamma\ \alpha - \frac{1}{2}{}^ta\ {}^t\vec{V}_n\left(\alpha^2+\beta^2\right)\right]\\ &+\xi^2\ {}^0a\left[-{}^t\vec{V}_2\ q_n\ \alpha + {}^t\vec{V}_1\ q_n\ \beta + \frac{1}{2}{}^tQ_n\ {}^t\vec{V}_2\ \beta\ \gamma + \frac{1}{2}{}^tQ_n\ {}^t\vec{V}_1\ \gamma\ \alpha - \frac{1}{2}{}^tQ_n\ {}^t\vec{V}_n\left(\alpha^2+\beta^2\right)\right]\\ &+\xi^2\ {}^0a\left[-{}^t\vec{V}_n\ q_1\ \beta + {}^t\vec{V}_2\ q_1\ \gamma + \frac{1}{2}{}^tQ_1\ {}^t\vec{V}_n\ \gamma\ \alpha + \frac{1}{2}{}^tQ_1\ {}^t\vec{V}_2\ \alpha\ \beta - \frac{1}{2}{}^tQ_1\ {}^t\vec{V}_1\left(\beta^2+\gamma^2\right)\right]\\ &+\xi^2\ {}^0a\left[-{}^t\vec{V}_1\ q_2\ \gamma + {}^t\vec{V}_n\ q_2\ \alpha + \frac{1}{2}{}^tQ_2\ {}^t\vec{V}_1\ \alpha\ \beta + \frac{1}{2}{}^tQ_2\ {}^t\vec{V}_n\ \beta\ \gamma - \frac{1}{2}{}^tQ_2\ {}^t\vec{V}_2\left(\gamma^2+\alpha^2\right)\right]\\ &+\xi^3\ {}^0a\left[-{}^t\vec{V}_n\ c_1\ \beta + {}^t\vec{V}_2\ c_1\ \gamma + \frac{1}{2}{}^tC_1\ {}^t\vec{V}_n\ \gamma\ \alpha + \frac{1}{2}{}^tC_1\ {}^t\vec{V}_2\ \alpha\ \beta - \frac{1}{2}{}^tC_1\ {}^t\vec{V}_1\left(\beta^2+\gamma^2\right)\right]\\ &+\xi^3\ {}^0a\left[-{}^t\vec{V}_1\ c_2\ \gamma + {}^t\vec{V}_n\ c_2\ \alpha + \frac{1}{2}{}^tC_2\ {}^t\vec{V}_1\ \alpha\ \beta + \frac{1}{2}{}^tC_2\ {}^t\vec{V}_n\ \beta\ \gamma - \frac{1}{2}{}^tC_2\ {}^t\vec{V}_2\left(\gamma^2+\alpha^2\right)\right]\end{aligned} \tag{1.12}$$

The current shell model contains 12 parameters to describe the shell behavior: three translations, three rotations, one thickness change, three quadratic displacements and two cubic displacements. However, we now exclude the γ rotation effect in the above equations because the degree of freedom leads to spurious zero energy modes, even when the initially straight fiber transverse to the shell mid-surface has become curved. Consider the linear terms of the incremental displacements, $\vec{u}_L$, as arranged in Table 1.1. We see that the displacement corresponding to the γ rotation when a fiber is not straight can be described by the degrees of freedom q_1, q_2, c_1 and c_2. Therefore, the γ rotation is a redundant degree of freedom and can be set to zero when we use the higher-order in-plane displacements.

Table 1.1: The components of the linear incremental displacement given in Eq. (1.11)

	$\vec{u}_M$		
$\vec{u}_L$	$\xi/2$	${}^t\vec{V}_1$	$({}^ta)\beta$
		${}^t\vec{V}_2$	$-({}^ta)\alpha$
		${}^t\vec{V}_n$	$({}^0a)\Delta_a$
	$\xi^2\ {}^0a$	${}^t\vec{V}_1$	${}^tQ_n\beta - {}^tQ_2\gamma + q_1$
		${}^t\vec{V}_2$	$-{}^tQ_n\alpha + {}^tQ_1\gamma + q_2$
		${}^t\vec{V}_n$	$-{}^tQ_1\beta + {}^tQ_2\alpha + q_n$
	$\xi^3\ {}^0a$	${}^t\vec{V}_1$	$-{}^tC_2\gamma + c_1$
		${}^t\vec{V}_2$	${}^tC_1\gamma + c_2$
		${}^t\vec{V}_n$	$-{}^tC_1\beta + {}^tC_2\alpha$

1.2 Finite element discretization

We use the shell model given in the previous section for the finite element discretization.

1.2.1 Interpolation of geometry and displacement

To interpolate the shell geometry, the usual interpolation is used [6]

$$\begin{aligned} {}^t\vec{x}(r,s,\xi) = & \sum_{k=1}^{4} h_k(r,s)\,{}^t\vec{x}_M^k + \frac{\xi}{2}\sum_{k=1}^{4} h_k(r,s)\,{}^ta_k\,{}^t\vec{V}_n^k \\ & + \xi^2 \sum_{k=1}^{4} h_k(r,s)\,{}^0a_k \left({}^tQ_n^k\,{}^t\vec{V}_n^k + {}^tQ_1^k\,{}^t\vec{V}_1^k + {}^tQ_2^k\,{}^t\vec{V}_2^k\right) \\ & + \xi^3 \sum_{k=1}^{4} h_k(r,s)\,{}^0a_k \left({}^tC_1^k\,{}^t\vec{V}_1^k + {}^tC_2^k\,{}^t\vec{V}_2^k\right) \end{aligned} \tag{1.13}$$

where $h_k(r,s)$ is the interpolation function corresponding to node k. The incremental displacement field has the same form as in Eq. (1.10)

$$\vec{u}(r,s,\xi) = \sum_{k=1}^{4} h_k(r,s)\vec{u}_L^k + \sum_{k=1}^{4} h_k(r,s)\vec{u}_Q^k \tag{1.14}$$

1.2.2 Mixed interpolation of strain field

The total Lagrangian formulation is used for large deformation but small strain analysis. In this framework, the covariant components of the Green-Lagrange strain with respect to the initial configuration are defined by

$$ {}^t_0\varepsilon_{ij} = \frac{1}{2}\left({}^t\vec{g}_i \cdot {}^t\vec{g}_j - {}^0\vec{g}_i \cdot {}^0\vec{g}_j\right) \tag{1.15} $$

where

$$ {}^0\vec{g}_i = \frac{\partial\, {}^0\vec{x}}{\partial r_i}, \quad {}^t\vec{g}_i = \frac{\partial\, {}^t\vec{x}}{\partial r_i} \quad \textit{with} \quad r_1 = r,\ r_2 = s,\ r_3 = \xi \tag{1.16} $$

The incremental strains are directly calculated by

$$ {}_0\varepsilon_{ij} = {}^{t+\Delta t}_{0}\varepsilon_{ij} - {}^t_0\varepsilon_{ij} = \frac{1}{2}\left(\frac{\partial\vec{u}}{\partial r_i}\cdot {}^t\vec{g}_j + \frac{\partial\vec{u}}{\partial r_j}\cdot {}^t\vec{g}_i + \frac{\partial\vec{u}}{\partial r_i}\cdot\frac{\partial\vec{u}}{\partial r_j}\right) \tag{1.17} $$

In order to avoid shear locking, the Dvorkin-Bathe transverse shear strain field is assumed, by interpolating the covariant components of the transverse shear strains using for all ξ

$$ {}^t_0\tilde{\varepsilon}_{r\xi} = \frac{1}{2}(1+s)\,{}^t_0\varepsilon_{r\xi}\Big|_{\substack{r=0\\ s=1}} + \frac{1}{2}(1-s)\,{}^t_0\varepsilon_{r\xi}\Big|_{\substack{r=0\\ s=-1}} \tag{1.18a} $$

$$ {}^t_0\tilde{\varepsilon}_{s\xi} = \frac{1}{2}(1+r)\,{}^t_0\varepsilon_{s\xi}\Big|_{\substack{r=1\\ s=0}} + \frac{1}{2}(1-r)\,{}^t_0\varepsilon_{s\xi}\Big|_{\substack{r=-1\\ s=0}} \tag{1.18b} $$

While the basic MITC4 element does not show membrane locking, the in-plane membrane behavior can of course be improved by introducing incompatible displacement modes [6], as offered for example in ADINA [27]. A similar improvement in the membrane behavior must be expected when using incompatible displacement modes in the formulation of the enriched element presented here.

However, the strain assumptions normal to the shell mid-surface used here, mean that the element will show pinching locking. This behavior can be alleviated using the MITC approach applied to the normal strain [15, 28, 29]. To fulfill the condition that the normal strain be zero throughout the element when this strain is zero at the element nodes, we simply interpolate the normal strain bi-linearly over the element using the nodal values directly calculated from the displacement assumptions. These nodal values will be zero for a constant bending situation even when the nodal director vectors are not normal to the shell mid-surface described by ${}^t\vec{x}_M$. Therefore, the assumed transverse normal strain is described by

$$ {}^t_0\tilde{\varepsilon}_{\xi\xi}(r,s,\xi) = {}^t_0\tilde{\varepsilon}_{\xi\xi}\Big|_{Const.} + \left({}^t_0\tilde{\varepsilon}_{\xi\xi}\Big|_{r,s,\xi} - {}^t_0\tilde{\varepsilon}_{\xi\xi}\Big|_{r,s,\xi=0} \right) \tag{1.19} $$

where

$$ \begin{aligned} {}^t_0\tilde{\varepsilon}_{\xi\xi}\Big|_{Const.} &= \frac{1}{4}(1+r)(1+s){}^t_0\varepsilon_{\xi\xi}\Big|_{\substack{r=1\\ s=1\\ \xi=0}} + \frac{1}{4}(1-r)(1+s){}^t_0\varepsilon_{\xi\xi}\Big|_{\substack{r=-1\\ s=1\\ \xi=0}} \\ &+ \frac{1}{4}(1-r)(1-s){}^t_0\varepsilon_{\xi\xi}\Big|_{\substack{r=-1\\ s=-1\\ \xi=0}} + \frac{1}{4}(1+r)(1-s){}^t_0\varepsilon_{\xi\xi}\Big|_{\substack{r=1\\ s=-1\\ \xi=0}} \end{aligned} \tag{1.20} $$

The behavior of this interpolation is thoroughly analyzed in Ref. [29]. All the other strain components are directly obtained using Eq. (1.15).

1.2.3 Displacement/Pressure (u/p) formulation

Unlike shell elements based on the plane stress assumption, shell elements using the full three-dimensional constitutive law suffer also from volumetric locking in incompressible, (or almost incompressible) analysis, just like the elements used in the analysis of solids [6]. The mixed formulation known as the displacement/pressure (u/p) formulation has been proven to be effective for the analysis of incompressible conditions [6,30]. Therefore, we adopt this formulation for the three-dimensional shell element. The key step of using the u/p formulation is to determine the interpolation of the assumed independent pressure field. In the 4/1 plane strain element, the pressure field is assumed to be constant which means that strictly the element does not pass the inf-sup condition [6, 31]. This is observed when regular meshes and special boundary conditions are used [6]. However, in practice, hardly flat and non-distorted shell elements are employed, and therefore the following pressure variation is proposed for the element

$$ p = p_0 + p_1\xi \tag{1.21} $$

Note that the pressure is assumed to be constant on each plane given by a fixed value of ξ and vary linearly through the shell thickness. The linear pressure distribution is introduced considering bending. The cost increase by using this formulation is negligible since only two additional pressure degrees of freedom are added to each element and these can be statically condensed out prior to the assemblage of the element stiffness matrix. Since the 4/1 flat plane strain element (4-nodes for displacements and a constant pressure) does not satisfy the inf-sup condition for incompressible analysis, there are very special element configurations and boundary conditions in which the shell element will also show checkerboard pressures. However, as mentioned already above, these will hardly be encountered in practice, and, also, can be identified in the post-processing of the results by plotting the pressure bands [6, 32]. A 4-node plane strain element that satisfies the inf-sup condition is presented in Refs. [33, 34]. The interpolation used in these references could be employed for the shell element but would render the shell element in computations considerably more expensive.

1.3 Numerical studies

In this section, we illustrate some important features of our shell element through the results of several test problems. We use our shell element with 5, 7, 9, or 11 degrees of freedom per node, see Table 1.2, which also lists the orders of numerical integration used. The element with 5 degrees of freedom at each node is the MITC4 shell element. Here, we use "t" for the original shell thickness instead of ${}^0a$ used above.

1.3.1 Cantilever beam under in-plane tangential tractions on the top and bottom surfaces

We consider a cantilever beam of rectangular cross-section with tangential in-plane tractions applied on its top and bottom surfaces. Of course, for normal tractions, the exact solution through the thickness is obtained (see also section 1.3.2). In this

Table 1.2: Summary of shell models

Shell Model	Nodal DOFs	Constitutive Law	Gauss Integration Points ($r \times s \times \xi$)
5 DOF	u, v, w, α, β	Modified	$2 \times 2 \times 2$
7 DOF	$u, v, w, \alpha, \beta,$ Δ_a, q_n	Full 3D	$2 \times 2 \times 2$
9 DOF	$u, v, w, \alpha, \beta,$ Δ_a, q_n, q_1, q_2	Full 3D	$2 \times 2 \times 3$
11 DOF	$u, v, w, \alpha, \beta,$ $\Delta_a, q_n, q_1, q_2, c_1, c_2$	Full 3D	$2 \times 2 \times 4$

problem, the in-plane quadratic and cubic displacement functions corresponding to q_1, q_2, c_1 and c_2 play an important role in the prediction of the stress field. Three load cases are tested as shown in Table 1.3, using $L = 20.0$, $t = 1.0$, $q = 10.0$, $E = 1.0 \times 10^5$ and $\nu = 0.3$. The beam is meshed with 41 elements along its length. We report the stresses as evaluated along the vertical centerline of the element located at the center of the beam, where edge effects are negligible. The analytical values for the stresses are derived in the Appendix.

In the first load case, the resultant axial force and shear force are zero but the bending moment is nonzero. As shown in Fig. 1-3, all shell element solutions give the same correct axial stress distribution. However, only the 11-DOF shell element predicts the correct shear stress distribution satisfying the zero resultant shear force condition and the traction boundary conditions on the top and bottom surfaces, $\tau_{xz}|_{\xi=\pm 1} = q$. In the second load case, the resultant shear force and bending moment are zero, but the axial force is nonzero. Fig. 1-4 shows the calculated stress distributions. In this case, both, the 9-DOF shell element and the 11-DOF shell element give the analytical solutions because the cubic displacement function has no effect on the finite element solution. In the third load case, the resultant axial force and bending moment are nonzero, but the resultant shear force is zero. Fig. 1-5 gives the calculated results. The predicted transverse shear stress is quite different using

Table 1.3: Cases of applied tractions and analytic stress distributions for the in-plane traction test

	Case 1	Case 2	Case 3
Tangential forces on top and bottom surfaces	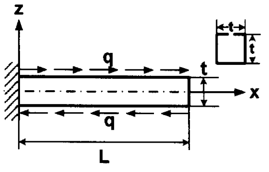	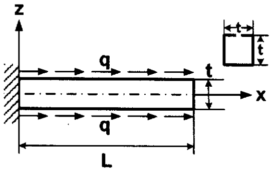	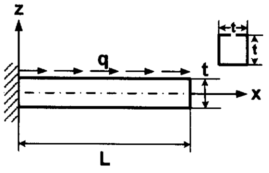
Equivalent force and moment on mid-surface	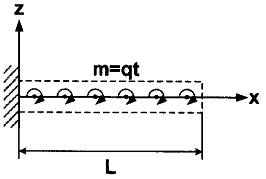	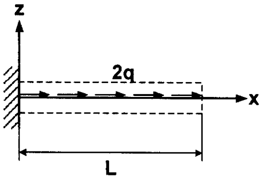	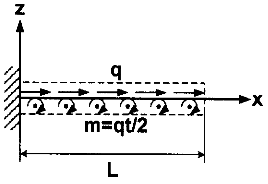
Analytical distribution of τ_{xx} through the thickness at $x = L/2$	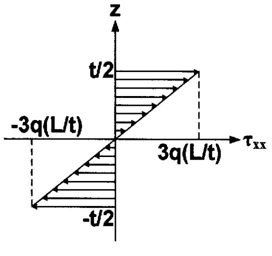	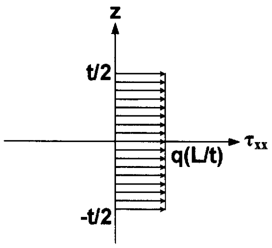	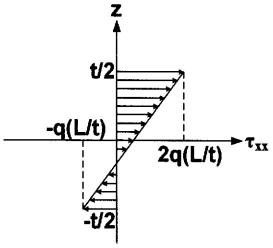
Analytical distribution of τ_{xz} through the thickness	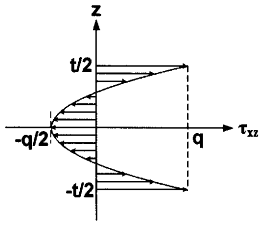	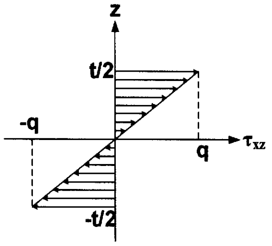	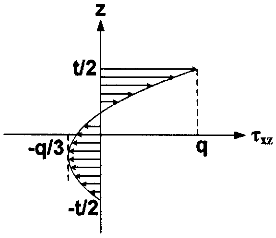

§ For simulations, stresses are evaluated at the center of the beam ($x = L/2$) by using 41 elements along the beam with $L = 20.0$, $t = 1.0$, $q = 10.0$, $E = 1.0 \times 10^5$, $\nu = 0.3$

the various element assumptions. Only the 11-DOF shell element gives an accurate solution satisfying the traction boundary conditions on the top and bottom surfaces, $\tau_{xz}|_{\xi=1} = q$ and $\tau_{xz}|_{\xi=-1} = 0$. This result must be expected, since the case is a linear superposition of cases 1 and 2.

Here, in general, the 11-DOF shell element with the quadratic distribution of the transverse shear stress through its thickness must be used to accurately capture the effect of tangential tractions on the top and bottom shell surfaces (satisfying the traction boundary conditions).

1.3.2 Pressurized cylinder

We consider the pressurized cylinder problem shown in Fig. 1-6. We use this problem to test the predictive capabilities of our shell element in the analysis of a thick-walled structure. A one element model is used, see Fig. 1-6(b). Note that, since the cylinder can only expand or contract in the radial direction due to symmetry, the degrees of freedom for the in-plane quadratic and cubic displacement functions (q_1, q_2, c_1 and c_2) have no effect in the solution of this problem, i.e. the 9-DOF and 11-DOF shell elements will give the same result as the 7-DOF element.

The analytical solutions of this plane strain problem ($\varepsilon_{zz} = 0$) for the radial displacement u_r, and the radial and circumferential stress τ_{rr} and $\tau_{\theta\theta}$ are

$$u_r = \frac{P_i R_i^2 - P_o R_o^2}{2(\lambda + G)(R_o^2 - R_i^2)} \times r + \frac{R_i^2 R_o^2 (P_i - P_o)}{2G(R_o^2 - R_i^2)} \times \frac{1}{r} \tag{1.22a}$$

$$\tau_{rr} = \frac{P_i R_i^2 - P_o R_o^2}{R_o^2 - R_i^2} - \frac{R_i^2 R_o^2 (P_i - P_o)}{R_o^2 - R_i^2} \times \frac{1}{r^2} \tag{1.22b}$$

$$\tau_{\theta\theta} = \frac{P_i R_i^2 - P_o R_o^2}{R_o^2 - R_i^2} + \frac{R_i^2 R_o^2 (P_i - P_o)}{R_o^2 - R_i^2} \times \frac{1}{r^2} \tag{1.22c}$$

where R_o and R_i are the outer and inner radii, respectively, P_o and P_i are the applied pressures, λ and G are the Lamé constants, and $R_i \leq r \leq R_o$.

Table 1.4 lists the predicted radial displacement of the cylinder mid-surface, and shows that the displacement obtained using the 7-DOF shell element is in good agreement with the analytical solution, even when the cylinder is rather thick. However,

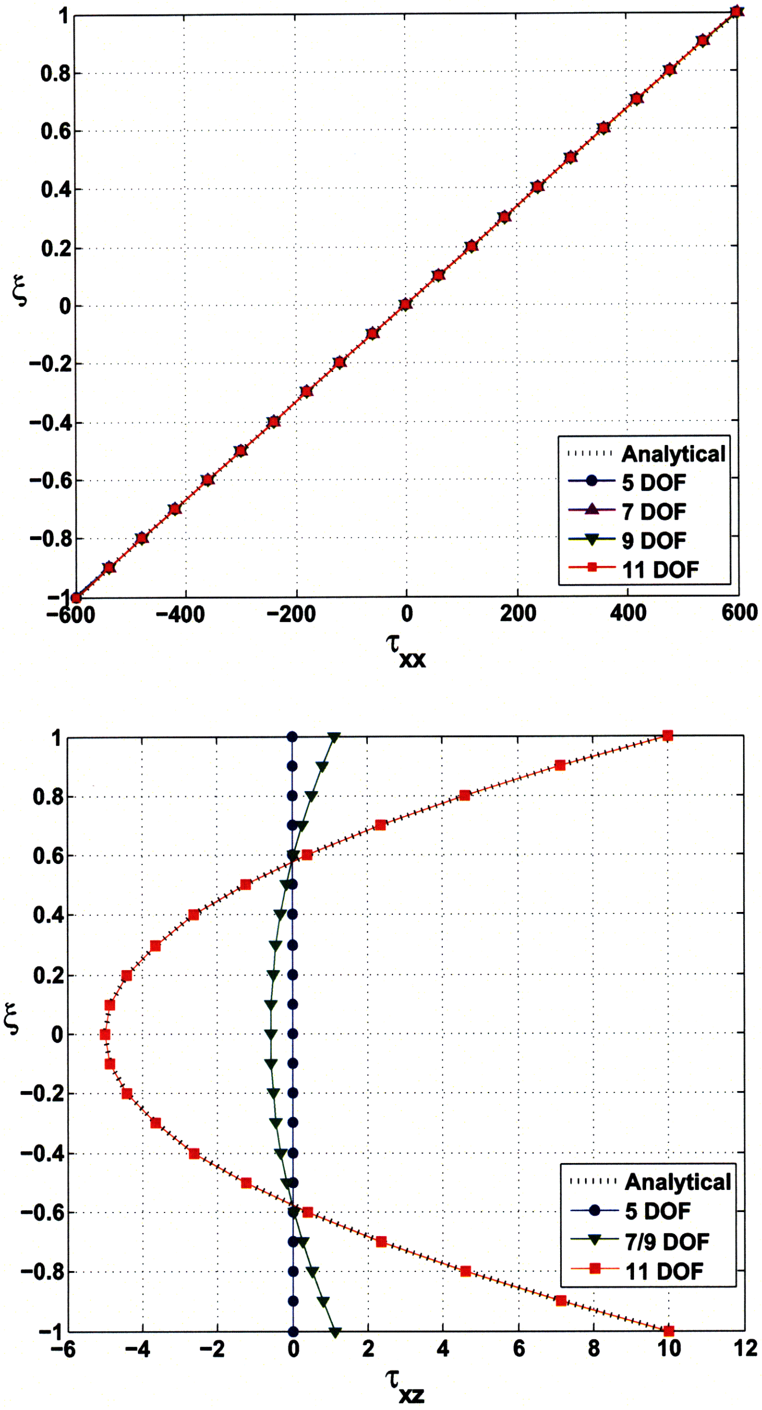

Figure 1-3: Stress distributions in a cantilever beam under in-plane tractions (Case 1)

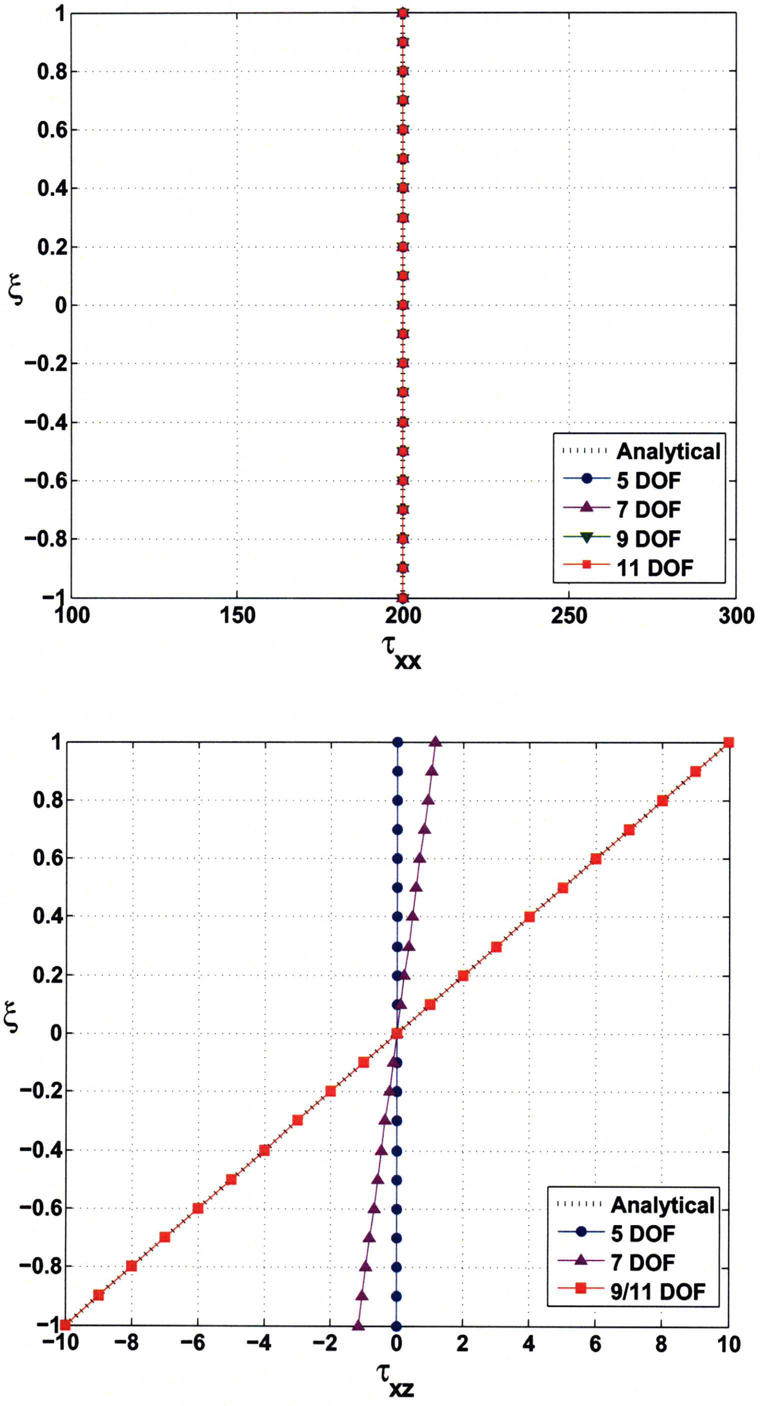

Figure 1-4: Stress distributions in a cantilever beam under in-plane tractions (Case 2)

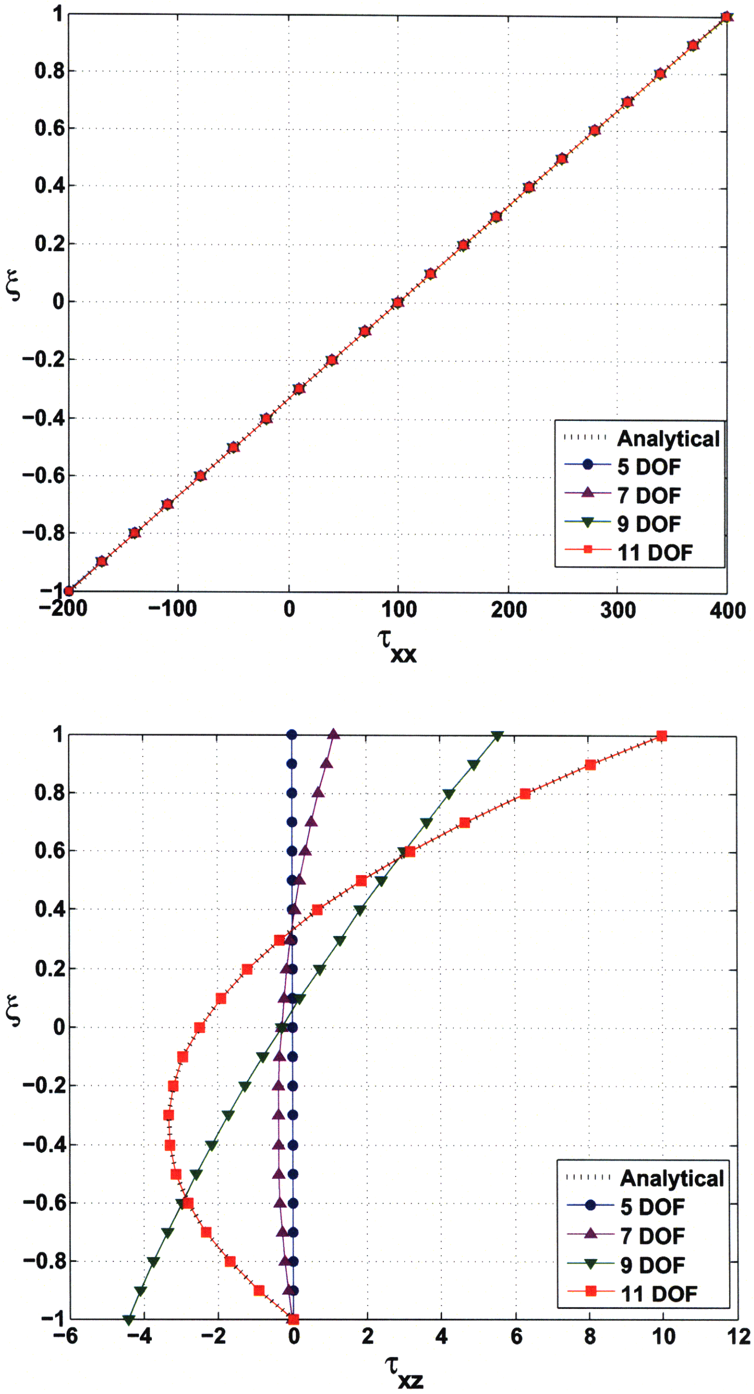

Figure 1-5: Stress distributions in a cantilever beam under in-plane tractions (Case 3)

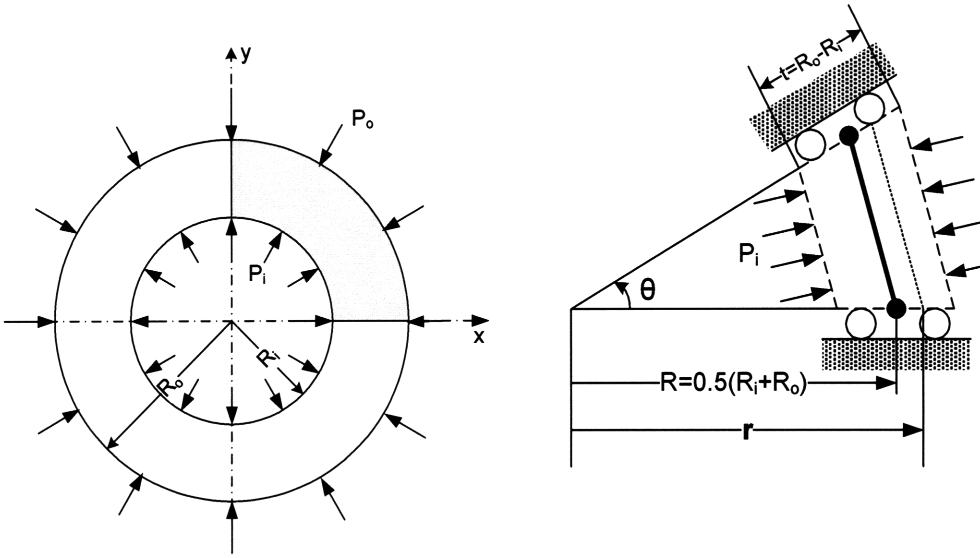

(a) (b)

Figure 1-6: Pressurized cylinder in plane strain condition; $\theta = 2\,^\circ, P_i = 20t, P_o = 80t, R = 10.0, E = 1.0\times10^4$; (a) the whole model, (b) single element representation (only radial displacement is allowed)

in the (almost) incompressible case, the 7-DOF shell element needs to be used with the proposed assumed pressure field. Of course, if the cylinder is thin, both, the 5-DOF and 7-DOF shell elements give virtually the same result for the mid-surface displacement. Figs. 1-7 and 1-8 show the predicted radial and hoop stresses for the thin and thick cases.

Table 1.4: Normalized radial displacement of the pressurized cylinder at $r = R$

	Shell model		$t = 0.1$	$t = 1.0$	$t = 2.0$	$t = 5.0$
ν=0.3	5 DOF		0.9962	0.9643	0.9294	0.8234
	7/9/11 DOF		0.9998	0.9998	0.9998	0.9980
ν=0.499999	5 DOF		0.9915	0.9203	0.8472	0.6495
	7/9/11 DOF		0.9998	0.6150	0.0905	0.0025
	7/9/11 DOF	(u/p)	0.9998	0.9998	0.9998	0.9987

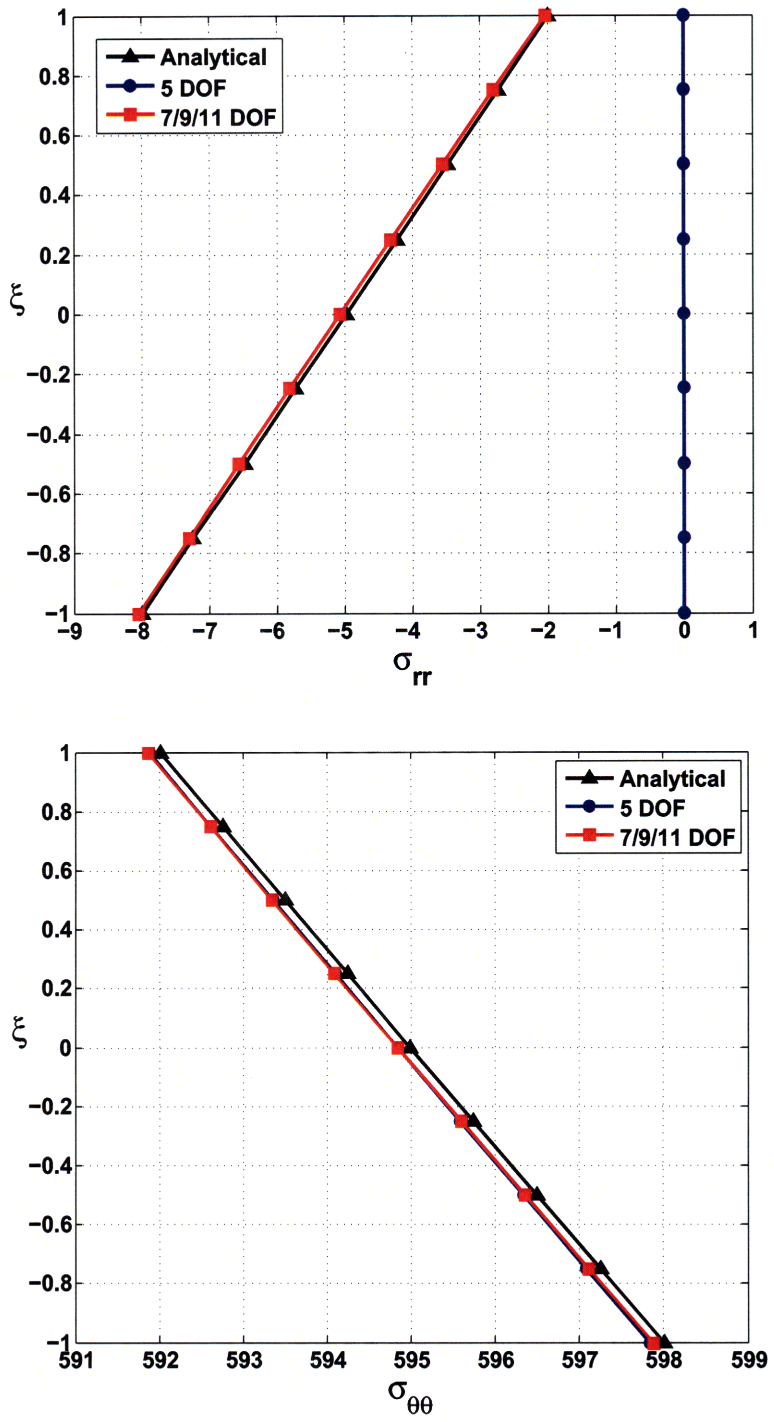

Figure 1-7: Stress distributions in the pressurized cylinder ($t = 0.1, P_i = 2.0, P_o = 8.0$)

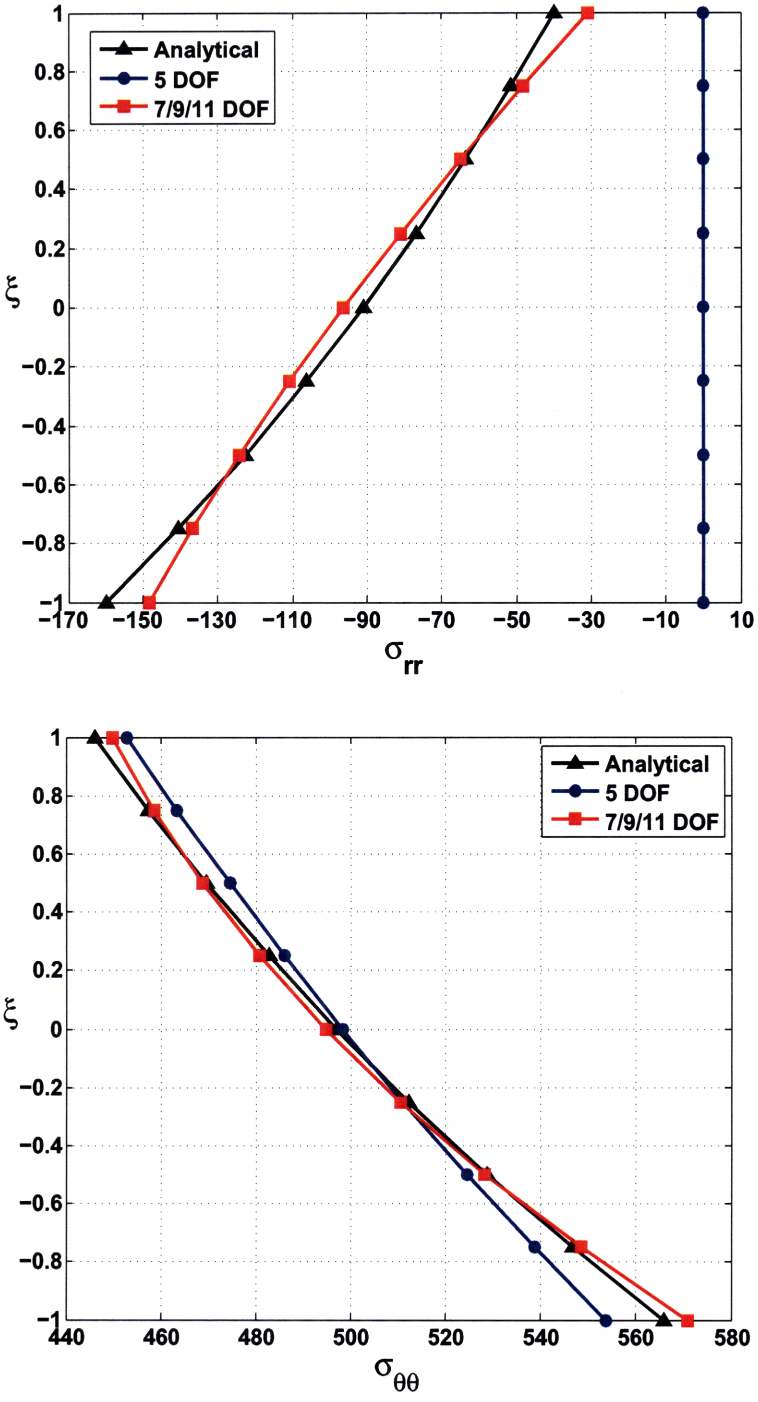

Figure 1-8: Stress distributions in the pressurized cylinder ($t = 2.0, P_i = 40, P_o = 160$)

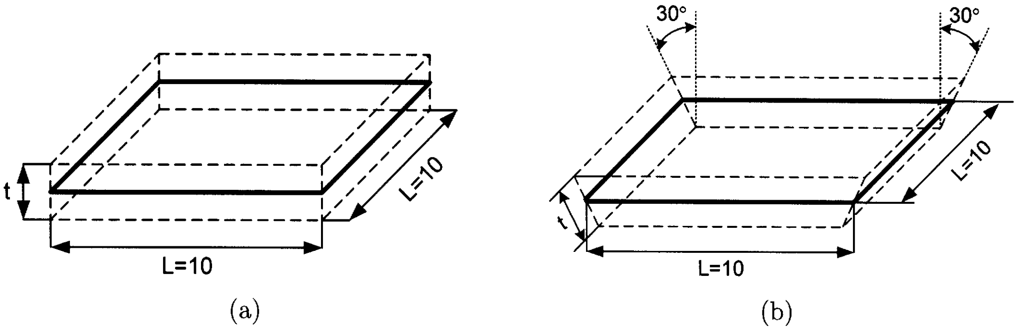

(a) (b)

Figure 1-9: Single element test for ill-conditioning; (a) director vectors are normal to the mid-surface, (b) director vectors are rotated 30° from the normal direction

1.3.3 Test cases for conditioning of the stiffness matrix

In these problem solutions, we study the conditioning of the stiffness matrices when the thickness of the shell decreases and the material becomes incompressible. The degree of ill-conditioning can be measured by the condition number defined as [6],

$$cond(K) = \frac{\lambda_{max}}{\lambda_{min}} \tag{1.23}$$

where λ_{max} and λ_{min} are the maximum and minimum eigenvalues of the stiffness matrix K with rigid body modes excluded. For comparison purposes, we use C_K

$$C_K = \log_{10}\{cond(K)\} \tag{1.24}$$

First, a single element with two different orientations of director vectors as shown in Fig. 1-9 is tested. The results are listed in Table 1.5. We see that the condition number of the 3D-shell element with more than five degrees of freedom is for the thin case only about an order of magnitude larger than for the MITC4 shell element with five degrees of freedom. This increase in the condition number is small when compared to the increase for the 3D-solid element. Note that $cond(K) \sim O(t^{-2})$ for all shell elements while $cond(K) \sim O(t^{-4})$ for the 3D-solid element with the thickness, t. When the director vectors are not normal to the shell mid-surface as shown in Fig. 1-9(b), the condition number only slightly increases. This is shown in Fig. 1-10.

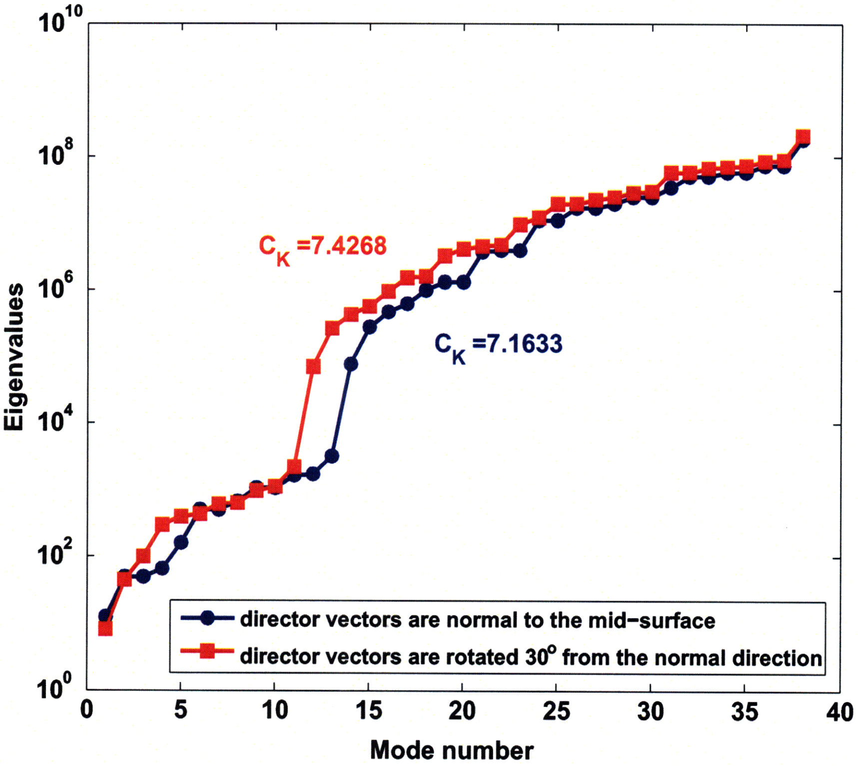

Figure 1-10: Eigenvalues of single element (11-DOF, $E = 1.0 \times 10^7, \nu = 0.3, t = 0.1$)

Table 1.5: C_K with different element thicknesses, see Fig. 1-9 ($E = 1.0 \times 10^7, \nu = 0.3$)

Shell model	Director vectors	$t = 1.0$	$t = 0.1$	$t = 0.01$	$t = 0.001$
5 DOF	(a)	3.8315	5.8217	7.8216	9.8216
	(b)	4.0434	6.0365	8.0364	10.0364
7 DOF	(a)	5.1716	7.1632	9.1632	11.1632
	(b)	5.3384	7.3318	9.3318	11.3318
9 DOF	(a)	5.1716	7.1632	9.1632	11.1632
	(b)	5.4338	7.4268	9.4267	11.4267
11 DOF	(a)	5.1732	7.1633	9.1632	11.1632
	(b)	5.4349	7.4268	9.4267	11.4267
3D 8-node solid element	(a)	3.8963	7.8753	11.8750	15.5166

(a) director vectors are normal to the mid-surface (b) director vectors are rotated 30 ° from the normal direction

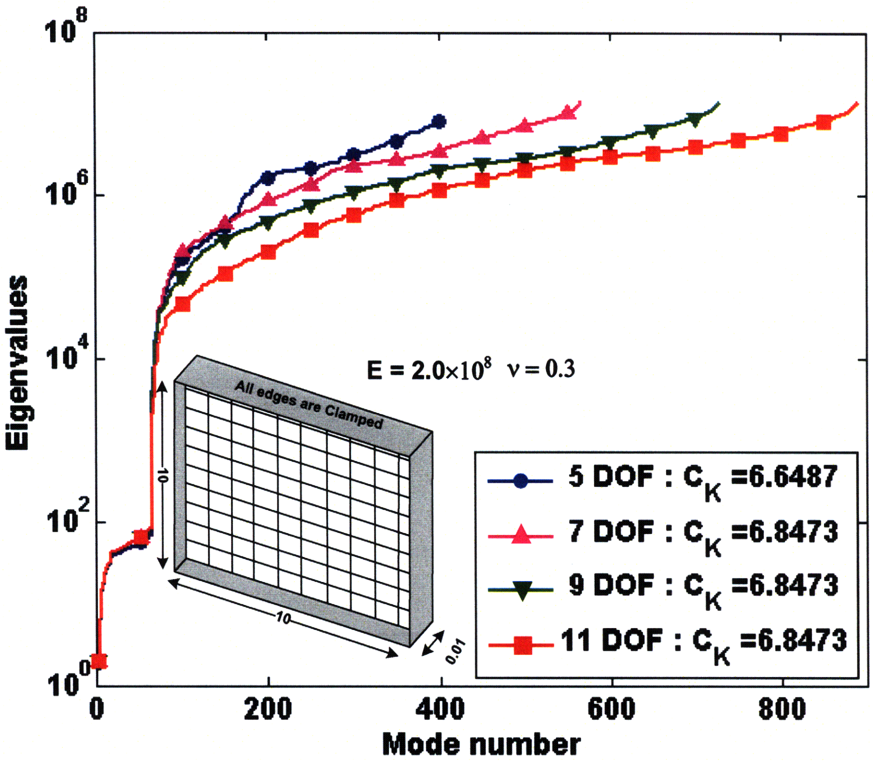

Figure 1-11: Eigenvalues and condition numbers (director vectors are normal to the mid-surface)

Next, we consider a plate modeled with a 10×10 element mesh, see Fig. 1-11, and solve for the eigenvalues and condition numbers, see Ref. [20] for a similar example. We see that the condition numbers of our shell element with 7 to 11 degrees of freedom are only slightly larger than for the MITC4 element. Therefore, in the analysis of shell structures in which 3D effects shall be predicted, the element proposed here is much more reliable than the 3D-solid element.

Finally, the single element with an almost incompressible material is considered. In this case, we have inevitably an ill-conditioned stiffness matrix because, for 3D type elements, we have at least one very large eigenvalue corresponding to the volumetric deformation mode. In Fig. 1-12, the displacement-based (without pressure degrees of freedom) shell element shows eight very large eigenvalues that cause the element to be too stiff and lock, see Tables 1.4, 1.7, and 1.9. If we use the element with the u/p formulation, see the assumed pressure field in Eq. (1.21), only two very

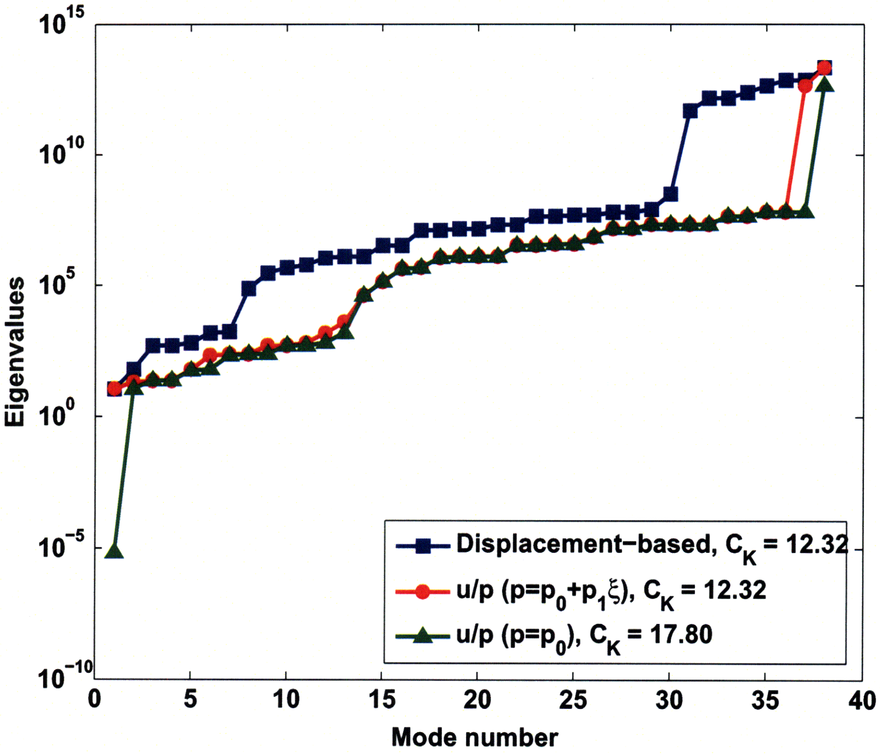

Figure 1-12: Eigenvalues of single element in almost incompressible case (11-DOF, $E = 1.0 \times 10^7, \nu = 0.499999, t = 0.1$); director vectors are normal to the mid-surface

large eigenvalues which correspond to the volumetric expansion mode (the constant pressure mode) and a bending mode (the linear pressure mode through the thickness) are observed. It appears natural to therefore try to use only the constant pressure field ($p = p_0$) in the u/p formulation, but then the element has a spurious zero energy mode corresponding to the bending mode. Hence, the pressure assumption in Eq. (1.21) is more appropriate.

1.3.4 Hyperboloid shell problems

These shell problems were proposed and studied by Chapelle and Bathe [2, 35, 36] and provide excellent test problems for shell elements. We solve the problems here to investigate the performance of our shell discretizations in the almost incompressible case.

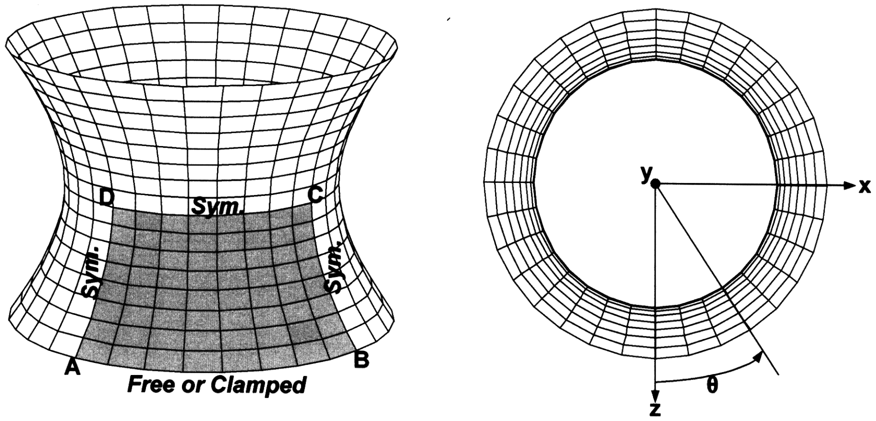

Figure 1-13: The hyperboloid shell problem ($E = 2.0 \times 10^{11}, t = 0.01, p_0 = 1.0 \times 10^6$)

The geometry of the shell mid-surface is given by (see Fig. 1-13)

$$x^2 + z^2 = 1 + y^2, \quad y \in [-1, 1] \tag{1.25}$$

The hyperboloid mid-surface is subjected to the smoothly varying periodic pressure

$$p(\theta) = p_0 \cos(2\theta) \tag{1.26}$$

If the shell is clamped on both ends, the problem is a membrane-dominated problem, and if the shell is free on both ends, the problem is a bending-dominated problem. We use a 16 × 16 uniform mesh of elements to solve the two problems.

Some results are listed in Tables 1.6, 1.7, 1.8 and 1.9. When the material is compressible (see Tables 1.6 and 1.8), each shell model gives similar results in both the membrane and bending dominated cases. However, when the material is nearly incompressible (see Tables 1.7 and 1.9), the shell elements based on the full three-dimensional constitutive law experience volumetric locking while the 5-DOF MITC4 shell element of course does not lock. Note that, by using the u/p formulation, the volumetric locking of the shell elements using the three dimensional constitutive law is successfully removed in, both, the membrane and bending dominated cases.

Table 1.6: The clamped-clamped hyperboloid shell ($\nu = 0.333333$)

Shell model	Strain energy	Max. magnitude of V-displacement	Max. magnitude of U/W-displacement
5 DOF	5.33891E+02	6.99667E-04	1.35918E-03
7 DOF	5.27460E+02	7.01485E-04	1.35438E-03
9 DOF	5.28865E+02	7.02342E-04	1.35637E-03
11 DOF	5.28915E+02	7.02341E-04	1.35635E-03

Table 1.7: The clamped-clamped hyperboloid shell ($\nu = 0.499999$)

Shell model		Strain energy	Max. magnitude of V-displacement	Max. magnitude of U/W-displacement
5 DOF		5.70978E+02	7.56065E-04	1.46331E-03
7 DOF		0.40085E+02	0.34764E-04	0.18041E-03
9 DOF		0.74792E+02	0.57580E-04	0.34114E-03
11 DOF		1.18613E+02	1.38555E-04	0.36024E-03
7 DOF	(u/p)	5.55900E+02	7.59076E-04	1.45204E-03
9 DOF	(u/p)	5.58361E+02	7.60885E-04	1.45701E-03
11 DOF	(u/p)	5.58467E+02	7.60881E-04	1.45706E-03

Table 1.8: The free-free hyperboloid shell ($\nu = 0.333333$)

Shell model	Strain energy	Max. magnitude of V-displacement	Max. magnitude of U/W-displacement
5 DOF	4.53983E+05	1.04082E+00	2.10145E+00
7 DOF	4.53820E+05	1.04044E+00	2.10070E+00
9 DOF	4.55217E+05	1.04372E+00	2.10719E+00
11 DOF	4.55237E+05	1.04377E+00	2.10728E+00

Table 1.9: The free-free hyperboloid shell ($\nu = 0.499999$)

Shell model		Strain energy	Max. magnitude of V-displacement	Max. magnitude of U/W-displacement
5 DOF		3.81804E+05	0.87391E+00	1.76575E+00
7 DOF		0.02886E+05	0.00198E+00	0.00846E+00
9 DOF		1.45692E+05	0.33107E+00	0.66385E+00
11 DOF		1.79671E+05	0.40899E+00	0.82209E+00
7 DOF	(u/p)	3.81421E+05	0.87293E+00	1.76395E+00
9 DOF	(u/p)	3.82368E+05	0.87517E+00	1.76836E+00
11 DOF	(u/p)	3.82384E+05	0.87520E+00	1.76843E+00

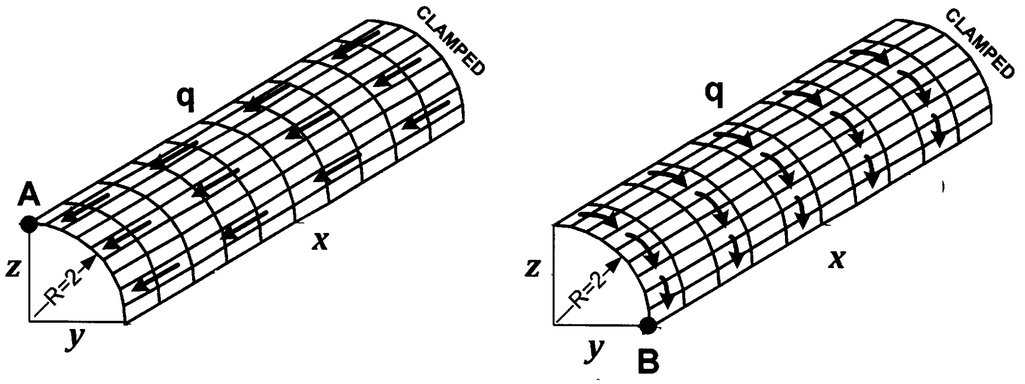

(a) (b)

Figure 1-14: The quadrant of a cantilevered cylinder under in-plane tractions ($E = 1.0 \times 10^4, \nu = 0.3$, length=40, thickness=0.1); (a) case of applied longitudinal traction ($q = 0.1$), (b) case of applied circumferential traction ($q = 0.007$)

1.3.5 A quadrant of a cantilevered cylinder under in-plane tangential tractions

A quadrant of a cantilevered cylinder under in-plane tangential tractions is tested. The tractions are applied in the longitudinal direction for one case and the circumferential direction for the other case as depicted in Fig. 1-14. In order to see how the load positions affect the solutions, the deformation-dependent tractions are applied on the top, middle and bottom surfaces for each case. Geometrically nonlinear analyses are performed using the 11-DOF shell element with a 10×9 mesh of elements in the total Lagrangian framework [6]. The deformed shapes and the displacements and effective stresses are given in Figs. 1-15-1-20. We can see that significant response differences arise depending on how the tractions are applied.

Note that we may obtain very similar results with the 5-DOF MITC4 shell element by applying the resultant forces and moments on the shell mid-surface, especially for a very thin structure as in this problem. Here the effect of the quadratic and cubic in-plane displacements is small enough to be neglected. However, our 11-DOF shell element provides a direct and natural way to include the effects of surface tractions when these are initially unknown (e.g. imposed in a metal forming problem), vary over the shell top and bottom surfaces and the shell thickness changes significantly.

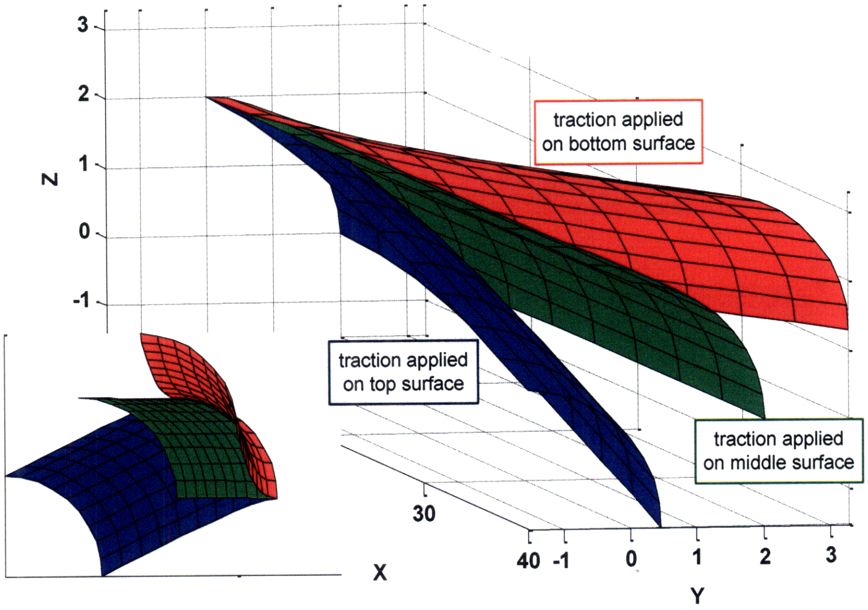

Figure 1-15: The deformed shapes when the traction is applied in the longitudinal direction

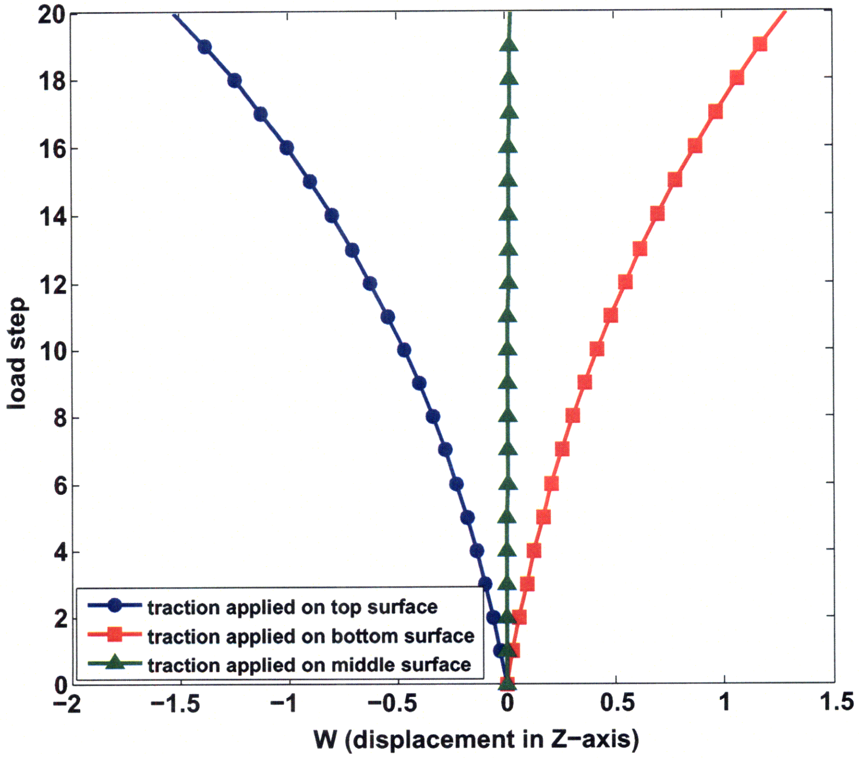

Figure 1-16: Displacement in z-direction of point A in Fig. 1-14(a)

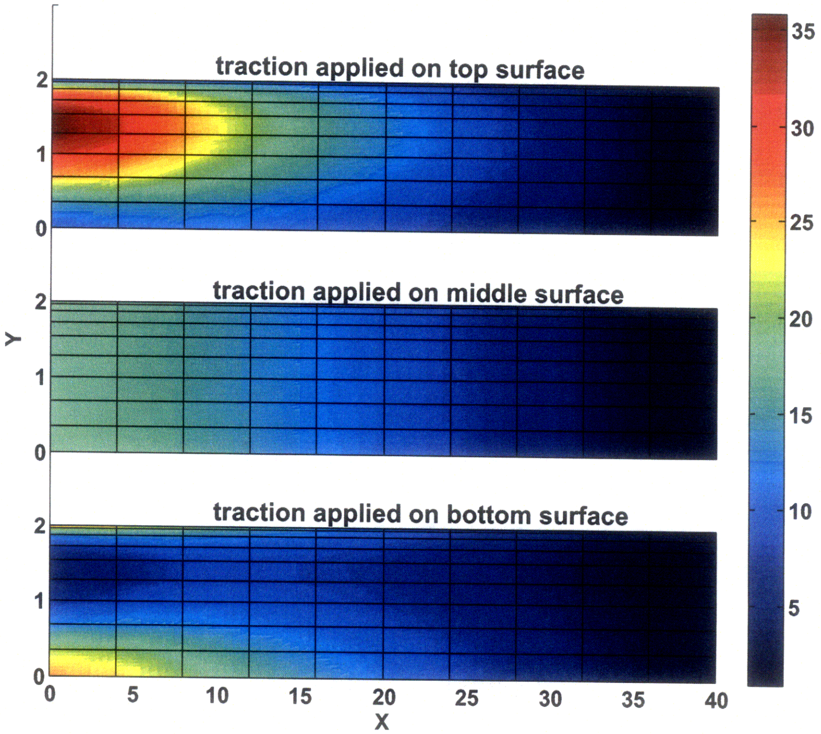

Effective Stress on the top surface (Case a)

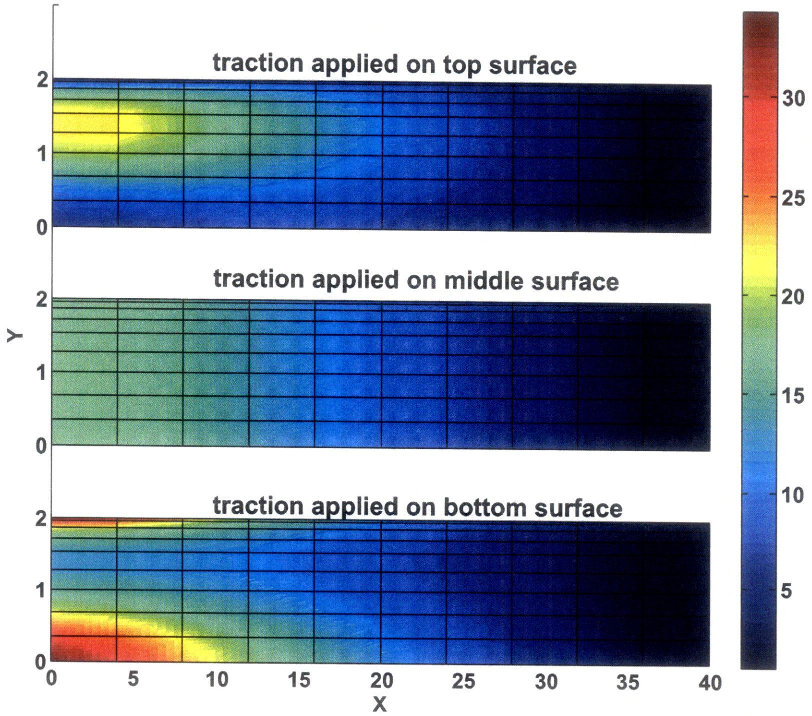

Effective Stress on the bottrom surface (Case a)

Figure 1-17: The effective stresses on the top and bottom surfaces in Case (a) of Fig. 1-14

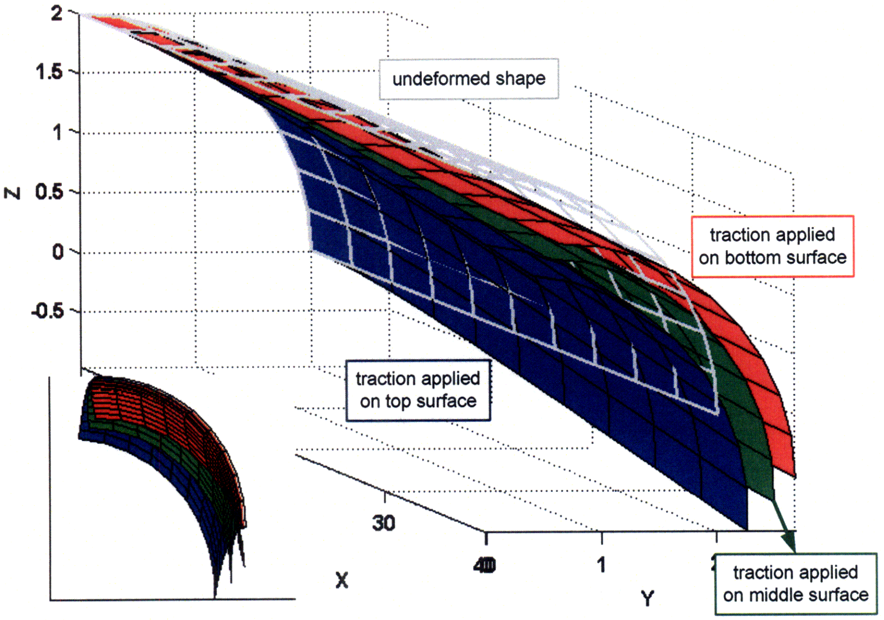

Figure 1-18: The deformed shapes when the traction is applied in the circumferential direction

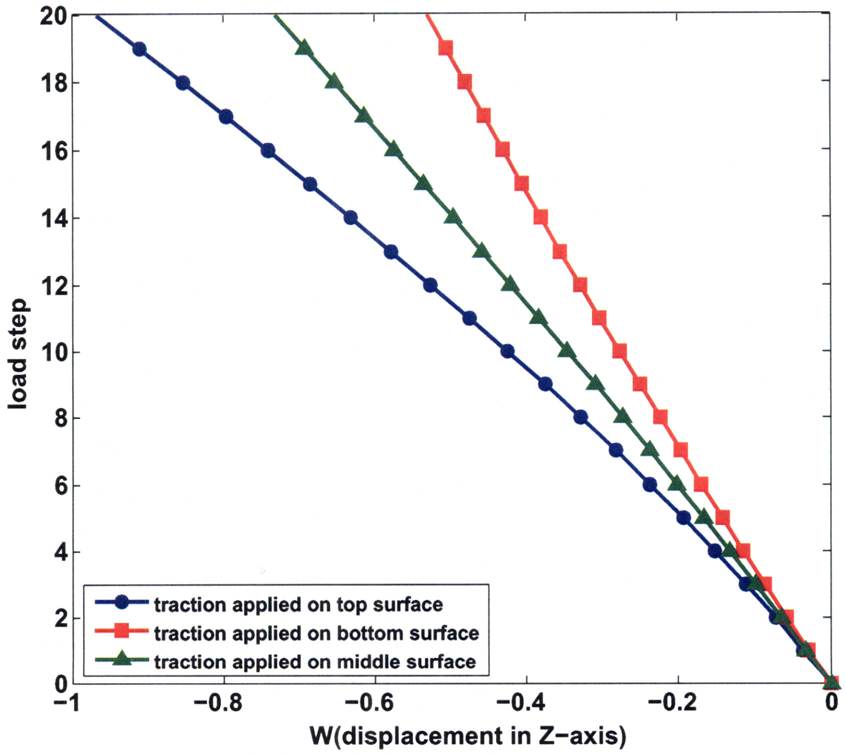

Figure 1-19: Displacement in z-direction of point B in Fig. 1-14(b)

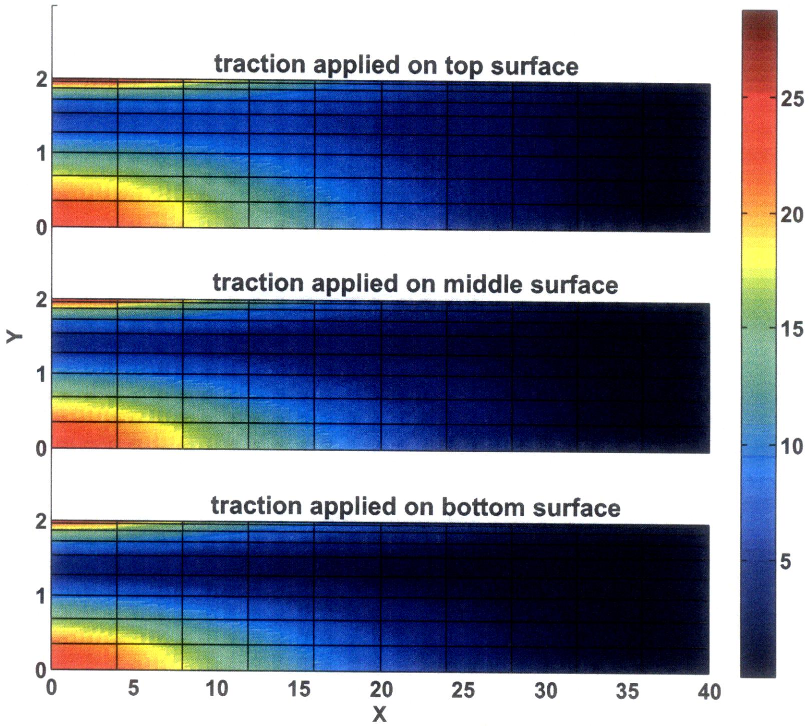

Effective Stress on the top surface (Case b)

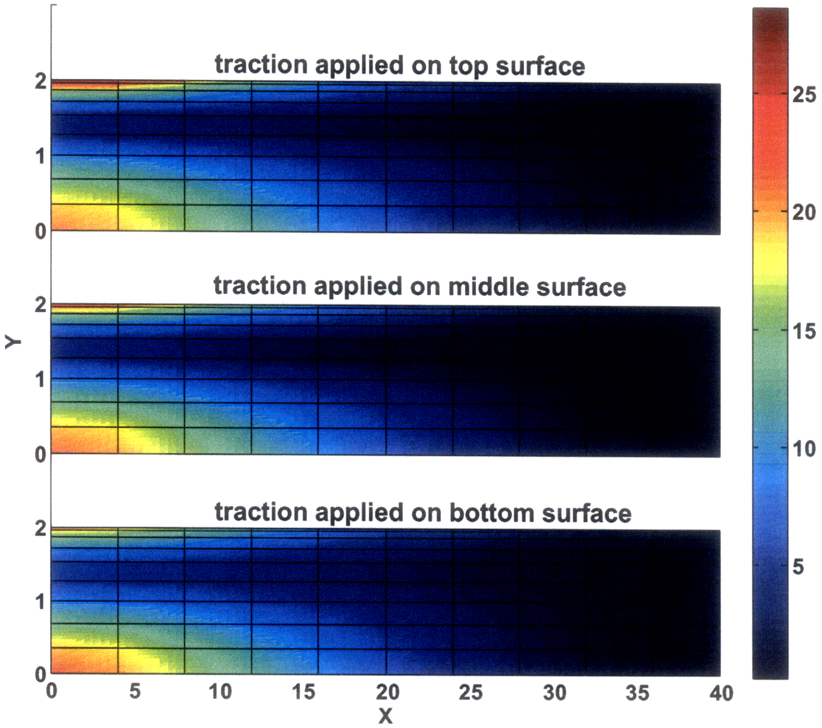

Effective Stress on the bottom surface (Case b)

Figure 1-20: The effective stresses on the top and bottom surfaces in Case (b) of Fig. 1-14

1.4 Concluding remarks

We presented in this chapter a 4-node 3D-shell element that, in essence, represents a hierarchical improvement of the MITC4 shell element to include some important three-dimensional effects: the full 3D stress-strain law is used, the thickness change is included, shell tractions can be applied on the top and bottom surfaces of the shell, and the material can be incompressible. An important attribute is that the element does not result in undue ill-conditioning (as seen when shell surface top and bottom nodes are used in the kinematic description of 3D-shell elements) and does not result in instabilities (as seen with enhanced strain formulations). There are various fields of applications for the 3D-shell element, including all those involving large strain effects and contact. But in particular, the given formulation provides the basic framework for effective large strain analyses using 3D orthotropic hyperelastic or elastic-plastic material descriptions [3, 37–39] as encountered in bio-engineering and metal forming. A quite outstanding research task is the mathematical analysis of the proposed 3D-shell element, as pursued in Refs. [2, 10, 13, 19, 21] for other formulations.

Chapter 2

A triangular 6-node shell element

A large amount of research has been expended over the past four decades on the development of shell finite elements, and yet more effective triangular shell elements are still much needed, see Refs. [1, 2, 40] and the references therein. In particular, the search for a general and uniformly effective 6-node triangular shell element continues, and indeed the development of such an element represents one of the remaining key challenges in finite element analysis. While such an element is, in the first instance, sought for linear analysis, of course, the formulation should, as well, be directly extendable to general nonlinear analysis.

Numerous shell analyses are conducted routinely but very fine discretizations and quadrilateral elements are typically used [41]. An effective general curved 6-node shell element would be very useful in that (i) it can be employed to discretize virtually any shell geometry, (ii) it can be used to model shells overlaid on three-dimensional solids that are represented in free-form meshing by 10 or 11-node tetrahedral solid elements, and (iii) it would give accurate solutions when using relatively coarse meshes.

Originally, to a large extent, shell elements were developed by simply superimposing plate bending and in-plane membrane behavior, and flat facet-shell elements were proposed. As now well known, such elements are not truly representing shell behavior and indeed may not even converge depending on which shell problem is solved [2]. The most promising formulation approach for a general shell element is based on the use of the "basic shell model" [2, 13, 14]. This mathematical model is obtained from the 3D continuum by introducing the Reissner-Mindlin kinematical hypothesis and the plane stress assumption for the mid-surface and the material layers parallel to that surface. Ideally, the shell element should then converge reliably and optimally to the exact solution of the mathematical model and for any well-posed shell problem. However, the usual displacement interpolation leads to locking and a scheme needs to be used to alleviate this detrimental behavior.

Successful quadrilateral general shell elements have been developed using the mixed-interpolated-tensorial-component approach, that is, the MITC procedure [7, 8, 11, 12, 42]. The advantage of this approach is that the elements are general, that is, they can be used for general shell geometries in linear and nonlinear analyses, and the elements have only the degrees of freedom of displacement-based elements with negligible additional computational cost. The MITC4 element is now widely used [41] and can also be employed in a hierarchical manner to model additional 3D effects [43]. While tight mathematical convergence proofs of the MITC shell elements are not available, and indeed for general geometries may be out of reach, the elements have been thoroughly tested on appropriate 'discriminating and revealing' test problems [2, 9, 12, 35, 36, 43, 44]. However, these studies largely focused on the use of quadrilateral elements, equally successful general triangular shell elements are more difficult to develop.

On the other hand, the family of MITC plate bending elements contains quadrilateral and triangular elements that are very effective, and for plate bending solutions practically optimal [6, 45, 46]. Thorough mathematical convergence analyses and results of numerical studies have been published, see Refs. [47–50]. However, except for the MITC4 element, the elements contain internal nodes with rotational degrees of freedom only, which renders them not effective for extension to shell analyses and general nonlinear analysis. Still, the fact that excellent MITC triangular plate bending elements exist encourages the search for an effective MITC triangular shell element.

A triangular 6-node shell element based on the MITC approach was recently presented by P. S. Lee and K. J. Bathe [1]*. This element has the desirable properties

---

*When we refer to the MITC6 shell element of Ref. [1], we mean the MITC6a shell element of not containing a spurious zero energy mode or artificial factor, being spatially isotropic, having the same degrees of freedom at every node, passing the plate bending and membrane patch tests, showing excellent convergence behavior in plate bending analyses, and reasonable convergence behavior in the analysis of 'discriminating and revealing' shell test problems. In particular, these shell test problems include the analysis of a hyperboloid shell with, at both ends, either clamped or totally free conditions. We consider these two problems to be excellent benchmark problems to test an element formulation for its capacity to predict membrane-dominated and bending-dominated shell behaviors.

However, additional testing of the element by D. Chapelle et al. [51,52] showed a surprising element peculiarity. Namely, when used to model certain shell geometries and boundary conditions, the solution becomes unstable, although the single element does not contain a spurious zero energy mode. An unphysical oscillatory response is predicted, like observed in some solutions with the 4/1 element of the displacement-pressure formulation for incompressible materials [6]. Chapelle et al. stabilized the formulation by replacing a part of the mixed-interpolated shear strain energy by the unreduced displacement-based shear strain energy. As is typical in such techniques of stabilization, a factor is introduced to allocate the amount of stabilization [2,6,51]. Depending on the shell problem solved, if the factor is too large the element behavior deteriorates significantly and if the factor is too small, the instability shows up. While the magnitude of the stabilizing factor is based on some analysis, ideally, we would have a stable and effective formulation without such factor. This is particularly desirable when the element formulation is to be used in general nonlinear analysis. Hence we continued our search for a more reliable and accurate triangular shell element.

In the search for more effective elements, the fundamental difference between the MITC formulation approach and the 'enhanced assumed strain', or EAS, formulation approach is important [53]. Both techniques start with the displacement formulation and aim to improve its predictive capability. Then, in the MITC formulation, the strain assumptions inherently used in the displacement formulation are improved by

---

formulated and tested in that reference.

not including certain terms of the displacement-based strain space. In this way, many MITC elements can, in principle, be developed even for the same displacement assumptions, and the key is to identify the optimal formulation. Hence, when searching for an effective 6-node MITC triangular shell element, many possibilities arise, some of which were studied in Refs. [51,52].

On the other hand, in the EAS formulations, new strain fields are added to those already inherently used in the displacement formulation, like first proposed by E. L. Wilson et al. with incompatible displacement modes, see Refs. [6,54] and the references therein. The EAS approach is generally implemented using static condensation for the additional strain terms on the element level. This results into some additional cost, and complexity in nonlinear analysis, not present in the MITC formulations. While there exits potential in developing elements based on the EAS method, a difficulty encountered is that stable formulations in linear analysis may become unstable in nonlinear analysis [24,25].

In an additional approach to obtain more effective elements, the 'discontinuous Galerkin (DG) method' can be pursued and shell elements can be formulated within this framework [55,56]. This approach has good potential, but stability parameters are used, and significant additional computational cost is present, even when static condensation can be employed. The performance of such shell elements in nonlinear solutions need also still be studied.

An important point is that any newly formulated element should not only be tested on rather simple shell analysis problems, but also on the discriminating problems proposed in Refs. [2,35] and used, for example, in Refs. [1,2,12,14,36,51,52]. The actual performance of a shell element formulation will only be revealed when solving these or equivalent problems and measuring the solution errors in appropriate norms.

The objective in this chapter is to present a further development of the MITC6 shell element of Ref. [1]. The improved MITC6 shell element represents a simple but effective extension of the original element. The element is not based on a stabilization scheme and does not contain any factor to be set. The same membrane strain and transverse shear strain interpolations as in Ref. [1] are used, but the interpolated covariant strain components are referred to an element constant contravariant basis. Of course, the geometry and the displacement-based strains used in the tying process are calculated using the varying quantities, as defined through the discretization of the 'basic shell mathematical model'. For plate problems, the improved element reduces to the original element and hence the results obtained using the original and the improved elements are identical. Indeed, this is one reason why we use this specific interpolation of strain components.

In the next sections we first briefly review the original MITC6 shell element, then we present the formulation of the improved element, and finally we give the numerical results obtained in the solution of the test problems. These benchmark tests include the discriminating test problems referred to above. While we consider in this chapter only linear analysis, the element formulation can directly be extended to general nonlinear analysis, which is an inherent property of the MITC formulations [2,6,8].

2.1 The formulation of the MITC6 shell element

As for displacement-based shell elements, the geometry of the 6-node shell element is interpolated using

$$\vec{x}(r,s,\xi) = \sum_{k=1}^{6} h_k(r,s)\vec{x}_k + \frac{\xi}{2}\sum_{k=1}^{6} a_k h_k(r,s)\vec{V}_n^k \tag{2.1}$$

where h_k is the 2D shape function of the standard isoparametric procedure corresponding to node k, $\vec{x}_k$ is the position vector at node k in the global Cartesian coordinate system, and a_k and $\vec{V}_n^k$ denote the shell thickness and the director vector at node k, respectively. The displacements of the element are given by

$$\vec{u}(r,s,\xi) = \sum_{k=1}^{6} h_k(r,s)\vec{u}_k + \frac{\xi}{2}\sum_{k=1}^{6} a_k h_k(r,s)\left(-\vec{V}_2^k\alpha_k + \vec{V}_1^k\beta_k\right) \tag{2.2}$$

where $\vec{u}_k$ is the nodal displacement vector in the global Cartesian coordinate system, $\vec{V}_1^k$ and $\vec{V}_2^k$ are unit vectors orthogonal to $\vec{V}_n^k$ and to each other, and α_k and β_k are the rotations of the director vector $\vec{V}_n^k$ about $\vec{V}_1^k$ and $\vec{V}_2^k$, respectively and k denotes the node k. The covariant strain components are calculated using

$$e_{ij} = \frac{1}{2}\left(\vec{g}_i \cdot \vec{u}_{,j} + \vec{g}_j \cdot \vec{u}_{,i}\right) \tag{2.3}$$

where

$$\vec{g}_i = \frac{\partial \vec{x}}{\partial r_i} \quad \text{and} \quad \vec{u}_{,i} = \frac{\partial \vec{u}}{\partial r_i} \quad \text{with} \quad r_1 = r,\ r_2 = s,\ r_3 = \xi \tag{2.4}$$

The basic step in the MITC formulation is to select a set of tying points $k = 1, \ldots, n_{ij}$ on the shell midsurface with coordinates $\left(r_{ij}^k, s_{ij}^k\right)$, and define the assumed covariant strain components $\tilde{e}_{ij}$ as

$$\tilde{e}_{ij}(r,s,\xi) = \sum_{k=1}^{n_{ij}} h_{ij}^k(r,s) e_{ij}\Big|_{\left(r_{ij}^k, s_{ij}^k, \xi\right)} \tag{2.5}$$

where n_{ij} is the number of tying points for the covariant strain component $\tilde{e}_{ij}$ and the h_{ij}^k are the assumed interpolation functions satisfying

$$h_{ij}^k\left(r_{ij}^l, s_{ij}^l\right) = \delta_{kl}, \qquad l = 1, \ldots, n_{ij} \tag{2.6}$$

with δ_{kl} the Kronecker delta. This tying procedure is carried out on the elemental level for each individual element. We next express the displacement-based covariant strain components in terms of the nodal displacements and rotations

$$e_{ij} = \mathbf{B}_{ij}\mathbf{U} \tag{2.7}$$

where $\mathbf{B}$ is the strain-displacement matrix and $\mathbf{U}$ is the nodal displacement/rotation vector. Thus we obtain

$$\tilde{e}_{ij} = \left[\sum_{k=1}^{n_{ij}} h_{ij}^k(r,s)\mathbf{B}_{ij}\Big|_{\left(r_{ij}^k, s_{ij}^k, \xi\right)}\right]\mathbf{U} = \tilde{\mathbf{B}}_{ij}\mathbf{U} \tag{2.8}$$

The strain-displacement matrix in Eq. (2.8) gives the covariant strain components as a function of the element coordinates r, s and ξ. The constitutive tensor is defined with respect to the local Cartesian coordinate system in which the plane stress assumption holds. Hence the assumed covariant strains in Eq. (2.8) are transformed into that coordinate system at each integration point to obtain the stiffness matrix. The local Cartesian coordinates are given by $\left(\vec{E}_r, \vec{E}_s, \vec{E}_\xi\right)$ where [6]

$$\vec{E}_r = \frac{\vec{g}_s}{\|\vec{g}_s\|} \times \vec{E}_\xi, \quad \vec{E}_s = \vec{E}_\xi \times \vec{E}_r, \quad \vec{E}_\xi = \frac{\vec{g}_\xi}{\|\vec{g}_\xi\|} \tag{2.9}$$

The key ingredients in the element formulation are the specific interpolations used for the membrane and transverse shear strains. Many different possibilities are available but the difficulty is to obtain an effective element, that is spatially isotropic, passes the patch tests, and performs well in bending-dominated and in membrane-dominated problems. The interpolations presented in Ref. [1] are leading to quite an effective element and are

$$\begin{aligned} \tilde{e}_{rr} &= a_{1i} + b_{1i}r + c_{1i}s \\ \tilde{e}_{ss} &= a_{2i} + b_{2i}r + c_{2i}s \\ \tilde{e}_{qq} &= a_{3i} + b_{3i}r + c_{3i}(1 - r - s) \end{aligned} \tag{2.10}$$

for the in-plane strains, as denoted by the subscript i on the coefficients, where $\tilde{e}_{qq} = \frac{1}{2}\left(\tilde{e}_{rr} + \tilde{e}_{ss}\right) - \tilde{e}_{rs}$ and

$$\begin{aligned} \tilde{e}_{r\xi} &= a_{1t} + b_{1t}r + c_{1t}s + s(d_t r + e_t s) \\ \tilde{e}_{s\xi} &= a_{2t} + b_{2t}r + c_{2t}s - r(d_t r + e_t s) \end{aligned} \tag{2.11}$$

for the transverse shear strains, as denoted by the subscript t on the coefficients. We refer to Ref. [1] for details on how to obtain the coefficients in Eqs. (2.10) and (2.11). The interpolations with the tying points used are shown in Fig. 2-1.

However, as mentioned above already, and reported first in Ref. [51] the resulting element shows an instability in the analysis of certain shell problems, depending on the curvature and the boundary conditions of the shell structure. Fig. 2-2 shows this instability in the analysis of a hyperboloid shell, clamped at the bottom and free at

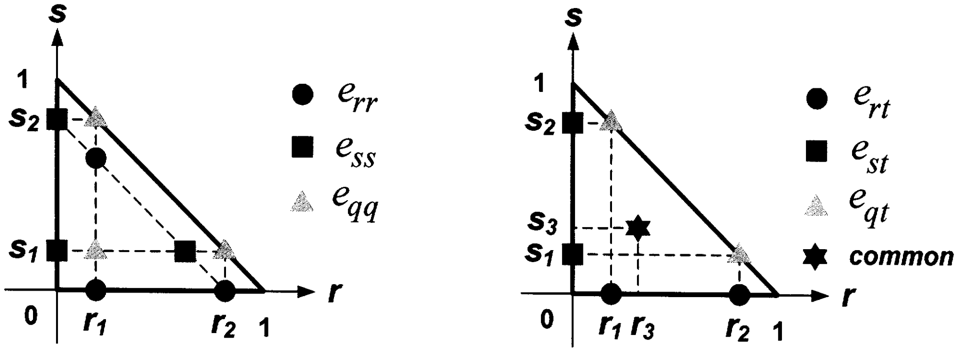

$$\tilde{e}_{rr} = a_{1i} + b_{1i} r + c_{1i} s$$
$$\tilde{e}_{ss} = a_{2i} + b_{2i} r + c_{2i} s$$
$$\tilde{e}_{qq} = a_{3i} + b_{3i} r + c_{3i} (1 - r - s)$$

$$\tilde{e}_{rt} = a_{1t} + b_{1t} r + c_{1t} s + s(d_t r + e_t s)$$
$$\tilde{e}_{st} = a_{2t} + b_{2t} r + c_{2t} s - r(d_t r + e_t s)$$

Figure 2-1: Interpolations and tying points used for the MITC6 shell element; $r_1 = s_1 = \frac{1}{2} - \frac{1}{2\sqrt{3}}$, $r_2 = s_2 = \frac{1}{2} + \frac{1}{2\sqrt{3}}$ and $r_3 = s_3 = \frac{1}{3}$

the top. These instabilities, even when seen only in the solution of certain problems, are clearly undesirable and a remedy needs to be introduced. Chapelle et al. [51, 52] discussed in depth the difficulty to obtain an improved triangular shell element that shows all the desirable properties and no instability, and presented a stabilization of the MITC6 element. However, as is typical in stabilized formulations [2, 6] a stabilization factor is introduced. In the next section we improve the original element formulation in a different way, without the use of a factor, while preserving the other desirable properties of the original element.

2.2 The improved MITC6 shell element

The basic approach in this formulation is as presented above. However, instead of using Eq. (2.5), we use the interpolation

$$\tilde{\hat{e}}_{ij}(r, s, \xi) = \sum_{k=1}^{n_{ij}} h_{ij}^k(r, s)\hat{e}_{ij}\Big|_{\left(r_{ij}^k, s_{ij}^k, \xi\right)} \tag{2.12}$$

where

$$\hat{e}_{ij} = e_{kl}\left(\vec{g}^k \cdot \hat{\vec{g}}_i\right)\left(\vec{g}^l \cdot \hat{\vec{g}}_j\right) \quad \text{with} \quad \hat{\vec{g}}_i(r, s, \xi) = \vec{g}_i\left(\tfrac{1}{3}, \tfrac{1}{3}, \xi\right) \tag{2.13}$$

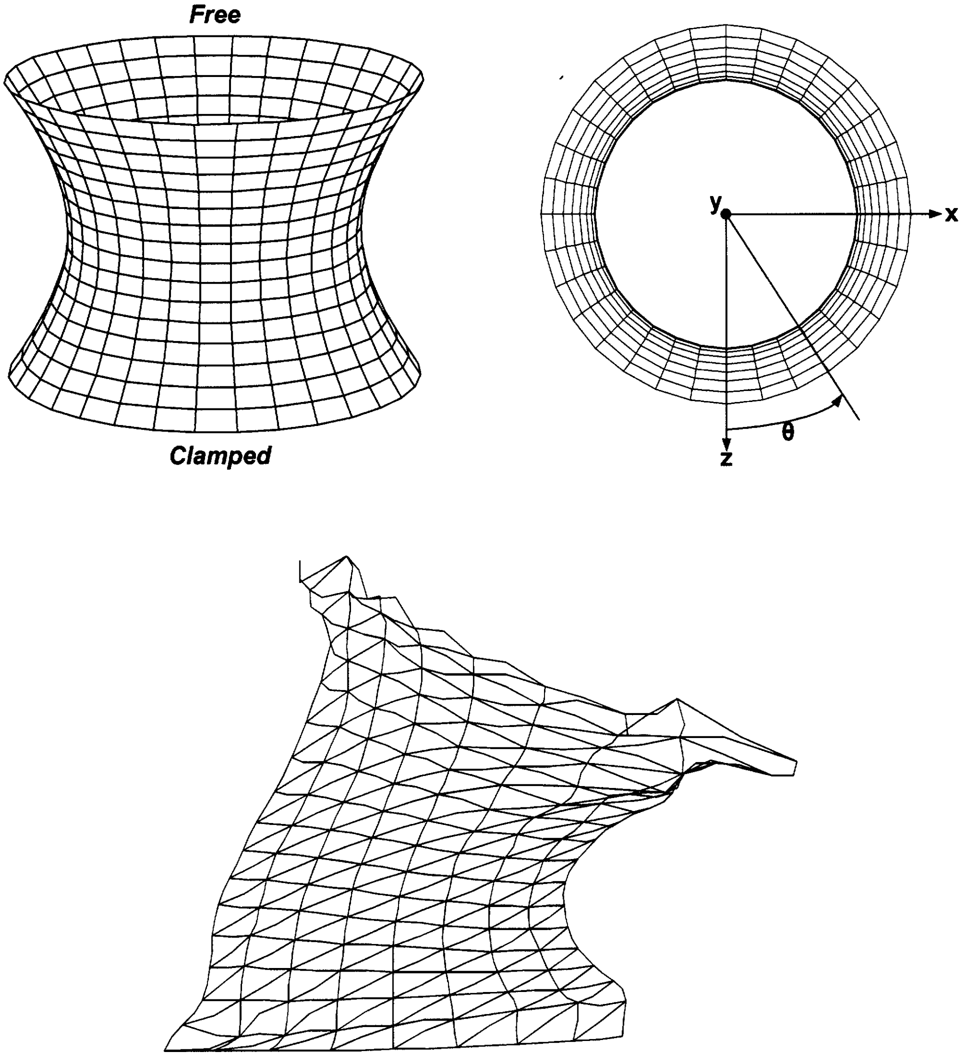

Figure 2-2: Analysis of a hyperboloid shell problem. The midsurface is given by $x^2 + z^2 = 1 + y^2 \quad (-1 \leq y \leq 1)$. The shell is fixed at its bottom and free at its top; $E = 2.0 \times 10^{11}$, $\nu = 1/3$, $t/L = 1/10000$ (where t denotes the thickness of the shell, see Sec. 2.3); the loading is the pressure loading $p(\theta) = p_0 \cos(2\theta)$, $p_0 = 1.0 \times 10^6$. The problem is solved using the original MITC6 shell element of Ref. [1].

Here we imply summation over the indices k and l, and the interpolation functions are those introduced in Ref. [1], see Fig. 2-1. Therefore, the same form of interpolation as given in Eqs. (2.5) and (2.6), is used in the improved element, but the interpolated strains are given in the basis $\left(\hat{\vec{g}}^r, \hat{\vec{g}}^s, \hat{\vec{g}}^\xi\right)$ and the $\hat{e}_{ij}$ are employed instead of the e_{ij} to evaluate the coefficients of the interpolation functions. Except for using the base vectors $\left(\hat{\vec{g}}_r, \hat{\vec{g}}_s, \hat{\vec{g}}_\xi\right)$, constant in r and s, in the interpolations instead of the base vectors $(\vec{g}_r, \vec{g}_s, \vec{g}_\xi)$, there is no difference in the element formulations. Using Eq. (2.12) the strain terms in the Cartesian basis aligned with the normal shell direction are calculated for use of the plane stress constitutive law.

Note that, when the element is flat and straight-sided, the base vectors $(\vec{g}_r, \vec{g}_s, \vec{g}_\xi)$ are constant throughout the element, and the interpolations given in Eqs. (2.12) and (2.13) reduce to those of the original MITC6 element. Hence identical results are obtained when plate problems are solved.

We shall see in the tests given below that the improved element does not display the instability of the original element and performs quite well. The reason is that all displacement-based strains couple into the interpolated membrane and shear strain components. In some respects, a more natural approach is to use membrane and shear strain interpolations as in Eq. (2.5), but with different interpolation functions and tying points than employed in the original MITC6 shell element. Many different schemes can be explored but - with the criteria to be satisfied - it appears difficult to reach in this way a significantly improved shell element, see Refs. [1,52].

2.3 Solution of test problems

In this section we report on the performance of the improved MITC6 shell element. As mentioned already, the element is isotropic, hence the test of Fig. 2-3 is passed. The element contains only the rigid body modes, no spurious zero energy modes, and passes the membrane and bending patch tests, see Fig. 2-4 and Table 2.1.

Of particular interest is the solution of the problem considered in Fig. 2-2, to see whether spurious displacements are obtained. Fig. 2-5 shows the result using the

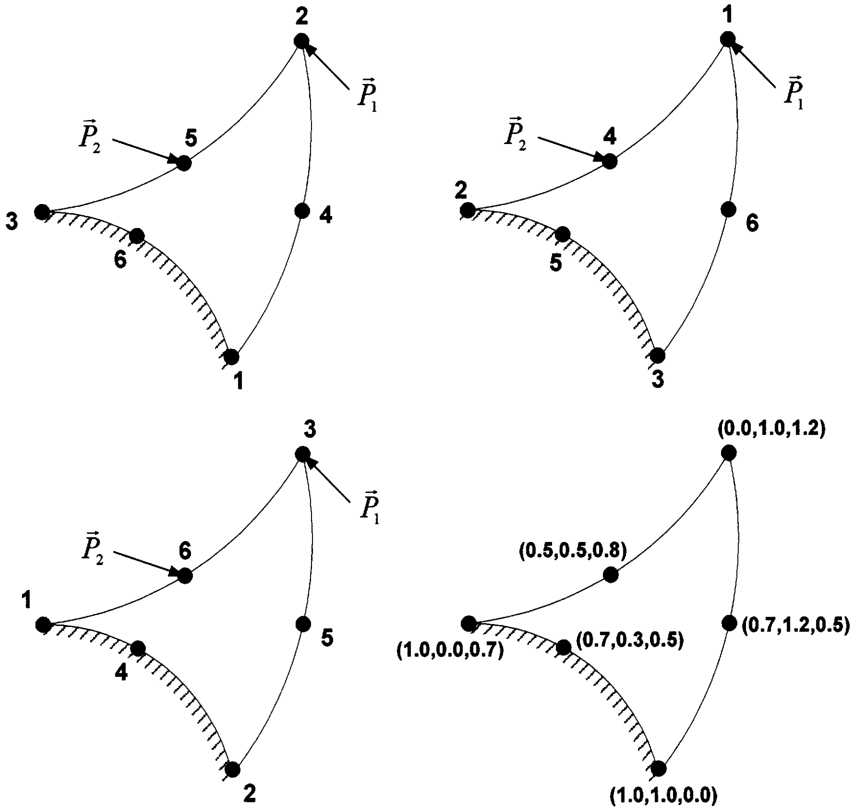

Figure 2-3: Isotropic element test of the 6-node triangular shell element, taken from Ref. [1]

Table 2.1: Basic test results of MITC6 shell elements

Element	Isotropic element test	Zero energy mode test	Membrane patch test	Bending patch test
The original MITC6	Pass	Pass	Pass	Pass
The improved MITC6	Pass	Pass	Pass	Pass

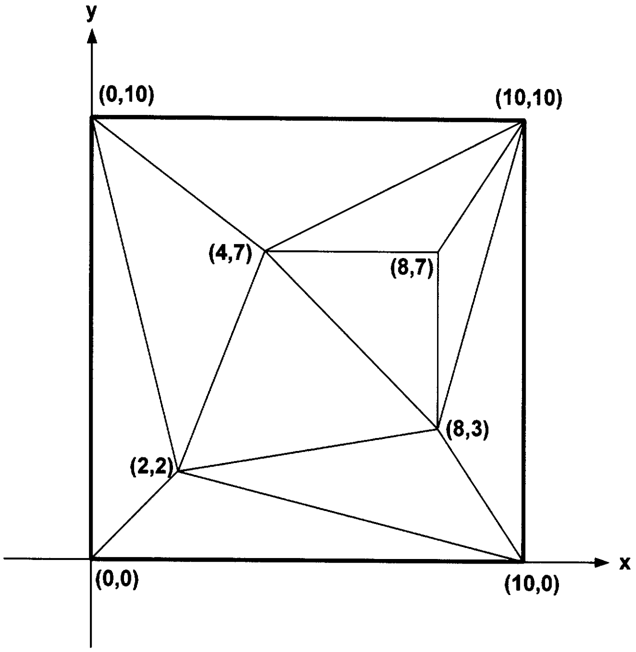

Figure 2-4: Mesh used for patch tests

improved MITC6 shell element and we see that no spurious displacements occur.

In the further tests, we evaluate the s-norm introduced in Ref. [36] to measure the rate of convergence, since this norm can be applied in bending-dominated and membrane-dominated shell problems. The relative error is defined as [1, 2, 36]

$$\text{relative error} = \frac{\|\vec{u}_{ref} - \vec{u}_h\|_s^2}{\|\vec{u}_{ref}\|_s^2} \tag{2.14}$$

where $\vec{u}_{ref}$ denotes the reference solution. We consider below the problems solved in Ref. [1]. For each problem, we use $\vec{u}_{ref}$, the solution obtained with a fine enough reference mesh.

In these test results we consider only structures of constant thickness, t. Hence t/L denotes the thickness over length ratio, as e.g. in Refs. [1, 2].

2.3.1 Analysis of clamped plate problem

The plate problem considered is shown in Fig. 2-6 and the convergence results are given in Fig. 2-7. These results should be identical to those reported for the MITC6

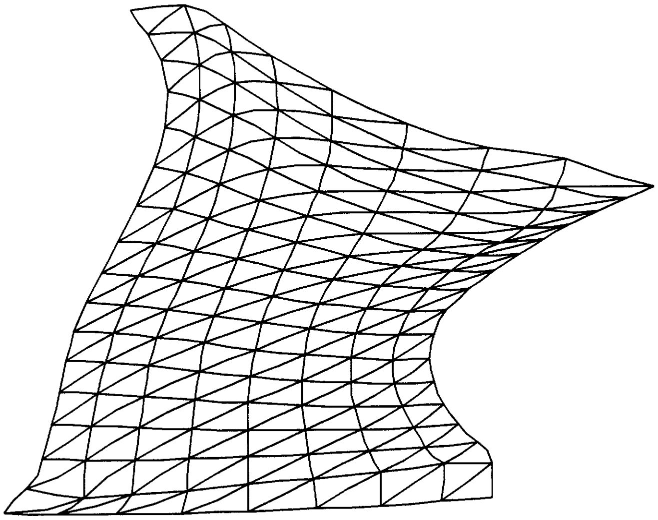

Figure 2-5: Shell problem of Fig. 2-2 solved with the improved MITC6 shell element

shell element in Ref. [1], and indeed are for individual nodal displacements. However, slight differences in the relative errors are observed because the s-norms were calculated using different implementations.

2.3.2 Analysis of cylindrical shell problems

The geometry and the loading of the problems are defined in Fig. 2-8. Depending on the boundary conditions used, a membrane-dominated problem (clamped boundary conditions) and a bending-dominated problem (free ends) are obtained [1, 2]. We solve both problems and the results are given in Fig. 2-9. The same good convergence behavior as reported in Ref. [1] is seen.

2.3.3 Analysis of hyperboloid shell problems

The MITC6 shell element performs very well in the analysis of the plate and cylindrical shell problems. However, these shells have rather simple surfaces, the plate is flat and the cylinder has one principal curvature equal to zero.

Two much more discriminating problems are obtained when considering the hyperboloid shell shown in Fig. 2-2. A membrane-dominated problem is obtained by

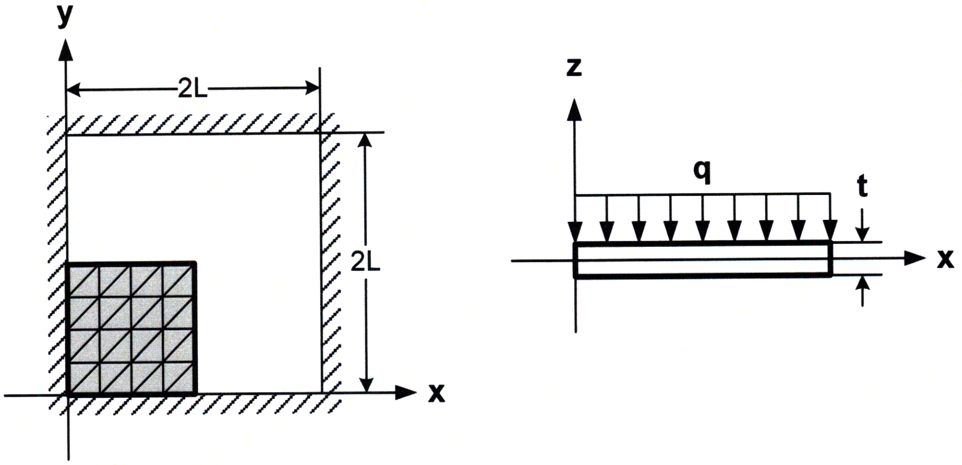

Figure 2-6: Clamped plate subjected to uniform pressure; $L = 1.0$, $E = 1.7472 \times 10^7$, $\nu = 0.3$ and $q = 1.0$

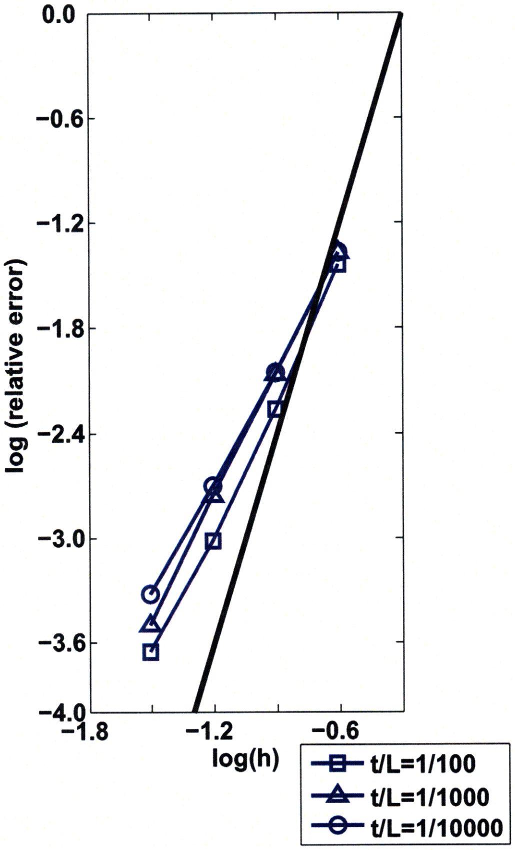

Figure 2-7: Convergence curves for the clamped plate problem. The bold line shows the optimal convergence rate.

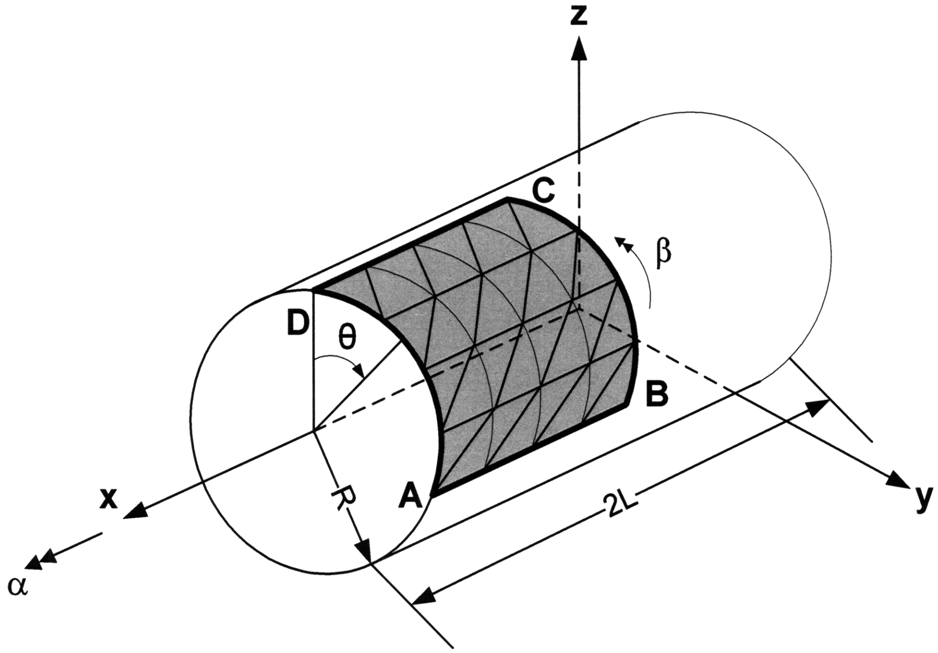

Figure 2-8: Cylindrical shell problem; pressure loading $p(\theta) = p_0 \cos(2\theta)$; both ends are either clamped or free, see Refs. [1, 2]; $L = R = 1.0$, $E = 2.0 \times 10^5$, $\nu = 1/3$ and $p_0 = 1.0$

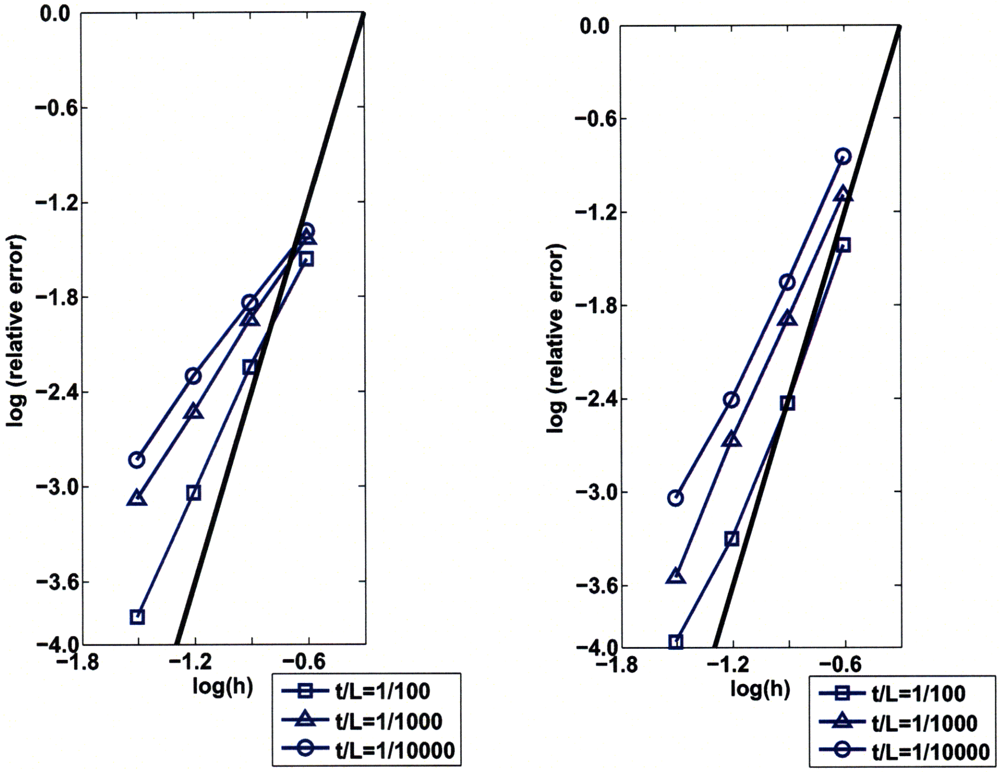

(a)

(b)

Figure 2-9: Convergence curves for the cylindrical shell problem (a) when both ends are clamped and (b) when both ends are free. The bold lines show the optimal convergence rate.

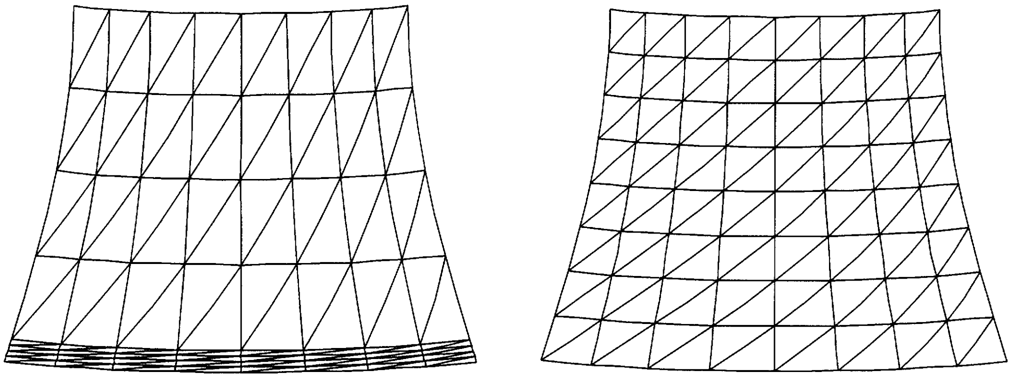

(a) (b)

Figure 2-10: Meshes used for 1/8th of the hyperboloid shell (8 × 8 element mesh) with symmetry boundary conditions applied. The geometry, material properties and loading are as in Fig. 2-2. (a) The graded mesh is used when both ends are fixed and (b) the uniform mesh is used when both ends are free. The boundary layer of width $6\sqrt{t}$ is meshed in the graded mesh [1].

considering clamped-clamped conditions and a bending-dominated problem is obtained when considering both edges to be free. It is important to mesh appropriately the boundary layer in the case of the clamped case [2,57], and we use the meshing of Ref. [1], where half the mesh is used in the boundary layer of width $6\sqrt{t}$, see Fig. 2-10. The very thin boundary layer present in the free case is not specially meshed. Fig. 2-11 shows the results obtained which are quite close to those reported for the original MITC6 shell element [1].

While the convergence behavior is quite good, of course, the element does not show optimal behavior, which would correspond to the optimal rate of convergence and no shift in the convergence curves when the ratio t/L decreases.

Finally we calculate the convergence curves of the element in the solution of the clamped hyperboloid in the A_m norm, that is, we evaluate

$$\text{relative error} = \frac{A_m\left(\vec{u}_{ref} - \vec{u}_h\,,\ \vec{u}_{ref} - \vec{u}_h\right)}{A_m\left(\vec{u}_{ref}\,,\ \vec{u}_{ref}\right)} \tag{2.15}$$

where $A_m\left(\cdot,\cdot\right)$ is the exact bilinear form containing the membrane and shear strain contributions. As well known, displacement-based elements show excellent conver-

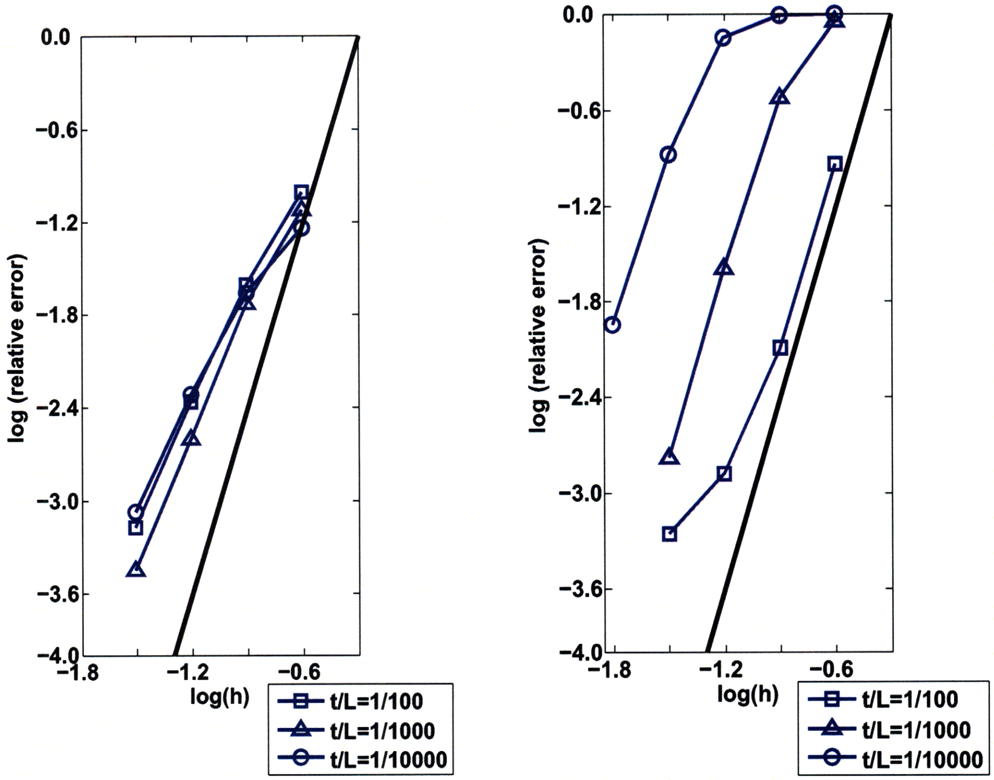

(a)

(b)

Figure 2-11: Convergence curves for the hyperboloid shell problem (a) when both ends are clamped and (b) when both ends are free. The bold lines show the optimal convergence rate.

gence in this norm when membrane dominated problems are solved, and indeed display optimal behavior when properly graded meshes are used [2]. To calculate A_m and $\vec{u}_{ref}$ we use the displacement-based 6-node triangular shell element with a mesh of 128 × 128 elements.

Since the solution $\vec{u}_h$ obtained with the MITC6 shell element will be different from the displacement-based solution, this measure for convergence is very discriminating. Any small difference in the calculated shell section displacements and rotations is magnified in the norm by the fact that the displacement-based element formulation locks when solving bending dominated problems.

Figs. 2-12 and 2-13 show the results obtained using Eq. (2.15). We also show the behaviors of the displacement-based 6-node triangular shell element and the original MITC6 shell element, and the results when excluding the transverse shear strain effects. The figures show that reasonable convergence is measured with the improved MITC6 shell element, and that the errors are substantially less when the shear strain effects are excluded. The shear strain error is largely due to errors in the nodal rotations which cause spurious shear stresses. Fig. 2-14 displays the rotations for one case of number of elements used, and we see that the improved MITC6 shell element result, compared with the original element result, is closer to the displacement-based solution.

2.3.4 A brief study using a stabilized shell element formulation

Here we want to briefly show how a formulation like the one given in Ref. [51] based on stabilization performs in the solution of the problem of Fig. 2-2. As pointed out already above, the major concern using the stabilization approach is that a factor has to be set. Hence we focus on the use of different values of the stabilization factor.

We obtain a stabilized shell element of the original MITC6 shell element by replacing a part of the mixed-interpolated shear strain by the unreduced displacement-based

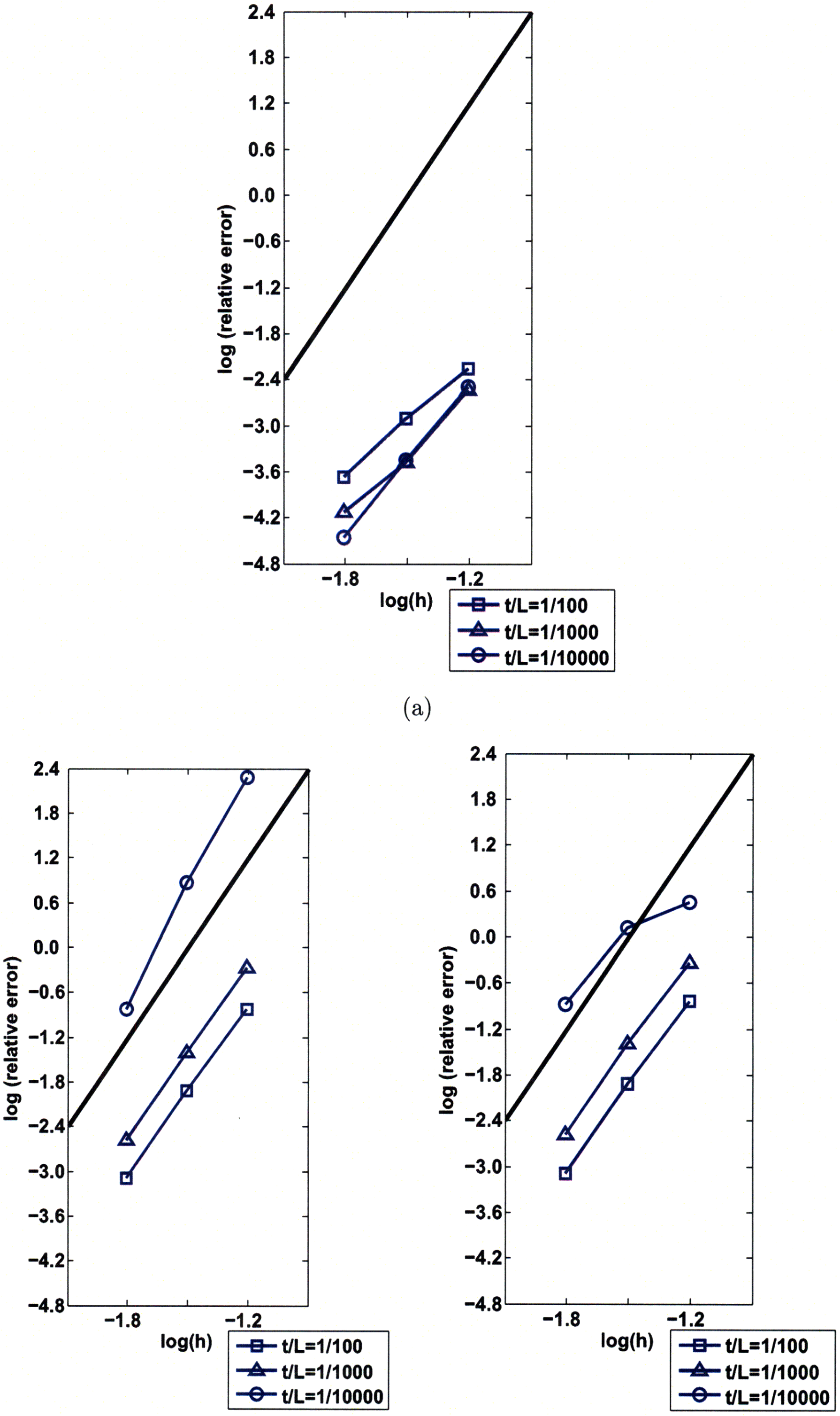

(a)

(b)

(c)

Figure 2-12: Convergence curves in the A_m norm for the fully clamped hyperboloid shell problem solved using (a) the displacement-based 6-node element, (b) the original MITC6 element and (c) the improved MITC6 element. Graded meshes are used as shown in Fig. 2-10(a).

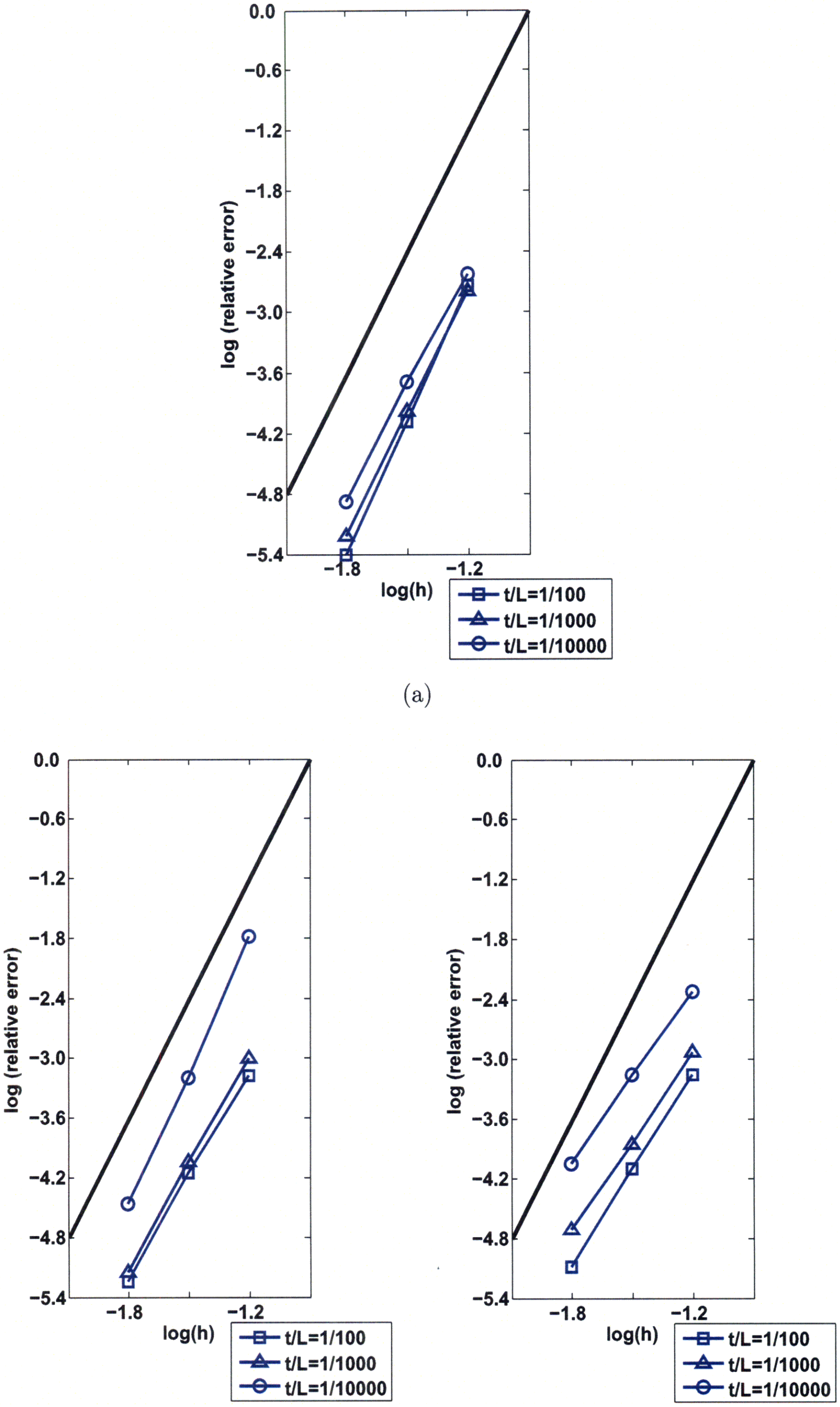

(a)

(b)

(c)

Figure 2-13: Convergence curves in the A_m norm without shear terms for the fully clamped hyperboloid shell problem solved using (a) the displacement-based 6-node element, (b) the original MITC6 element and (c) the improved MITC6 element. Graded meshes are used as shown in Fig. 2-10(a).

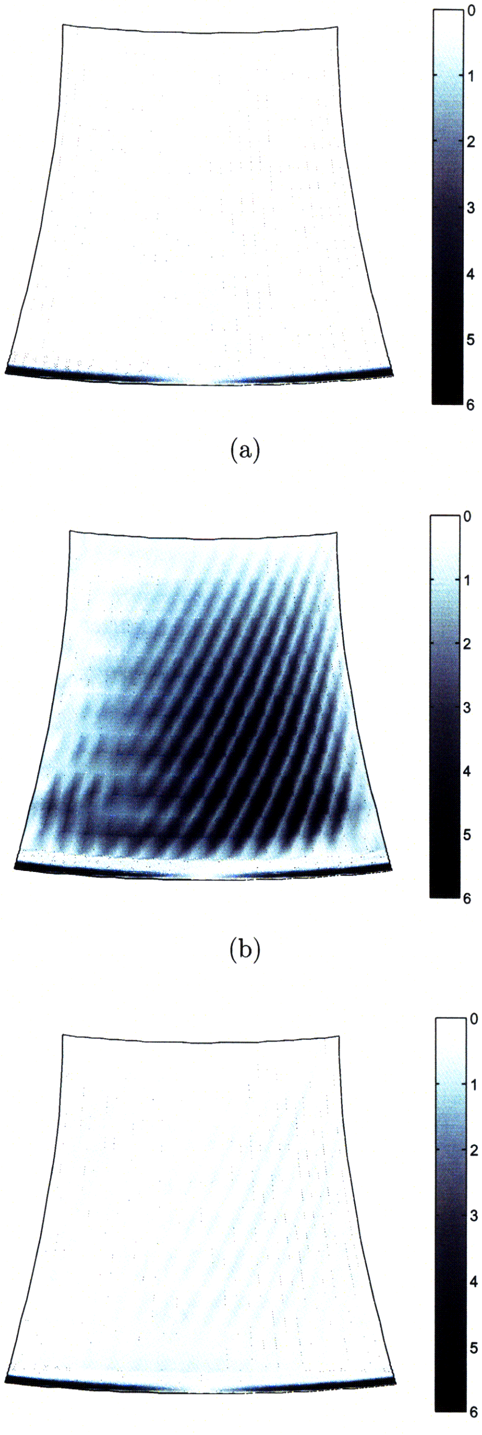

(a)

(b)

(c)

Figure 2-14: Rotation magnitudes $\left(\sqrt{\alpha^2+\beta^2}\right)$ of the fully clamped hyperboloid shell problem solved using (a) the displacement-based 6-node element, (b) the original MITC6 element and (c) the improved MITC6 element. The 16×16 graded mesh is used with $t/L = 1/10000$.

shear strain, see Refs. [2,6,51].

$$
\begin{aligned}
\tilde{e}_{r\xi} &= \left(1 - C\frac{h_T}{L}\right)\tilde{e}_{r\xi}^{MITC6} + C\frac{h_T}{L}e_{r\xi}^{DI} \\
\tilde{e}_{s\xi} &= \left(1 - C\frac{h_T}{L}\right)\tilde{e}_{s\xi}^{MITC6} + C\frac{h_T}{L}e_{s\xi}^{DI}
\end{aligned}
\tag{2.16}
$$

where $\tilde{e}_{r\xi}^{MITC6}$ and $\tilde{e}_{s\xi}^{MITC6}$ are the shear strains calculated from the MITC6 strain interpolation in Eq. (2.11) and $e_{r\xi}^{DI}$ and $e_{s\xi}^{DI}$ are the strains obtained from the displacement interpolation in Eq. (2.3). In Eq. (2.16), C is the stabilization factor to be set, h_T is a measure of the element size and L is the characteristic length. For the problems we consider, $L = 1$ and we use h_T to be the radius of the circumscribed circle around the corner points of the triangular element. This stabilization operates on the transverse shear strains whereas the procedure of Ref. [51] operates on the shear strain energy. We expect that a similar stabilization is achieved with the two techniques, but the method using the above strain expressions is more easily applied.

Fig. 2-15 shows the deformations of the shell considered in Fig. 2-2 when three different values of C are used. As seen, the deformations of the shell are quite sensitive to the value of C, but once the stabilization factor is large enough, the instability of the original MITC6 element is no longer present. Hence it appears that simply a large enough value of C needs to be selected.

However, clearly, if the stabilization factor is too large, the error in the response prediction (displacements and stresses) is significant, see Ref. [51]. We demonstrate this deterioration of the response prediction in Table 2.2 for the analysis of the clamped plate problem of Fig. 2-6. Here the stabilization is not needed but when used with values as in Fig. 2-15, the response prediction is much deteriorating.

Hence a major difficulty when using this stabilization approach is to choose the optimal stabilization factor automatically for each element for any shell analysis, including also nonlinear analysis. This is hardly possible but assuming that it is achieved, we may find thereafter that the accuracy of the solution results is not acceptable.

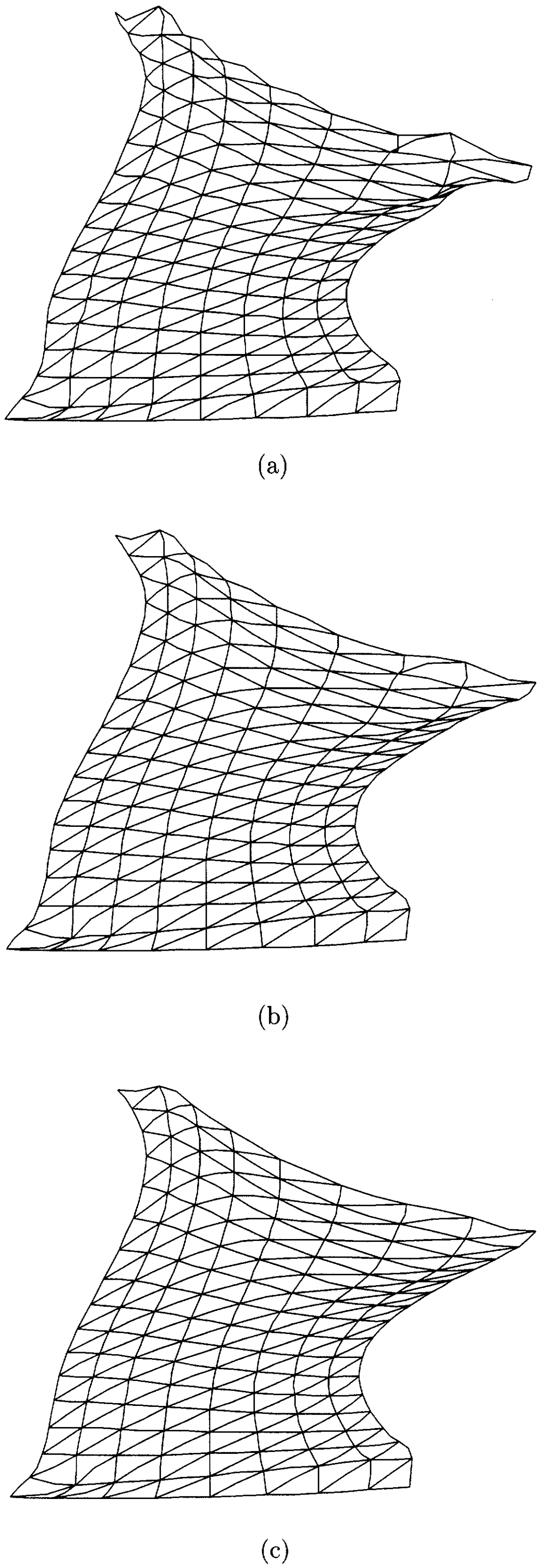
(a)

(b)

(c)

Figure 2-15: Shell problem of Fig. 2-2 solved with the stabilized MITC6 shell element. (a) $C = 0.1$, (b) $C = 0.2$ and (c) $C = 0.4$

Table 2.2: Normalized maximum displacements of the clamped plate problem in Fig. 2-6

Improved MITC6	$t/L = 1/100$	$t/L = 1/1000$	$t/L = 1/10000$
4×4	1.020307	1.014698	1.014628
8×8	1.012138	1.009567	1.009512
16×16	1.006941	1.005911	1.005839
Stabilized MITC6 ($C = 0.1$)	$t/L = 1/100$	$t/L = 1/1000$	$t/L = 1/10000$
4×4	1.019691	0.967412	0.306133
8×8	1.012110	1.008506	0.964094
16×16	1.006935	1.005893	1.004342
Stabilized MITC6 ($C = 0.4$)	$t/L = 1/100$	$t/L = 1/1000$	$t/L = 1/10000$
4×4	1.010283	0.698071	0.026907
8×8	1.011874	0.996715	0.673236
16×16	1.006914	1.005626	0.994437

2.4 Concluding Remarks

The objective in this chapter was to present a triangular shell element which represents a significant improvement over an earlier published element [1]. Like the earlier presented element, the improved 6-node element is based on the MITC formulation approach and has all the attractive attributes of MITC shell elements, with respect to ease of use and computational effectiveness. Actually, the changes in the formulation of the earlier element to reach the improvements are quite simple.

The formulation of the improved MITC6 shell element given here specifically addresses the peculiar unstable behavior reported in Ref. [51] observed with the earlier published 6-node element [1] in the solution of certain shell problems. Specific shell geometries and boundary conditions allow the instability to occur. The improved MITC6 shell element does not show this behavior and in the other test problems performs practically as well as the earlier published element. In plate analyses the same results as earlier are obtained.

While the shell element does not show uniformly optimal behavior in all analyses, a property that is extremely difficult to reach [2], it shows good convergence behavior. A mathematical analysis of the element would be very valuable and could yield insight into how the element might be further improved.

Chapter 3

A model for large strain anisotropic elasto-plasticity

Accurate modeling of the elasto-plastic deformations of metals is very important not only for the simulation of the manufacturing process but also for the analysis of the final components during their service, for example consider the simulation of car crash or crush conditions. Many metallic goods are made from cold-rolled sheets. Rolling, as well as many other manufacturing procedures, induces anisotropy in the metals. Anisotropy manifests itself in that the physical properties depend on the directions along which they are measured. Hence the constants determining the elastic and plastic properties, notably the Young's moduli and yield stresses become dependent on the direction of testing. An accurate computational model must take into account the directions of both the elastic and plastic properties, as well as their evolution with plastic strains.

Most computational simulations are currently using continuum models and finite element procedures, see for example [6, 41]. Since the 1990s simulations of isotropic elasto-plasticity at large strains have achieved reasonable accuracy and efficiency [58], using combined isotropic-kinematic hardening [59] and consistently linearized implicit implementations [37, 60]. The principal ingredients of the most successful elasto-plastic implementations at large strains are the use of the multiplicative or Lee decomposition [61], hyperelasticity in terms of the logarithmic strains and the exponential function to integrate the plastic gradient [60,62]. The multiplicative decomposition is based on micromechanical observations and uses the existence of an intermediate, local, configuration uniquely determined from the historical evolution of the local plastic flow (both plastic strain and plastic rotation tensors) [3]. An advantage of the use of the Lee decomposition is that, since the elastic stretch tensor is explicitly obtained, the total elastic strains may be directly computed from the deformation gradient. Then, the use of a stored energy function gives stresses without resorting to 'rate' expressions [63–66], thus avoiding any algorithmic objectivity issue and dissipation during purely elastic strain paths [67,68].

However, the Lee decomposition presents important computational issues due to its multiplicative character, inserting the Mandel stress tensor in the dissipation expression [3,37]. The resulting difficulties are bypassed in the case of isotropic elasticity using logarithmic strains and the exponential mapping. In isotropic elasticity the stress and elastic strain tensors commute and the Mandel stress tensor coincides with the rotated Kirchhoff stress tensor [6,60]. A physically motivated hyperelastic function of the logarithmic strains [69,70] may be employed. Retaining the linear term of the Taylor series of the exponential mapping for the integration of the plastic flow, a very simple algorithm is obtained [60], in which the large strains framework acts as a simple pre- and post-processor of the usual small strains algorithm, even for obtaining the algorithmic tangent [37]. It should be noted that with these algorithms any anisotropic yield function could be used and the plastic flow is computed using the corresponding small strains algorithm.

However, for the case of anisotropic elasticity, stresses and elastic strains do not commute in general and the dissipation equation presents major mathematical difficulties. Hence some researchers adopt formulations that rely on additive decompositions, see for example Refs. [71,72], elastic isotropy [73–75] or other complex frameworks more difficult to implement in an implicit finite element code [76–79]; see also some criticisms in Ref. [80]. In summary, those algorithms do not retain the successful properties of the previously mentioned algorithms for isotropic elasticity.

The above-mentioned anisotropic elasto-plastic algorithms as well as the vast majority of the computational algorithms for anisotropic plasticity of continua do not take into account the possible evolution of the material symmetries. However, the evolution of the material symmetries with nonproportional plastic strains is intuitive and has been observed experimentally, see for example Refs. [4,81–84] . This evolution is closely related to the texture evolution of the microstructure, also observed experimentally, see for example Refs. [78,85–94] . Texture evolution involves both changes in the yield function and in the preferred directions. In practice, as a first approximation, the yield function evolution may be taken into account through isotropic and kinematic hardening of the original anisotropic yield function. This approximation has given good results [4, 5, 74, 75, 81, 95], even if constant normalized parameters of the Hill yield function are used for a wide range of plastic strains [3, 4].

For an accurate simulation, the rotation of the preferred directions must also be taken into account. In crystal plasticity, the lattice rotation and the plastic spin are closely related by the Schmidt law. In continuum plasticity, the physical meaning of the plastic spin has been much discussed even for the case of isotropic elasticity, see for example [46-51]. The usual choice in isotropic elasticity is a vanishing plastic spin. This is a natural choice for isotropic elasticity because the plastic spin does not appear in the dissipation equation and does not affect the stored or dissipated energies [3]. Indeed, since there is no preferred orientation, in average, the microstructure should not show any rotation preference. However, in the case of elastic anisotropy, the stress tensor in the dissipation equation is the unsymmetric Mandel stress tensor, which produces work on the plastic spin, and hence needs to be accounted for in the energy balance equations. In addition, the evolution of the material symmetries also produces a change in the stored energy in the case of anisotropy. In Ref. [3], a framework for anisotropic elasto-plasticity using logarithmic strains, the multiplicative decomposition and the exponential mapping is presented. The model takes into account the evolution of the orthotropic preferred directions and was shown to predict the experimental results of Ref. [4] for material symmetry evolution. These simulations are also used in this chapter to gain further insight into the meaning of the material parameters. Central to the model is the importance of the evolution of the preferred directions and the effect on both the stored energy and the dissipation terms. This is an important difference with other works in which such evolution is also taken into account but through ad-hoc constitutive equations for the plastic spin [4,5,74,75,95].

In this chapter we present results of some studies on the model of Ref. [3] in order to obtain deeper insight into the use of the parameters for the constitutive equations and the effects that may be simulated, as for example the cross effect during path changes on the plastic strains.

In the following, we first outline the main features of the model of Ref. [3], focusing on the rotation of the orthotropic directions. Next, we discuss the effect of the parameters on the predictions with physical interpretations and give some results comparing with physical test data. For a constitutive model, a simple procedure to obtain the material parameters is always desirable. We present a procedure to obtain the spin parameters from Lankford R-values and the predictions are compared to those of Ref. [5]. Thereafter, we give some results regarding the predictability of the model in nonproportional loading conditions. Finally, in the last section of the chapter, we present our conclusions of this work.

3.1 The Montáns-Bathe model

In this section we review the ingredients of the Montáns-Bathe model. A detailed description is given in Ref. [3]. We follow the notation of Refs. [6,58].

3.1.1 Kinematics

The model is based on the Lee decomposition which leads to the following multiplicative decomposition for the deformation gradient

$$ {}^{t}_{0}\boldsymbol{X} = {}^{t}_{0}\boldsymbol{X}^{e}\, {}^{t}_{0}\boldsymbol{X}^{p} \tag{3.1}$$

where ${}^{t}_{0}\boldsymbol{X}$ is the deformation gradient and ${}^{t}_{0}\boldsymbol{X}^{e}$ and ${}^{t}_{0}\boldsymbol{X}^{p}$ represent its elastic and plastic part respectively. The left superscript denotes always the current configuration while the left subscript represents the reference configuration. We will omit these left indices when confusion is hardly possible. The spatial velocity gradient is

$$ {}^{t}\boldsymbol{l} = {}^{t}_{0}\dot{\boldsymbol{X}}\,{}^{t}_{0}\boldsymbol{X}^{-1} = {}^{t}_{0}\dot{\boldsymbol{X}}^{e}\left({}^{t}_{0}\boldsymbol{X}^{e}\right)^{-1} + {}^{t}_{0}\boldsymbol{X}^{e}\left[{}^{t}_{0}\dot{\boldsymbol{X}}^{p}\left({}^{t}_{0}\boldsymbol{X}^{p}\right)^{-1}\right]\left({}^{t}_{0}\boldsymbol{X}^{e}\right)^{-1} \tag{3.2} $$

We use the modified plastic velocity gradient defined in the intermediate stress-free configuration

$$ {}^{t}\boldsymbol{L}^{p} = {}^{t}_{0}\dot{\boldsymbol{X}}^{p}\left({}^{t}_{0}\boldsymbol{X}^{p}\right)^{-1} \tag{3.3} $$

whose symmetric part is the modified plastic deformation rate tensor ${}^{t}\boldsymbol{D}^{p}$ while its skew part is the modified plastic spin tensor ${}^{t}\boldsymbol{W}^{p}$. Eq. (3.3) provides the differential equation for the evolution of the plastic deformation gradient

$$ {}^{t}_{0}\dot{\boldsymbol{X}}^{p} = {}^{t}\boldsymbol{L}^{p}\,{}^{t}_{0}\boldsymbol{X}^{p} \tag{3.4} $$

whose backward-Euler exponential solution is given by

$$ {}^{t+\Delta t}_{0}\boldsymbol{X}^{p} = \exp\left(\Delta t\ {}^{t+\Delta t}\boldsymbol{L}^{p}\right){}^{t}_{0}\boldsymbol{X}^{p} \tag{3.5} $$

For small steps ($\|\Delta t\ {}^{t+\Delta t}\boldsymbol{L}^{p}\| \ll 1$, a common restriction in plasticity formulations based on logarithmic strains), the exponential function can be approximated by

$$ \exp\left(\Delta t\ {}^{t+\Delta t}\boldsymbol{L}^{p}\right) \approx \exp\left(\Delta t\ {}^{t+\Delta t}\boldsymbol{D}^{p}\right)\exp\left(\Delta t\ {}^{t+\Delta t}\boldsymbol{W}^{p}\right) \tag{3.6} $$

Then we have the following update formulas

$$ \left({}^{t+\Delta t}_{0}\boldsymbol{X}^{p}\right)^{-1} = \left({}^{t}_{0}\boldsymbol{X}^{p}\right)^{-1}\exp\left(-\Delta t\ {}^{t+\Delta t}\boldsymbol{W}^{p}\right)\exp\left(-\Delta t\ {}^{t+\Delta t}\boldsymbol{D}^{p}\right) \tag{3.7a} $$

$$ {}^{t+\Delta t}_{0}\boldsymbol{X}^{e} = \boldsymbol{X}^{e}_{*}\exp\left(-\Delta t\ {}^{t+\Delta t}\boldsymbol{W}^{p}\right)\exp\left(-\Delta t\ {}^{t+\Delta t}\boldsymbol{D}^{p}\right) \tag{3.7b} $$

where $\boldsymbol{X}^e_* = {}^{t+\Delta t}_{\ \ \ t}\boldsymbol{X}\ {}^{t}_{0}\boldsymbol{X}^e$ is the trial elastic deformation gradient. Now we define the incremental plastic rotation as

$$ {}^{t+\Delta t}_{\ \ \ t}\boldsymbol{R}^w = \exp\left(\Delta t\ {}^{t+\Delta t}\boldsymbol{W}^p\right) \tag{3.8} $$

Using Eqs. (3.7b) and (3.8) and the logarithm strains defined by $2\boldsymbol{E}^e = \ln \boldsymbol{C}^e$ where $\boldsymbol{C}^e = \boldsymbol{X}^{eT}\boldsymbol{X}^e$ is the right Cauchy-Green deformation tensor, we can derive the following update scheme for the strains (see details in Ref. [37])

$$ {}^{t+\Delta t}_{\ \ \ 0}\underset{\leftarrow}{\boldsymbol{E}}^e \approx \underset{\leftarrow}{\boldsymbol{E}}^e_* - \Delta t\ {}^{t+\Delta t}\underset{\leftarrow}{\boldsymbol{D}}^p \tag{3.9} $$

We define $\underset{\leftarrow}{(\cdot)}$ as the quantity $(\cdot)$ rotated to the configuration where the plastic rotations are frozen during the plastic flow such that

$$ \underset{\leftarrow}{(\cdot)} = {}^{t+\Delta t}_{\ \ \ t}\boldsymbol{R}^{w^T}\,(\cdot)\,{}^{t+\Delta t}_{\ \ \ t}\boldsymbol{R}^w \tag{3.10} $$

Note that $\boldsymbol{E}^e_*$ is given by the trial elastic deformation gradient, and ${}^{t+\Delta t}_{\ \ \ t}\boldsymbol{R}^w$ is not involved in Eq. (3.9) and only known after integrations.

3.1.2 Dissipation inequality

The stored energy function is assumed to be of the type

$$ \mathcal{W} = \frac{1}{2}\boldsymbol{E}^e : \mathbb{A} : \boldsymbol{E}^e \tag{3.11} $$

where $\mathbb{A}$ is an elastic anisotropy tensor. Note that in Eq. (3.11) the strain tensor and the elastic anisotropy tensor are defined in the unrotated configuration where the elastic rotation is removed. During the plastic flow, this configuration and all objects defined in it rotate in each step by the amount ${}^{t+\Delta t}_{\ \ \ t}\boldsymbol{R}^w$ due to the plastic spin. However it has been observed that the anisotropy axes do not necessarily rotate as given by ${}^{t+\Delta t}_{\ \ \ t}\boldsymbol{R}^w$. Therefore we introduce an additional rotation for the anisotropy axes given by ${}^{t+\Delta t}_{\ \ \ t}\boldsymbol{R}^A$.

Then the rate of the stored energy function can be written as (for details see Ref. [3])

$$\dot{\mathcal{W}} = \underleftarrow{\boldsymbol{T}} : \dot{\underleftarrow{\boldsymbol{E}}}^{e} + \underleftarrow{\boldsymbol{T}}_{w} : \dot{\underleftarrow{\boldsymbol{W}}}^{A} = \boldsymbol{T} : \underleftarrow{\mathcal{L}}\boldsymbol{E}^{e} + \boldsymbol{T}_{w} : \boldsymbol{W}^{A} \tag{3.12}$$

where $\boldsymbol{T} = \mathbb{A} : \boldsymbol{E}^{e}$ is a symmetric tensor defined as a generalized Kirchhoff stress tensor which is work conjugate to the logarithmic strains, $\boldsymbol{T}_{w} = \boldsymbol{E}^{e}\boldsymbol{T} - \boldsymbol{T}\boldsymbol{E}^{e}$ is a skew tensor, $\boldsymbol{W}^{A} = \dot{\boldsymbol{R}}^{A}\boldsymbol{R}^{A^{T}}$ is a spin tensor for the anisotropy axes, and $\underleftarrow{\mathcal{L}}(\cdot)$ is a Lie derivative with ${}^{t+\Delta t}_{t}\boldsymbol{R}^{w}$ acting as a gradient.

Similarly we assume the following expression for the rate of the hardening potential

$$\dot{\mathcal{H}} = \underleftarrow{\boldsymbol{B}}_{s} : \dot{\underleftarrow{\boldsymbol{E}}}^{i} + \underleftarrow{\boldsymbol{B}}_{w} : \dot{\underleftarrow{\boldsymbol{W}}}^{H} + \kappa\dot{\zeta} + \kappa_{w}\dot{\xi} = \boldsymbol{B}_{s} : \underleftarrow{\mathcal{L}}\boldsymbol{E}^{i} + \boldsymbol{B}_{w} : \boldsymbol{W}^{H} + \kappa\dot{\zeta} + \kappa_{w}\dot{\xi} \tag{3.13}$$

where $\boldsymbol{B}_{s}$ is the backstress tensor, $\boldsymbol{E}^{i}$ are logarithmic strain-like internal variables and $\boldsymbol{B}_{w} = \boldsymbol{E}^{i}\boldsymbol{B}_{s} - \boldsymbol{B}_{s}\boldsymbol{E}^{i}$, the tensor $\boldsymbol{W}^{H}$ is the spin for the hardening anisotropy axes, the scalars κ and κ_{w} are the effective stress-like internal variables (current yield stress and couple-stress respectively) and the scalars ζ and ξ (effective plastic strain and effective plastic rotation) are the effective strain-like internal variables. For the evolution of the yield stress and the backstress, we use Prager's hardening model with the SPM (Splitting of Plastic Modulus) method, see Ref. [59], including the possibility of anisotropic kinematic hardening given by

$$\begin{aligned}
\kappa &= (1-M)\kappa_{0} + M\bar{\kappa} && (3.14)\\
&= (1-M)\kappa_{0} + M\left[\kappa_{\infty} - (\kappa_{\infty} - \kappa_{0})\exp(-\delta\zeta) + \bar{h}\zeta\right] \\
\dot{\underleftarrow{\boldsymbol{B}}}_{s} &= \frac{2}{3}(1-M)\frac{d\bar{\kappa}}{d\zeta}\underleftarrow{\mathbb{H}} : \underleftarrow{\boldsymbol{D}}^{p} && (3.15)
\end{aligned}$$

where M is the mixed hardening parameter, $\mathbb{H}$ is an anisotropy tensor for the kinematic hardening and κ_{∞}, κ_{0}, δ and $\bar{h}$ are material properties which govern the isotropic hardening curve.

Then the dissipation inequality becomes

$$\dot{\mathcal{D}}^{p} = \boldsymbol{\Xi}_{s} : \boldsymbol{D}^{p} + \boldsymbol{\Xi}_{w} : \boldsymbol{W}^{d} - \boldsymbol{B}_{s} : \underleftarrow{\mathcal{L}}\boldsymbol{E}^{i} - \boldsymbol{B}_{w} : \boldsymbol{W}^{H} - \kappa\dot{\zeta} - \kappa_{w}\dot{\xi} \geq 0 \tag{3.16}$$

where $\boldsymbol{\Xi}_s$ and $\boldsymbol{\Xi}_w$ are the symmetric part and the skew part of the Mandel stress tensor $\boldsymbol{\Xi} = \boldsymbol{C}^e\ \boldsymbol{S}$ (where $\boldsymbol{S}$ is the pull-back of the Kirchhoff stress $\boldsymbol{\tau}$ to the stress-free configuration) respectively and $\boldsymbol{W}^d = \boldsymbol{W}^p - \boldsymbol{W}^A$ is the dissipative spin tensor. The symmetric part and the skew part of the Mandel stress tensor can be related to the generalized Kirchhoff stress tensor by

$$\begin{aligned} \boldsymbol{\Xi}_s &= \boldsymbol{T} : \mathbb{S}^M && (3.17) \\ \boldsymbol{\Xi}_w &= \boldsymbol{T}_w = \boldsymbol{E}^e \boldsymbol{T} - \boldsymbol{T}\boldsymbol{E}^e && (3.18) \end{aligned}$$

where $\mathbb{S}^M$ is the fourth order mapping tensor which for small elastic strains is close to the identity tensor.

We assume that, without loss of generality, the elastic region is enclosed by two yield functions $f_s(\boldsymbol{\Xi}_s, \boldsymbol{B}_s, \kappa)$ and $f_w(\boldsymbol{\Xi}_w, \boldsymbol{B}_w, \kappa_w)$. Then the Lagrangian for the constrained problem is $L = \dot{\mathcal{D}}^p - \dot{t} f_s - \dot{\gamma} f_w$ where $\dot{t}$ and $\dot{\gamma}$ are the consistency parameters. By claiming that the principle of maximum dissipation holds ($\nabla L = 0$), we have the associated flow and hardening rules given by

$$\begin{cases} \dfrac{\partial L}{\partial \boldsymbol{\Xi}_s} = 0 \quad \Rightarrow \ \boldsymbol{D}^p = \dot{t}\dfrac{\partial f_s}{\partial \boldsymbol{\Xi}_s} & \text{and} \quad \dfrac{\partial L}{\partial \boldsymbol{\Xi}_w} = 0 \quad \Rightarrow \ \boldsymbol{W}^d = \dot{\gamma}\dfrac{\partial f_w}{\partial \boldsymbol{\Xi}_w} \\ \dfrac{\partial L}{\partial \boldsymbol{B}_s} = 0 \quad \Rightarrow \ \underleftarrow{\mathcal{L}}\boldsymbol{E}^i = -\dot{t}\dfrac{\partial f_s}{\partial \boldsymbol{B}_s} & \text{and} \quad \dfrac{\partial L}{\partial \boldsymbol{B}_w} = 0 \quad \Rightarrow \ \boldsymbol{W}^H = -\dot{\gamma}\dfrac{\partial f_w}{\partial \boldsymbol{B}_w} \\ \dfrac{\partial L}{\partial \kappa} = 0 \quad \Rightarrow \ \dot{\zeta} = -\dot{t}\dfrac{\partial f_s}{\partial \kappa} & \text{and} \quad \dfrac{\partial L}{\partial \kappa_w} = 0 \quad \Rightarrow \ \dot{\xi} = -\dot{\gamma}\dfrac{\partial f_w}{\partial \kappa_w} \end{cases} \tag{3.19}$$

3.1.3 Yield functions

We assume that the well-known Hill's quadratic yield criterion holds for the symmetric part of the Mandel stress tensor.

$$f_s = \frac{3}{2\kappa^2}(\boldsymbol{\Xi}_s - \boldsymbol{B}_s) : \mathbb{A}_s^p : (\boldsymbol{\Xi}_s - \boldsymbol{B}_s) - 1 = 0 \tag{3.20}$$

where $\mathbb{A}_s^p$ is the plastic anisotropy tensor assumed to have the same anisotropy directions as the elastic anisotropy tensor. Note that $\mathbb{A}_s^p$ extracts the deviatoric stresses only and therefore the mean stresses do not enter the yield condition in Eq. (3.20). From Eq. (3.19), we have

$$\begin{aligned} \underleftarrow{\mathcal{L}}\boldsymbol{E}^{i} &= \boldsymbol{D}^{p} = \frac{3}{\kappa^{2}}\mathbb{A}_{s}^{p} : (\boldsymbol{\Xi}_{s} - \boldsymbol{B}_{s})\,\dot{t} && (3.21) \\ \dot{\zeta} &= \frac{2}{\kappa}\dot{t} && (3.22) \end{aligned}$$

where $f_s = 0$ at yield is used in Eq. (3.22).

On the other hand, the Mises type of yield function is used for the skew part in this study

$$f_w = \|\boldsymbol{\Xi}_w\| - \sqrt{2}\kappa_w \tag{3.23}$$

where κ_w is the allowed yield value which may be set to zero. Then we have also from Eq. (3.19)

$$\begin{aligned} \boldsymbol{W}^{d} &= \dot{\gamma}\hat{\boldsymbol{\Xi}}_{w} && (3.24) \\ \dot{\xi} &= \sqrt{2}\dot{\gamma} && (3.25) \end{aligned}$$

where $\hat{\boldsymbol{\Xi}}_w = \boldsymbol{\Xi}_w / \|\boldsymbol{\Xi}_w\|$.

Note that Eq. (3.23) indicates that the plastic spin will take place once $\|\boldsymbol{\Xi}_w\|$ becomes larger than $\sqrt{2}\kappa_w$ regardless of the symmetric part of the plastic flow. However, this is inconsistent with experimental observations where a progressive rotation of the anisotropy axes is measured. Furthermore, in crystal plasticity the Schmidt law shows a clear relation between the plastic deformation rate tensor and the plastic spin tensor. Hence we propose the following relationship connecting the skew part with the symmetric part.

$$\dot{\xi} = \left(\frac{\langle f_w \rangle}{\eta}\right)^{m} \dot{\zeta} \tag{3.26}$$

where $\langle \cdot \rangle$ is the Macauley bracket function and η and m are material properties with η having the unit of stress. This viscoplastic-like law relates the plastic spin to the magnitude of the skew part of the Mandel stress tensor, and there is naturally no plastic spin when the skew part of the Mandel stress is zero (as usually assumed in isotropic plasticity).

3.2 Parametric study

We present in this section some parametric studies to obtain insight into the model. We discuss the physical meaning of the results and the effects that the material parameters for the skew part have on the predictions for some loading cases.

3.2.1 Constitutive equation for spin tensors

We assume the following constitutive equations for the spin tensors

$$\boldsymbol{W}^{axes} = \boldsymbol{W}^{p} + \boldsymbol{W}^{A} = -\rho \boldsymbol{W}^{d} \tag{3.27}$$

where $\boldsymbol{W}^{axes}$ is the total spin of the anisotropy axes with respect to the unrotated configuration (where the elastic rotation is removed). Then, from $\boldsymbol{W}^{d} = \boldsymbol{W}^{p} - \boldsymbol{W}^{A}$, we have

$$\begin{aligned} \boldsymbol{W}^{p} &= \frac{1}{2}(1-\rho)\boldsymbol{W}^{d} && (3.28) \\ \boldsymbol{W}^{A} &= -\frac{1}{2}(1+\rho)\boldsymbol{W}^{d} && (3.29) \end{aligned}$$

Eq. (3.27) implies that the spin of the anisotropy axes is proportional to the dissipative spin. In general ρ may be better modeled to be a function of the plastic deformation, but here we assume, as a first approximation, that ρ is constant. Note that the definition of ρ is slightly modified from the original definition proposed in Ref. [3].

We are able to establish a proper range of ρ based on physical reasoning. First we claim that the anisotropy axes rotate to a more favorable orientation after plastic flow such that the stored strain energy decreases. Therefore the second term in Eq. (3.12), which corresponds to the change in internal energy due to the anisotropy axes rotation, must be negative. This leads to, using Eqs. (3.24) and (3.29),

$$\boldsymbol{T}_w : \boldsymbol{W}^A = -\frac{1}{2}(1+\rho)\dot{\gamma}\,\|\boldsymbol{\Xi}_w\| < 0 \tag{3.30}$$

Since $\dot{\gamma}$ and $\|\boldsymbol{\Xi}\|$ are always positive, we have

$$\rho > -1 \tag{3.31}$$

Then we assume that the plastic spin has the same direction as the dissipative spin which physically means that the dissipative spin drives the plastic spin and consequently the spin of the unrotated configuration where the elastic rotation is removed. Hence, from Eq. (3.28), we have

$$\rho < 1 \tag{3.32}$$

Eqs. (3.31) and (3.32) imply that the total spin of the anisotropy axes does not exceed the dissipative spin in magnitude, see Eq. (3.27). Finally from Eqs. (3.24) and (3.27)

$$\boldsymbol{W}^{axes} = -\rho\dot{\gamma}\hat{\boldsymbol{\Xi}}_w \tag{3.33}$$

From this expression it is deduced that the anisotropy axes rotate in the direction of $\hat{\boldsymbol{\Xi}}_w$ if $\rho < 0$ while they rotate in the opposite direction of $\hat{\boldsymbol{\Xi}}_w$ if $\rho > 0$. It is reasonable to postulate that the anisotropy axes will rotate in the opposite direction of $\hat{\boldsymbol{\Xi}}_w$ because $\boldsymbol{\Xi}_w$ measures how much the elastic strain tensor and the stress tensor are not coaxial. This can be also confirmed by numerical tests versus laboratory test data. Consider the data in Fig. 1, which shows the prediction for the evolution of the principal orthotropic directions and the comparison with the experimental result when a uniaxial tensile force is applied on a metal sheet with three initial orientations of orthotropic axes. We observe a rotation of the orthotropic axes to a wrong orientation when we use $\rho < 0$.

Hence, together with Eqs. (3.31) and (3.32), a reasonable range of ρ is

$$0 < \rho < 1 \tag{3.34}$$

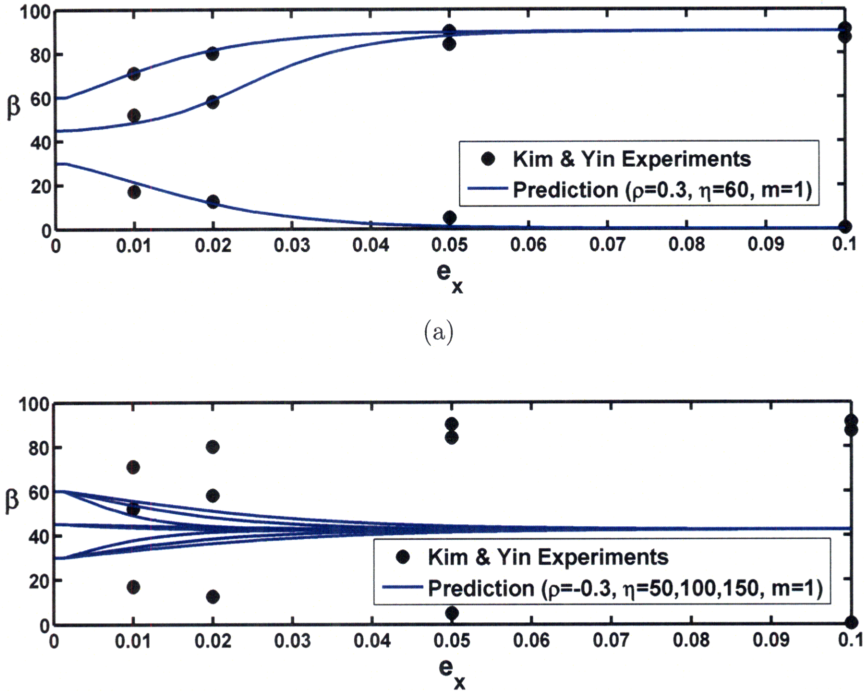

(a)

(b)

Figure 3-1: The evolution of the principal orthotropic directions at different spatial strains e_x when uniaxial tensile loading is applied to a metal sheet along the x-axis. β is the angle between the rolling direction and the loading direction (x-axis). Three initial orientations (30°, 45° and 60°) of orthotropic axis are considered. See Refs. [3,4] for the detailed description of the experiment and the analysis. The other material parameters are listed in Table 3.1.

3.2.2 The direction of axes rotation through elastic anisotropy

Boehler and Koss [84] and Kim and Yin [4] performed similar experiments to measure the evolution of orthotropic axes of a metal sheet under uniaxial tension with initial off-axis loading angles of 30°, 45° and 60°. Their results are qualitatively the same except for the case in which the initial off-axis loading angle is 45°. A counterclockwise rotation to 90° was observed by Kim and Yin while a clockwise rotation to 0° was reported by Boehler and Koss. Within our theory, these different observations can be explained by the elastic anisotropy because we claim that the anisotropy axes will rotate to more preferable directions such that the stored strain energy decreases. As shown in Fig. 3-2(a), our model can predict both experimentally observed clockwise and counterclockwise rotations by controlling the elastic anisotropy. Hence we

Table 3.1: The material parameters used in Sec. 3.2

Elastic constants	Hill's yield function parameters	Hardening
$E_a = 204GPa$		$M = 1.0$
$E_b = 203GPa$	$f = 0.3613$	$\kappa_0 = 230MPa$
$E_c = 210GPa$	$h = 0.4957$	$\kappa_\infty = 276MPa$
$\nu_{ab} = \nu_{ac} = \nu_{bc} = 0.3$	$g = 0.3535$	$\delta = 30$
$G_{ab} = 82GPa$	$l = 1.0$	$\bar{h} = 350MPa$
$G_{ac} = G_{bc} = 80.77GPa$		

conclude that the difference between the two different experimental observations may be due to the unconsidered or unknown elastic anisotropies. Here we changed the Young's moduli slightly to have a different landscape of Young's modulus in the plane and in consequence of the stored strain energy. Note that the orthotropic axes rotate in the direction of the downhill in Young's modulus variation, see Fig. 3-2(b). If we select an elastic tensor such that Young's modulus variation has a zero slope at 45 °, no rotation takes place for an initial orientation of 45 ° as shown in Fig. 3-3. Moreover the model predicts that the orthotropic axes rotate to 0 ° or 90 ° regardless of its initial orientation if Young's modulus has a monotonic increasing or decreasing pattern, see Figs. 3-4 and 3-5. Therefore the elastic anisotropy is very important in our model and enriches the model's predictability. This is a key feature of the model which distinguishes it from other phenomenological models that consider the plastic spin.

3.2.3 Sensitivity of the spin parameters

From Eqs. (3.22)-(3.28), the spin tensors can be rewritten as

$$\boldsymbol{W}^p = -\frac{1}{2\sqrt{2}}(1+\rho)\left(\frac{\langle f_w \rangle}{\eta}\right)^m \hat{\boldsymbol{\Xi}}_w \dot{\zeta} \tag{3.35}$$

$$\boldsymbol{W}^A = \frac{1}{2\sqrt{2}}(1-\rho)\left(\frac{\langle f_w \rangle}{\eta}\right)^m \hat{\boldsymbol{\Xi}}_w \dot{\zeta} \tag{3.36}$$

Fig. 3-6 shows the effect of the spin parameters, ρ, η and m, on the evolution of orthotropic axes in a uniaxial tension test. For the other material constants, we use

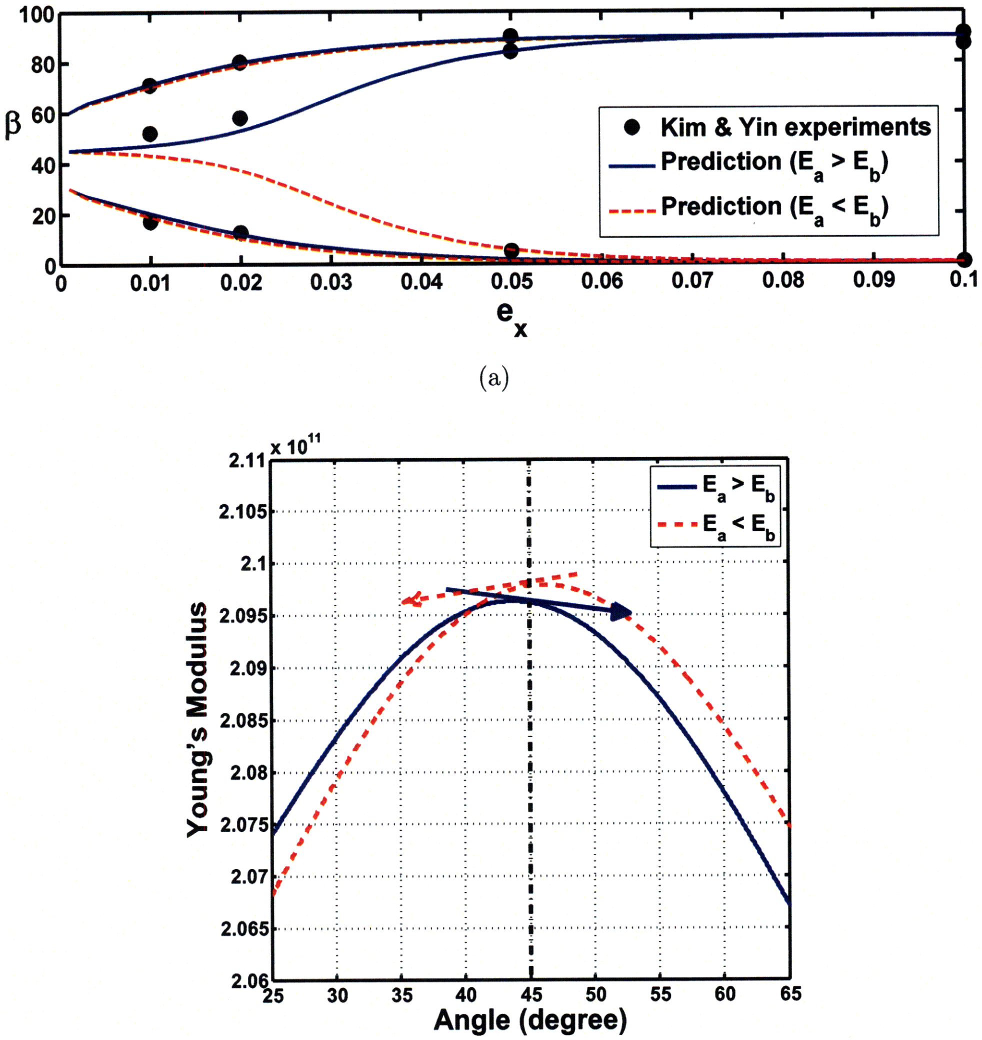

(a)

(b)

Figure 3-2: The effect of the elastic anisotropy. (a) The evolution of the principal orthotropic directions, (b) Young's modulus at different angles with respect to the rolling direction (a-direction). $E_a = 204GPa$ and $E_b = 203GPa$ are used for the solid lines while $E_a = 203GPa$ and $E_b = 204GPa$ are used for the dashed lines where a and b represent the rolling direction and the transverse direction of a metal sheet respectively. See Table 3.1 for the other elastic constants which are the same for both cases.

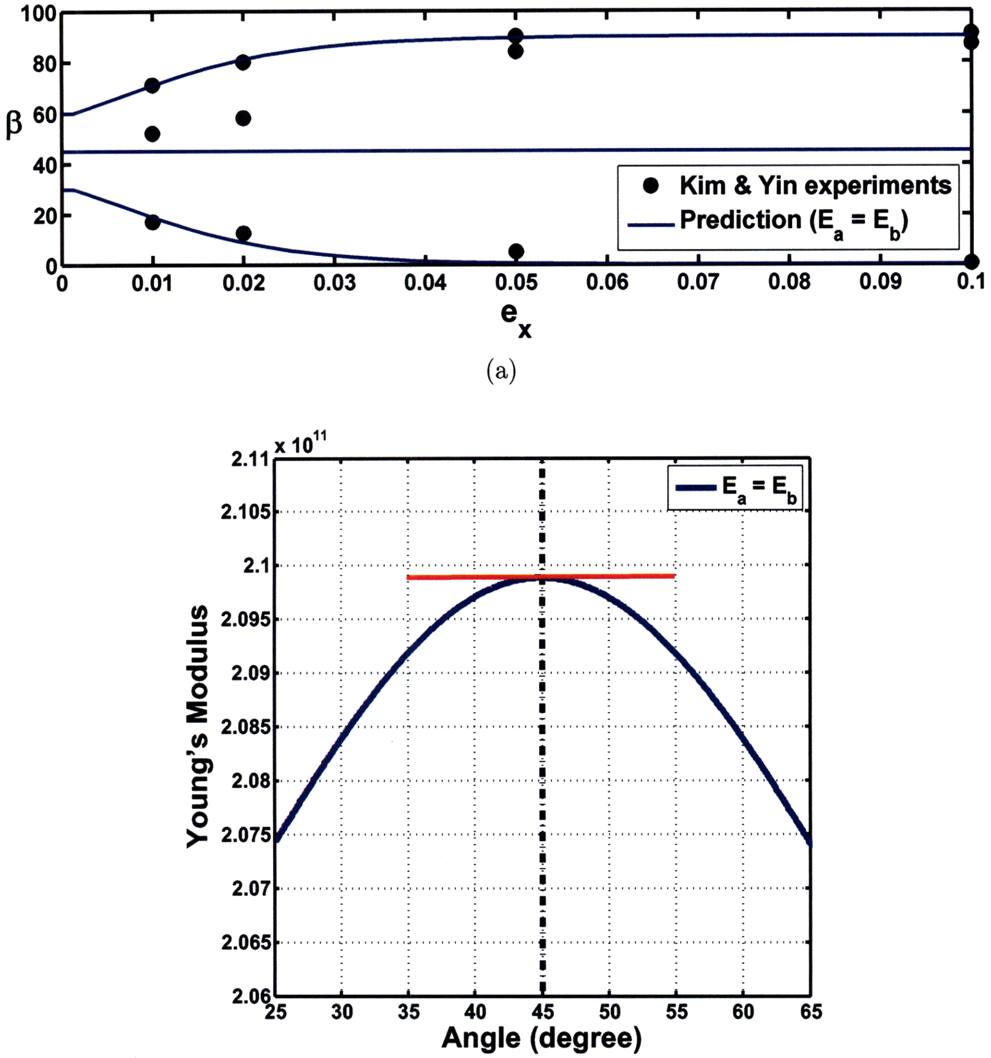

(a)

(b)

Figure 3-3: The effect of the elastic anisotropy. (a) The evolution of the principal orthotropic directions, (b) Young's modulus at different angles with respect to the rolling direction (a-direction). $E_a = E_b = 204GPa$.

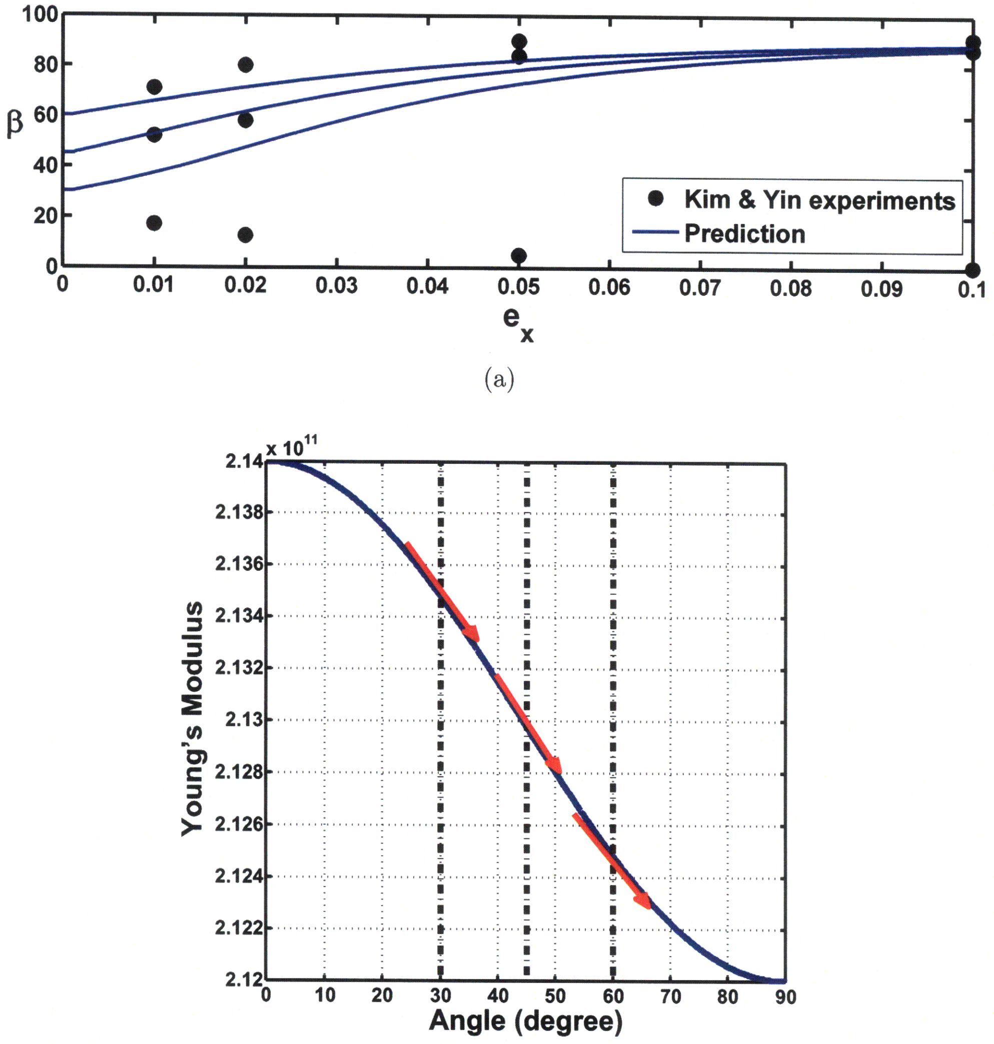

(a)

(b)

Figure 3-4: The effect of the elastic anisotropy. (a) The evolution of the principal orthotropic directions, (b) Young's modulus at different angles with respect to the rolling direction (a-direction). $E_a = 214GPa$ and $E_b = 212GPa$.

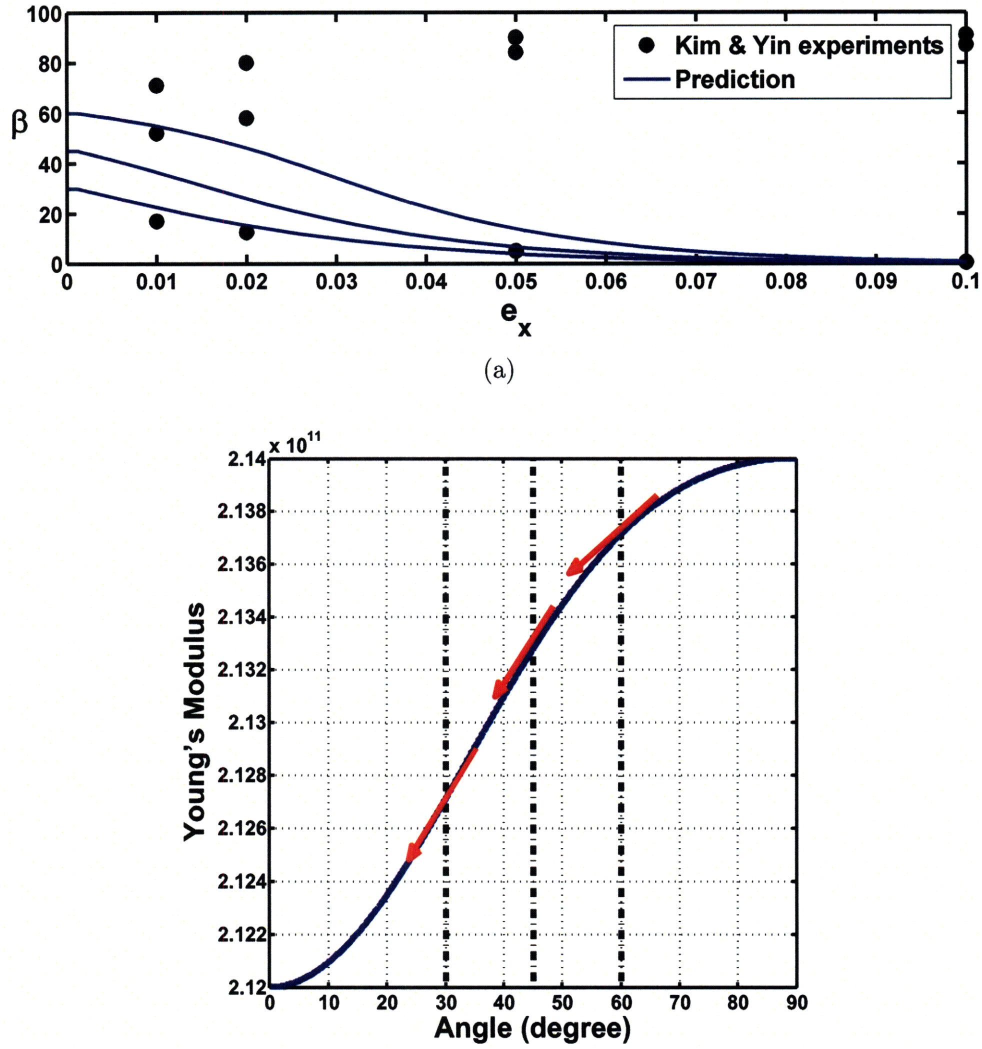

(a)

(b)

Figure 3-5: The effect of the elastic anisotropy. (a) The evolution of the principal orthotropic directions, (b) Young's modulus at different angles with respect to the rolling direction (a-direction). $E_a = 212GPa$ and $E_b = 214GPa$.

the same values as in Ref. [3] and they are listed in Table 3.1.

To be more quantitative in the analysis, we define the following root mean square errors for the orientation of the orthotropic axes

$$\Phi = \frac{1}{3}\left(\Theta_{\beta_0=30^\circ} + \Theta_{\beta_0=45^\circ} + \Theta_{\beta_0=60^\circ}\right) \tag{3.37}$$

where

$$\Theta_{\beta_0} = \sqrt{\frac{1}{n}\sum_{i=1}^{n}\left(\beta_i^{exp} - \beta_i^{num}\right)^2} \tag{3.38}$$

Here β_i^{exp} is the angle between the orthotropic axis (the rolling direction) and the loading direction obtained from experiments while β_i^{num} is the predicted angle by the model, β_0 is the initial orientation of the orthotropic axis and n is the number of experimental data points. Here the experimental data obtained by Kim and Yin [4] are used as a reference. The dimension for the angle is degree.

Fig. 3-7 shows the contour plot for Φ with respect to ρ and η when $m = 1$ and $m = 2$. We can see that there is a region where the change of Φ is negligible, which means that there is a certain relationship between ρ and η which gives a very similar prediction for the anisotropic axes rotation. These relationships obtained from the simulations for each m are also shown in Fig. 3-7 as dashed lines with their equations. The simulation results with some pairs of ρ and η on the dashed line for $m = 1$ are shown in Fig. 3-8. Note that almost the same predictions are obtained not only for the evolution of anisotropic axes but also for the evolution of the flow stresses.

This can be explained by considering the total spin of the anisotropic axes with respect to the unrotated configuration in Eq. (3.27). From Eqs. (3.27), (3.35) and (3.36), we have

$$\boldsymbol{W}^{axes} = -\frac{1}{\sqrt{2}}\left(\frac{\rho}{\eta^m}\right)\langle f_w\rangle^m \hat{\boldsymbol{\Xi}}_w\dot{\zeta} \tag{3.39}$$

This indicates that the ratio of ρ to η^m may play a more important role to the evolution of the anisotropic axes than the specific values of ρ, η and m. If we set the

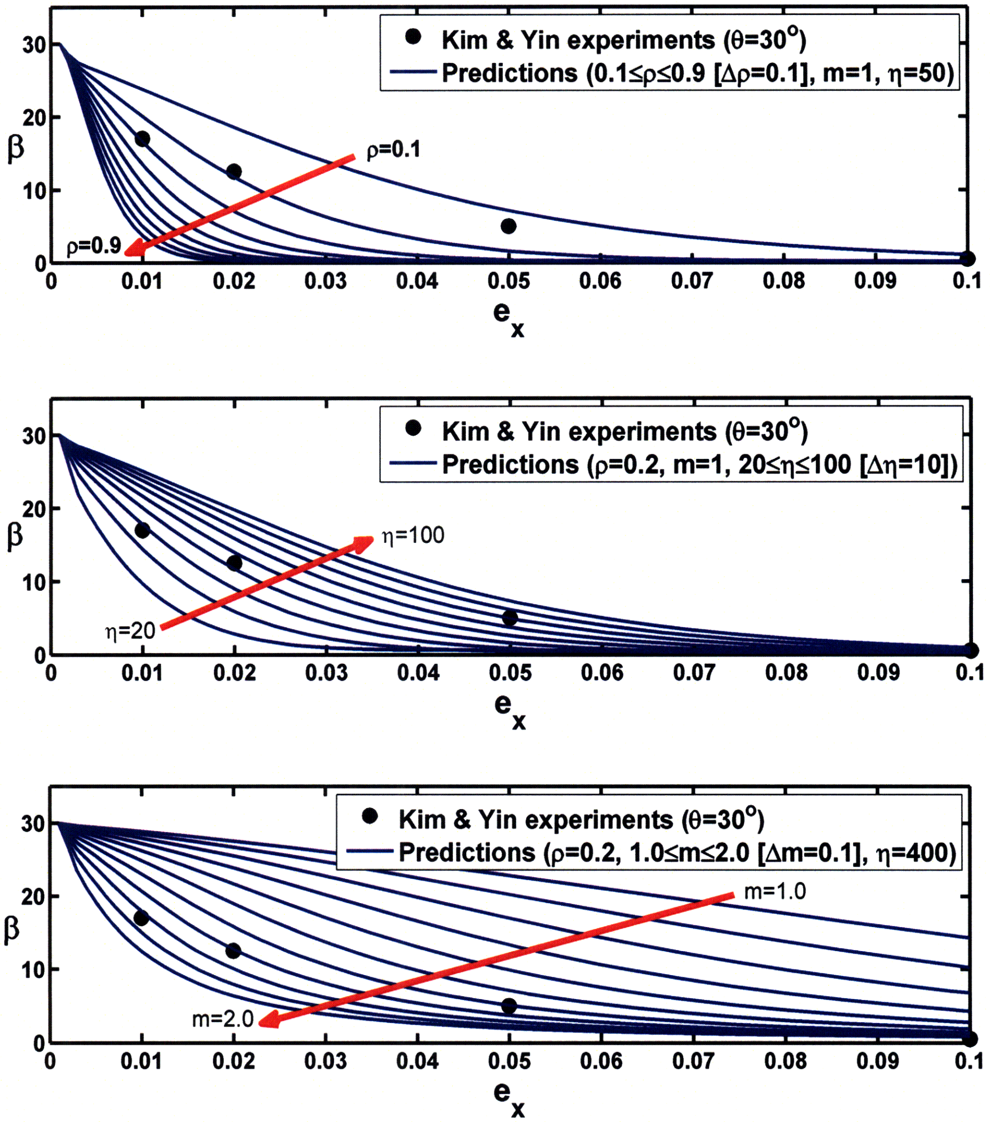

Figure 3-6: The effect of parameters on the evolution of the principal orthotropic directions. θ is the initial orientation of orthotropic axis

ratio to be a constant C, we have

$$\rho = C\eta^m \tag{3.40}$$

Eq. (3.40) provides a possible relationship between the spin parameters. We see that the dashed lines in Fig. 3-7 correspond to $C = 0.0051$ for $m = 1$ and $C = 1.1 \times 10^{-6}$ for $m = 2$ respectively.

However each value of parameters, not only the ratio of them, may be important for certain problems. As an example, we performed a simulation for a simple shear deformation with a load reversal and the result is shown in Fig. 3-9. The same material properties are used as in the previous uniaxial tensile test. Different responses are obtained even when we use pairs of the spin parameters which satisfy the relationship shown in Fig. 3-7(a). Especially there is a clear difference in the amount of the equivalent plastic strain where the load reversal begins, see Fig. 3-9(a). According to Figs. 3-9(b) and 3-9(c), the change is mainly attributed to the value of the parameter ρ while η has a primary effect on the initial transient response which depends on the rate of anisotropic axes rotation. Note that, in principle, ρ determines the amount of the axes spin from the given dissipative spin while η scales the skew part of the Mandel stress tensor. Therefore each parameter has a unique function and each value of parameters, not only their ratio, may be important for a certain problem like in simple shear where the principal strain direction changes continuously during the plastic deformation and, in consequence, the orthotropic axes and the intermediate configurations do so too.

3.3 Identification of spin parameters based on the R-values

In general, spin parameters have been chosen in order that a model properly reproduces the evolution curve of anisotropic axes measured from the evolution of anisotropies in yield stress as in Ref. [4]. As an alternative, Choi et al. [5] recently

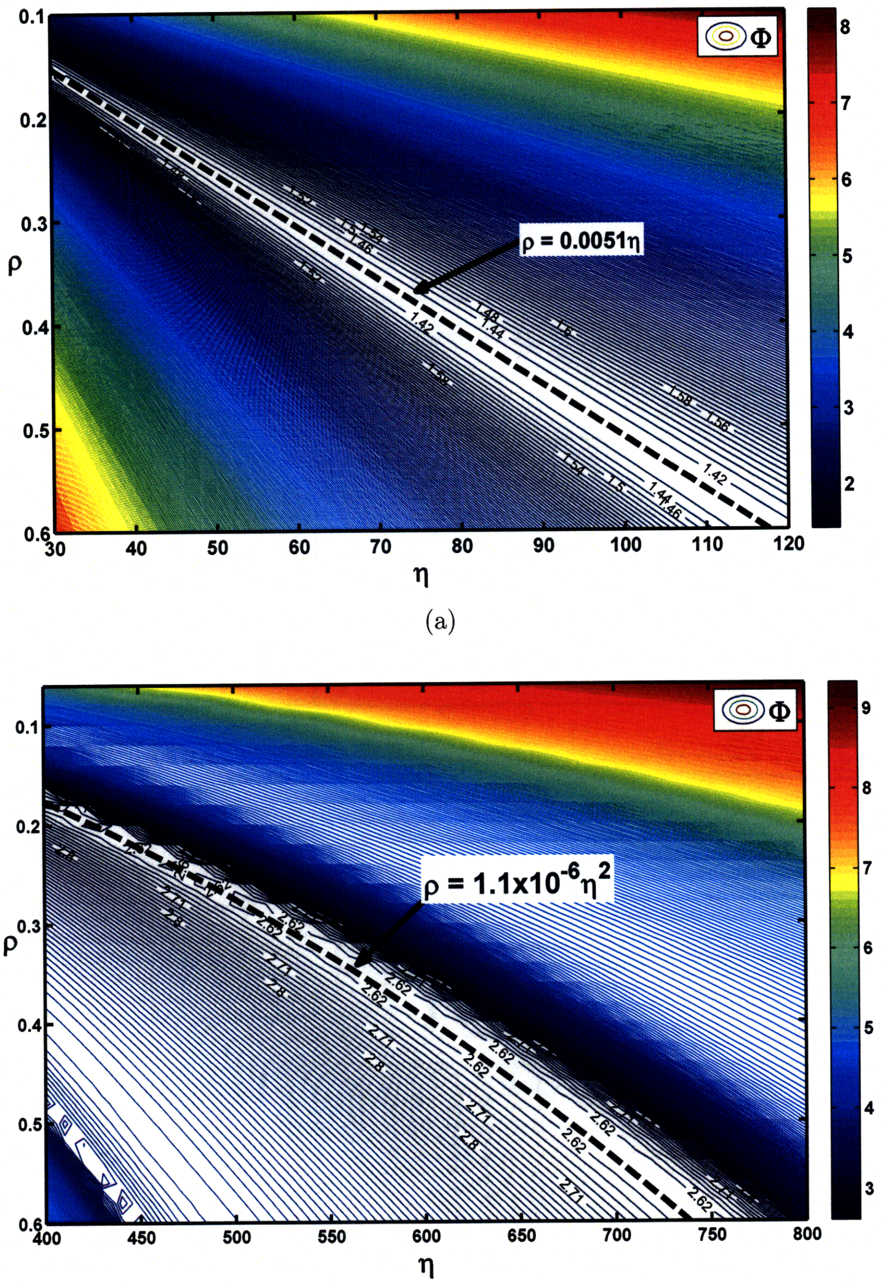

(a)

(b)

Figure 3-7: Contour maps for Φ with respect to ρ and η. (a) $m = 1$, (b) $m = 2$. The dashed lines represent where the change of Φ is minimum.

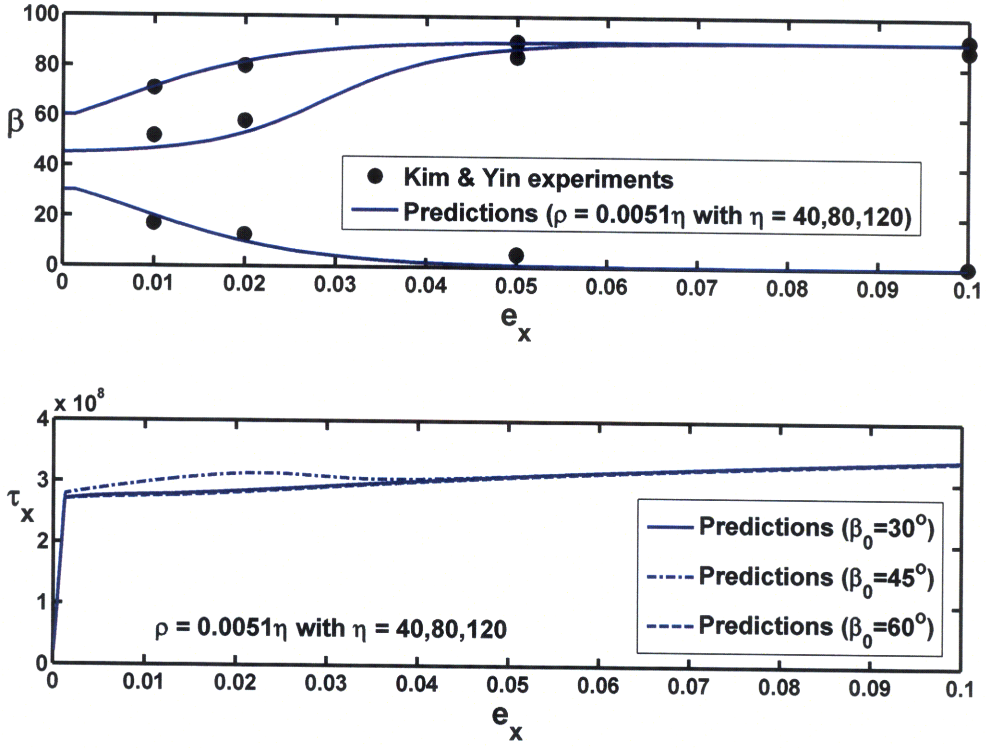

Figure 3-8: The evolution of the orthotropic axis and the flow stresses. Pairs of ρ and η on the dashed line in Fig. 3-7(a) are used with $m = 1$

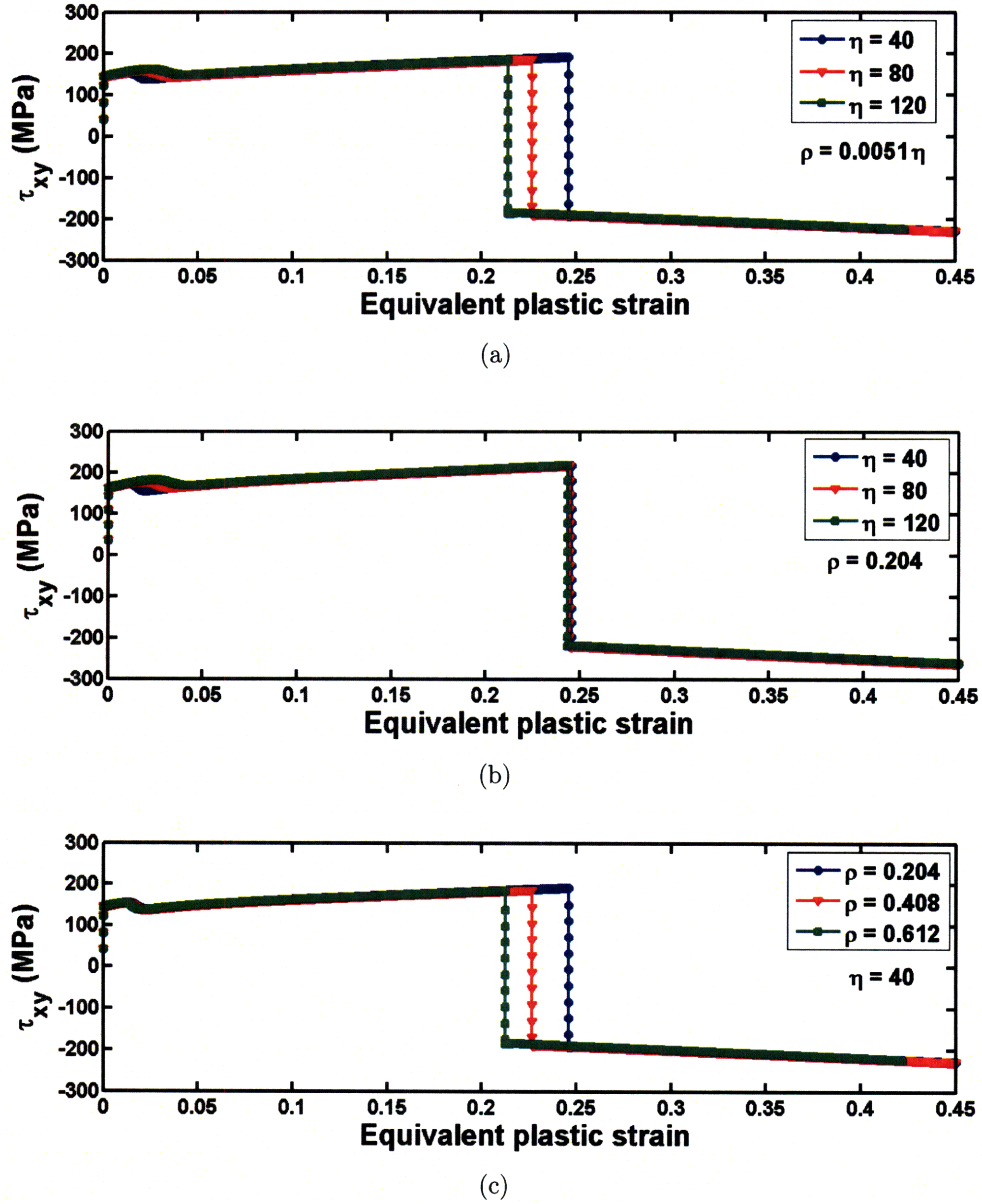

Figure 3-9: The evolution of shear stress in a reverse simple shear test ($m = 1$) (a) with pairs of ρ and η shown as the dashed line in Fig. 3-7(a); (b) with the fixed $\rho = 0.204$; (c) with the fixed $\eta = 40$.

proposed a possible way of identifying spin parameters based on the evolution of the R-values, also known as the Lankford coefficients. The motivation is based on the observation that the R-value shows a non-negligible evolution when an orthotropic axis is initially oriented at 45 ° while the R-values for the initial orientations of 0 ° and 90 ° can be regarded as constant as usual. Also, it has been shown that the flow stress for the initial orientation of 45 ° will be over-predicted if a conventional hardening model is used without considering the axes rotation [5]. Therefore the rotation of the orthotropic axes in addition to a conventional hardening model needs be included to predict the R-values and the flow stresses with better accuracy.

This procedure seems experimentally more practical than measuring the evolution of anisotropic axes directly because only uniaxial tensile test data for three different orientations of 0 °, 45 ° and 90 ° are necessary. The experimental data for 0 ° and 90 ° are used to determine isotropic hardening parameters and then we use the evolution curves of the R-value and the flow stress for 45 ° to calibrate parameters for kinematic hardening and plastic spin. The coefficients of Hill's quadratic yield function are calculated from the reference R-values. Here we apply this procedure to our model and compare our predictions with the experimental results available in Ref. [5].

First of all, we need to clarify the definition of the R-value because it has been used with various forms through the literature. We use the same definition of the R-value as in Ref. [5] given by

$$R = \frac{\varepsilon_w}{\varepsilon_t} = -\frac{\varepsilon_w}{\varepsilon_l + \varepsilon_w} \tag{3.41}$$

where ε_l is the longitudinal strain in the direction of uniaxial loading, ε_t is the through-the-thickness strain and ε_w is the widthwise strain. Due to the difficulty in measuring ε_t of sheet metals, $\varepsilon_t = -(\varepsilon_l + \varepsilon_w)$ is used by assuming small elastic strains and incompressibility of the plastic strains.

It has been reported that the flow stress for initial orientation of 45 ° will be under-predicted when only isotropic hardening is used even if the axes rotation is considered. We need to include kinematic hardening. Since it is not our goal to discuss which hardening model is more adequate, we simply use Prager's mixed hardening rule as in Eqs. (3.14) and (3.15) although Choi et al. [5] used a different hardening model. Of course, any kind of kinematic hardening model can be used with our model, simply by just replacing Eq. (3.15) with the chosen model equations. We use the orthotropic hardening tensor in Eq. (3.15), which in matrix form is

$$\underleftarrow{\mathbb{H}} = \begin{bmatrix} \frac{2}{3}h_a^E & -\frac{1}{3}\left(h_a^E + h_b^E - h_c^E\right) & -\frac{1}{3}\left(h_a^E - h_b^E + h_c^E\right) & 0 & 0 & 0 \\ -\frac{1}{3}\left(h_a^E + h_b^E - h_c^E\right) & \frac{2}{3}h_b^E & -\frac{1}{3}\left(-h_a^E + h_b^E + h_c^E\right) & 0 & 0 & 0 \\ -\frac{1}{3}\left(h_a^E - h_b^E + h_c^E\right) & -\frac{1}{3}\left(-h_a^E + h_b^E + h_c^E\right) & \frac{2}{3}h_c^E & 0 & 0 & 0 \\ 0 & 0 & 0 & 2h_{ab}^G & 0 & 0 \\ 0 & 0 & 0 & 0 & 2h_{ac}^G & 0 \\ 0 & 0 & 0 & 0 & 0 & 2h_{bc}^G \end{bmatrix} \tag{3.42}$$

where h_a^E, h_b^E and h_c^E are normal stress hardening parameters in each orthotropic direction and h_{ab}^G, h_{ac}^G and h_{bc}^G are shear stress hardening parameters in each plane. In case there is no preferred direction for kinematic hardening, this tensor may be replaced by the deviatoric projection tensor or by the identity tensor. Note that Eq. (3.42) guarantees the deviatoric feature of a backstress tensor. We assume that the orthotropic axes for hardening are aligned with those for the elastic tensor and the yield surface.

The same material properties are used as in Ref. [5]. The properties are those of two DDQ (deep drawing quality) and one DQ (drawing quality) mild steels. We calibrate spin parameters and kinematic hardening parameters of our model to fit the experimental results while we adopt the same values for isotropic hardening and initial R-values used in Ref. [5]. Only small anisotropy is introduced for elastic constants. The material properties and parameters used in this study are listed in Table 3.2. Figs. 3-10-3-12 show the results obtained. The predictions show a good agreement with experimental results both in the R-values and the flow stresses for all three materials, which is also achieved by Choi et al. Hence it may be concluded that this method can be an alternative way of identifying parameters for anisotropic axes

Table 3.2: The material parameters used in Sec. 3.3

Material	Elastic constants	R-values	Hardening	Spin
DDQ-1	$E_a = 212GPa$ $E_b = 208GPa$ $E_c = 210GPa$ $\nu_{ab} = \nu_{ac} = \nu_{bc} = 0.3$ $G_{ab} = 82GPa$ $G_{ac} = G_{bc} = 80.77GPa$	$R_0 = 2.722$ $R_{45} = 1.474$ $R_{90} = 2.169$	$M = 0.8$ $\kappa_0 = 152.00MPa$ $\kappa_\infty = 387.81MPa$ $\delta = 9.23$ $\bar{h} = 0.0$ $h_a^E = h_b^E = h_c^E = 1.0$ $h_{ab}^G = h_{ac}^G = h_{bc}^G = 1.6$	$\rho = 0.40$ $\eta = 60$ $m = 1.0$
DDQ-2	$E_a = 208GPa$ $E_b = 212GPa$ $E_c = 210GPa$ $\nu_{ab} = \nu_{ac} = \nu_{bc} = 0.3$ $G_{ab} = 82GPa$ $G_{ac} = G_{bc} = 80.77GPa$	$R_0 = 2.137$ $R_{45} = 0.930$ $R_{90} = 1.508$	$M = 0.8$ $\kappa_0 = 152.22MPa$ $\kappa_\infty = 372.23MPa$ $\delta = 7.87$ $\bar{h} = 0.0$ $h_a^E = h_b^E = h_c^E = 1.0$ $h_{ab}^G = h_{ac}^G = h_{bc}^G = 5.0$	$\rho = 0.26$ $\eta = 20$ $m = 1.0$
DQ	$E_a = 182GPa$ $E_b = 178GPa$ $E_c = 180GPa$ $\nu_{ab} = \nu_{ac} = \nu_{bc} = 0.3$ $G_{ab} = 70GPa$ $G_{ac} = G_{bc} = 69.23GPa$	$R_0 = 1.600$ $R_{45} = 1.010$ $R_{90} = 1.460$	$M = 0.8$ $\kappa_0 = 198.00MPa$ $\kappa_\infty = 455.00MPa$ $\delta = 9.95$ $\bar{h} = 0.0$ $h_a^E = h_b^E = h_c^E = 1.0$ $h_{ab}^G = h_{ac}^G = h_{bc}^G = 2.2$	$\rho = 0.48$ $\eta = 60$ $m = 1.0$

rotation.

However, much more comparisons of computed responses with experimental data on various materials are needed to validate this identification procedure. It would be ideal if we could compare the spin parameters, for the same material, calibrated from the evolution of anisotropies in yield stress as in Ref. [4] and from the evolution of the R-values and the flow stresses as in Ref. [5].

3.4 Predictability of the model in multi-paths loading problems

We consider in this section the capability of our model to predict the behavior in problems where the loading path changes during the plastic deformation. Two key

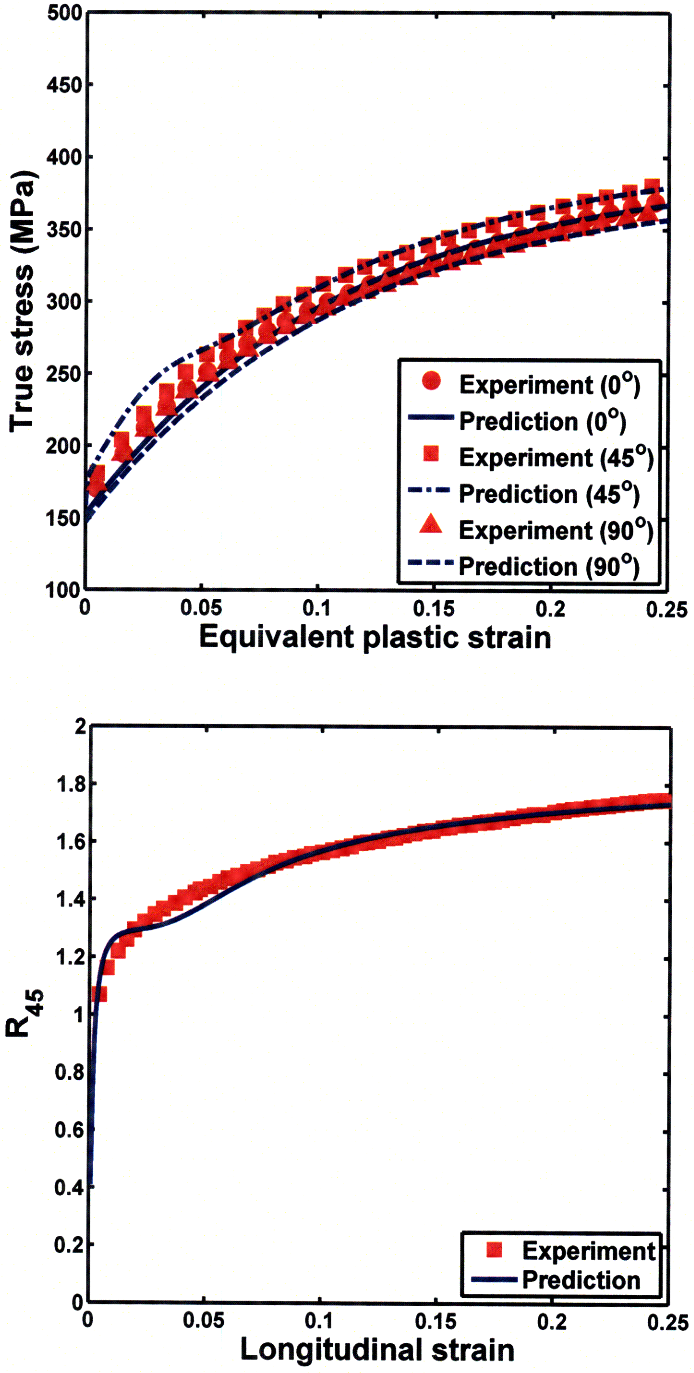

Figure 3-10: The evolution of flow stresses and R_{45} for DDQ-1 in Table 3.2. The experimental results are taken from Ref. [5]

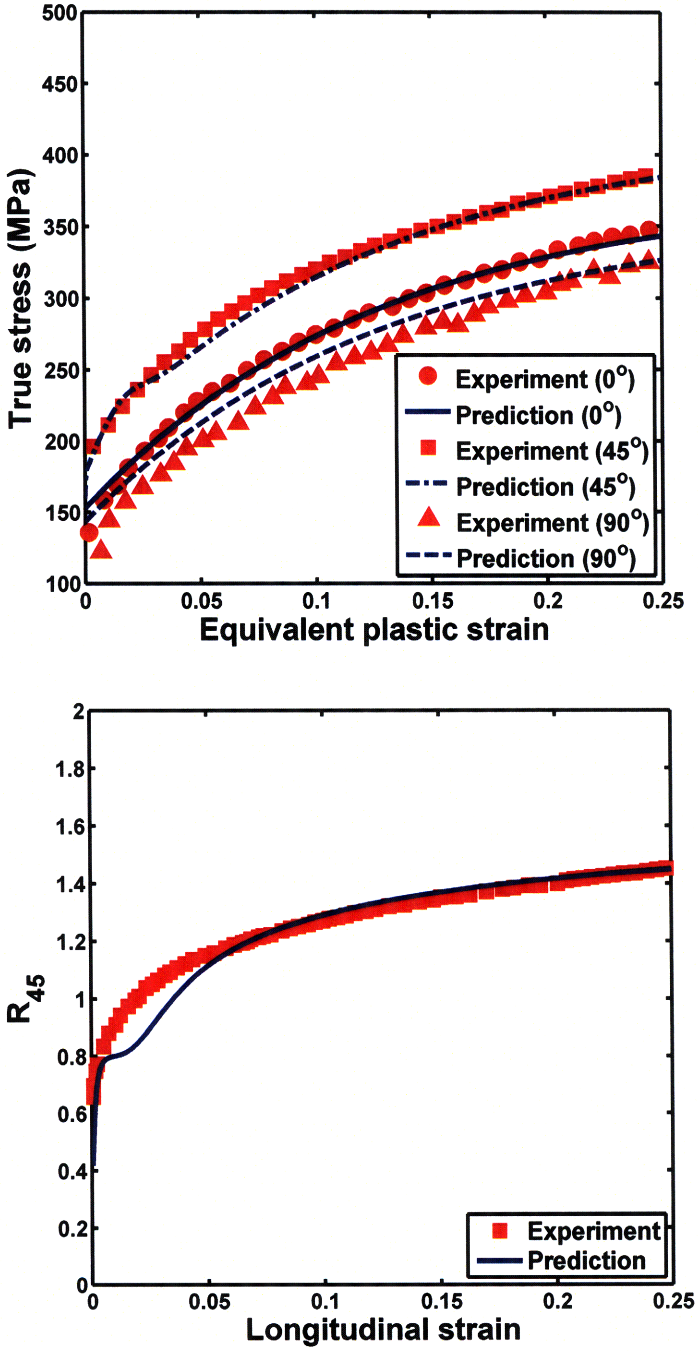

Figure 3-11: The evolution of flow stresses and R_{45} for DDQ-2 in Table 3.2. The experimental results are taken from Ref. [5]

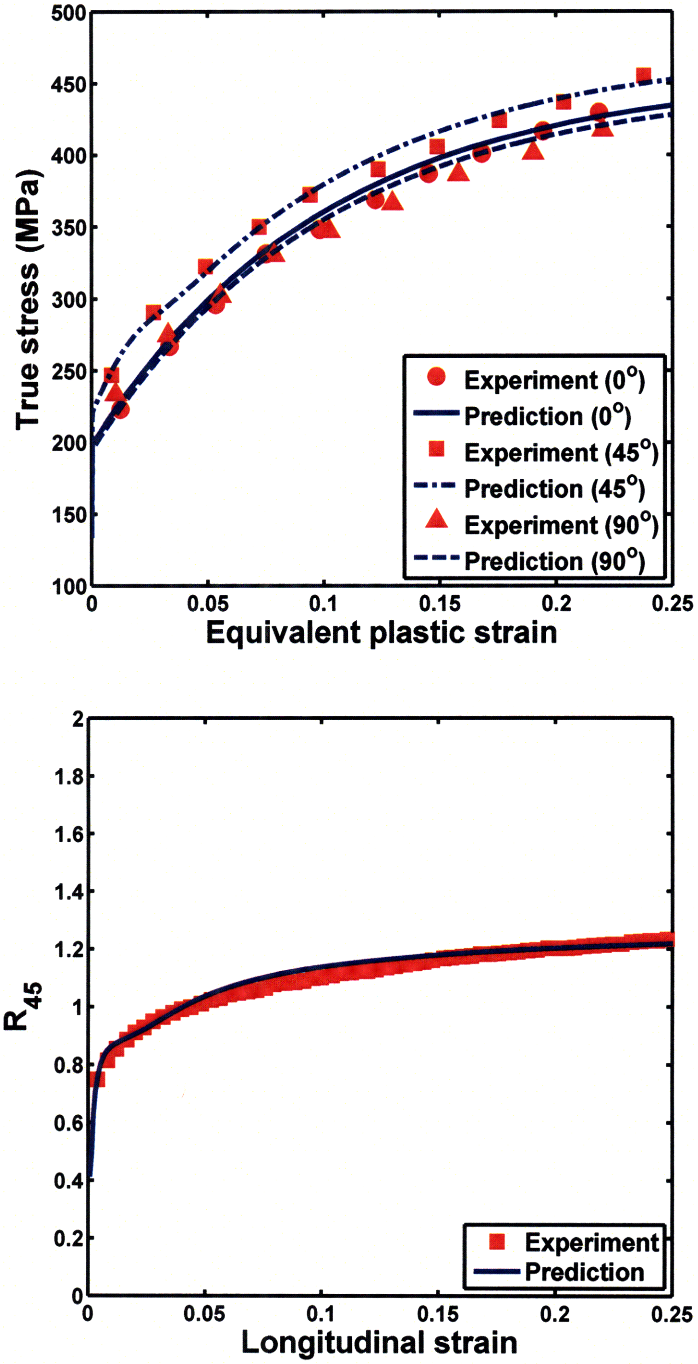

Figure 3-12: The evolution of flow stresses and R_{45} for DQ in Table 3.2. The experimental results are taken from Ref. [5]

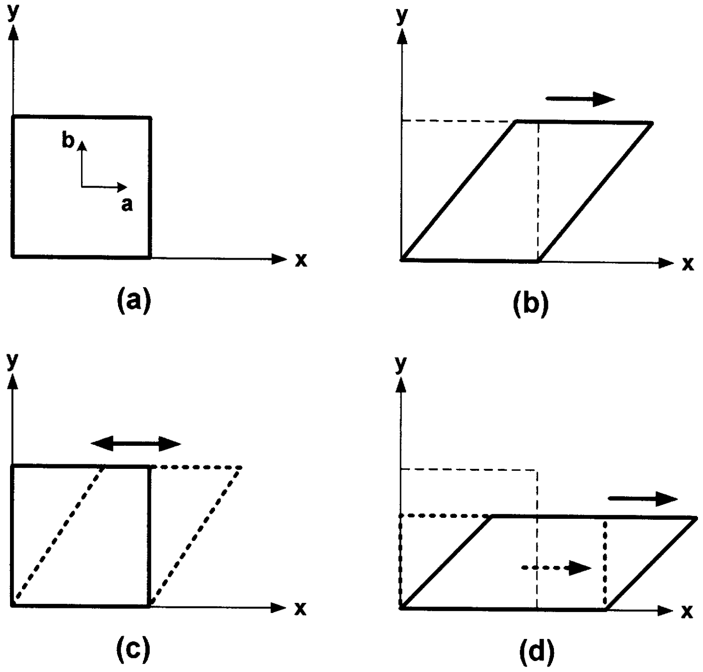

Figure 3-13: The multi-paths loading problems. (a) Initial configuration where a and b represent the rolling direction and the transverse direction of a metal sheet respectively; (b) The case of monotonic simple shear; (c) The case of reverse simple shear; (d) The case of tension-shear

features that we want to capture in multi-paths loading problems are the well-known 'Bauschinger' effect and the 'cross' effect, that is, the effect of uniaxial prestraining on the shear response [87, 95]. Three deformation patterns are simulated in order to identify basic features of a multi-paths loading problem as in Ref. [95]. The first one is a monotonic simple shear. The second one is a reverse simple shear, where the material goes back to its initial shape after a forward shear. The third one is a tension-shear path, where uniaxial prestraining is applied prior to the simple shear. The Bauschinger effect can be seen in the reverse shear test and the cross effect may appear in certain tension-shear tests depending on materials used. These are illustrated in Fig. 3-13

As reported in Ref. [95], the cross effect cannot be captured by a conventional phenomenological model which considers only isotropic and kinematic hardening while, of course, the Bauschinger effect can be modeled with kinematic hardening by the backstress evolution. If the rotation of anisotropic axes is taken into account, the

Table 3.3: The material parameters used in Sec. 3.4

Elastic constants	R-values	Hardening	Spin
$E_a = 207GPa$ $E_b = 206GPa$ $E_c = 206GPa$ $\nu_{ab} = \nu_{ac} = \nu_{bc} = 0.3$ $G_{ab} = 80GPa$ $G_{ac} = G_{bc} = 79.23GPa$	$R_0 = 2.64$ $R_{45} = 1.57$ $R_{90} = 2.17$	$\kappa_0 = 152.00MPa$ $\kappa_\infty = 387.81MPa$ $\delta = 9.23$ $\bar{h} = 0.0$	$\rho = 0.40$ $\eta = 80$ $m = 1.0$

cross effect appears in the predicted response. The calculated responses are shown in Figs. 3-14 and 3-15. The material parameters used are listed in Table 3.3. Note that the amount of crossing depends on how much the material is prestrained prior to the shear deformation. A larger amount of prestraining leads to a greater crossing effect as shown in Fig. 3-16. It is also interesting that the cross effect is greatly influenced by the amount of kinematic hardening, see Fig. 3-17. The cross effect becomes prominent as M approaches 1 (purely isotropic hardening). As the portion of kinematic hardening increases (M approaches 0), the cross effect gradually weakens and eventually no crossing takes place after a certain amount of hardening. In that case, the shear stress of a tension-shear test follows a monotonic simple shear curve with an offset.

3.5 Concluding Remarks

Despite the significant advances in the simulations of elasto-plastic responses, the efficient and accurate analysis of large strain deformations of anisotropic sheet metals remains elusive. This is due to the difficulties imposed by the elastic and plastic anisotropy and the evolution thereof.

In this chapter we performed some studies on a model suitable for the analysis of orthotropic elasto-plastic continua considering both the elastic and plastic anisotropy and the evolution of the material symmetries. Elastic anisotropy is a crucial ingredient in the model to capture the rotation of the anisotropy axes. These studies give some physical insight into the model, notably regarding the understanding of the

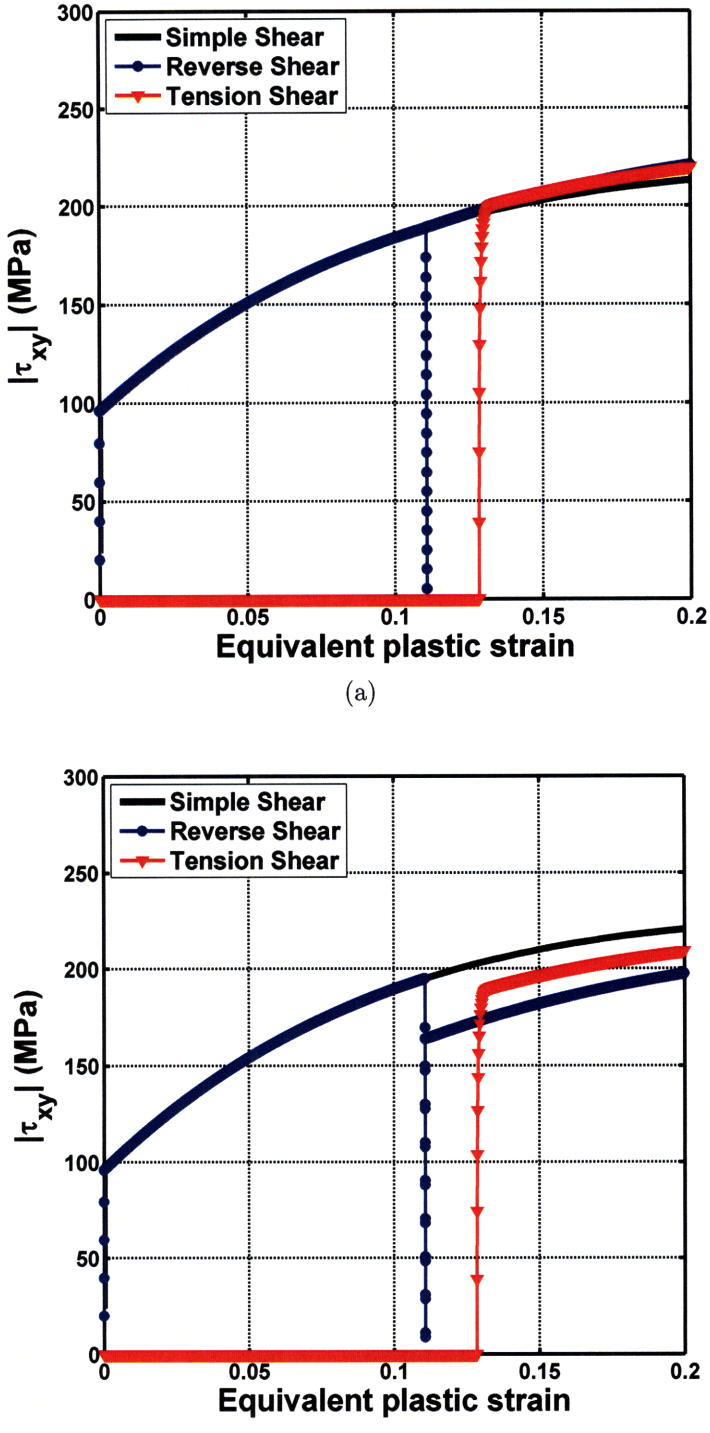

(a)

(b)

Figure 3-14: Multi-path loading response ***(without plastic spin)***; (a) isotropic hardening model - neither 'cross' nor 'Bauschinger' effect, (b) mixed hardening model - no 'cross' but 'Bauschinger' effect. ($M = 0.9$ and $\mathbb{H} = \mathbb{D}$ where $\mathbb{D}$ is the fourth order deviatoric projection tensor)

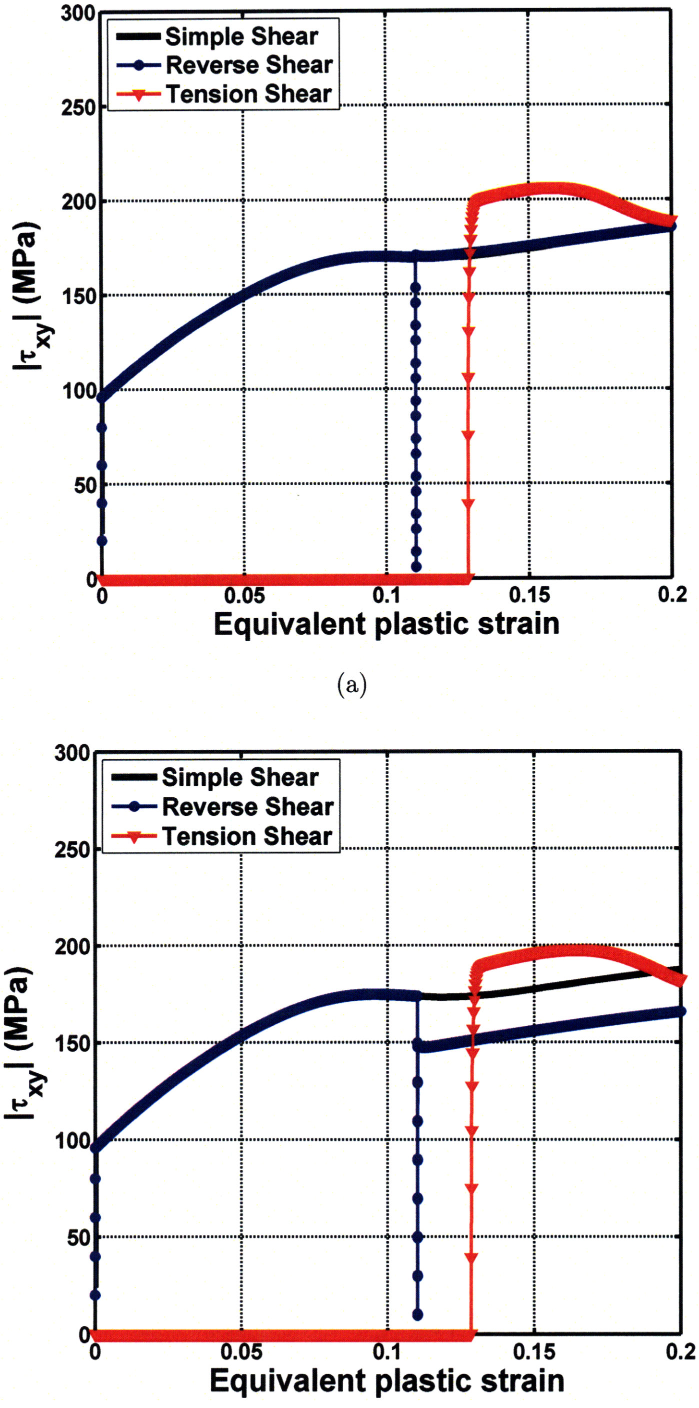

(a)

(b)

Figure 3-15: Multi-path loading response ***(with plastic spin)***; (a) isotropic hardening model – 'cross' but no 'Bauschinger' effect, (b) mixed hardening model – 'cross' and 'Bauschinger' effect. ($M = 0.9$ and $\mathbb{H} = \mathbb{D}$ where $\mathbb{D}$ is the fourth order deviatoric projection tensor)

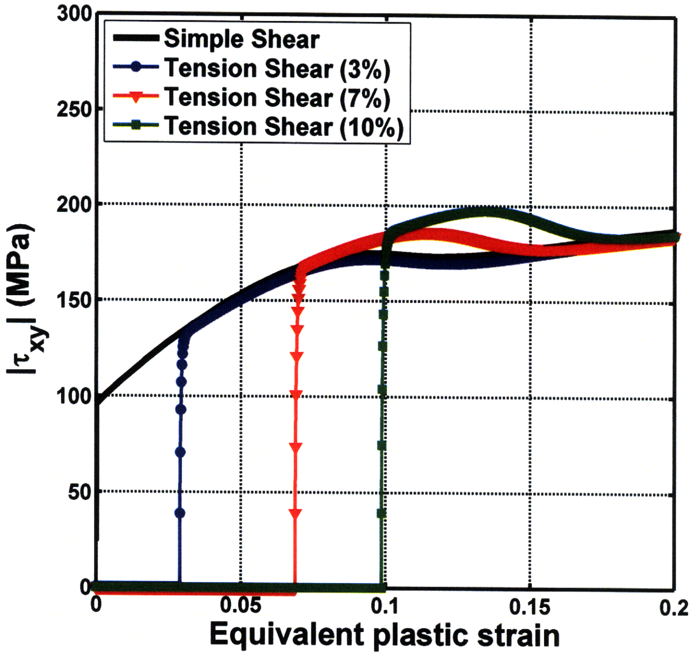

Figure 3-16: The effect of the amount of prestraining on crossing. (Isotropic hardening, $M = 1.0$)

material parameters that affect the evolution of the directions of orthotropy, their effect on the predictions achieved with the model, and hence the proper choice of these parameters. We obtain the material parameters from measurements of elastic and plastic anisotropies including from the evolution of the Lankford coefficients, and find that modeling the elastic anisotropy explains earlier published results.

An effective material model requires the use of a consistent theory, as given in this chapter, and a full validation of the model. For our model, a full validation will require the availability of more experimental data and comparisons with simulations. However, the required experimental data is still scarce, especially when including the measurement of elastic anisotropy. It will be very valuable to continue with the validation of the model as more experimental data becomes available.

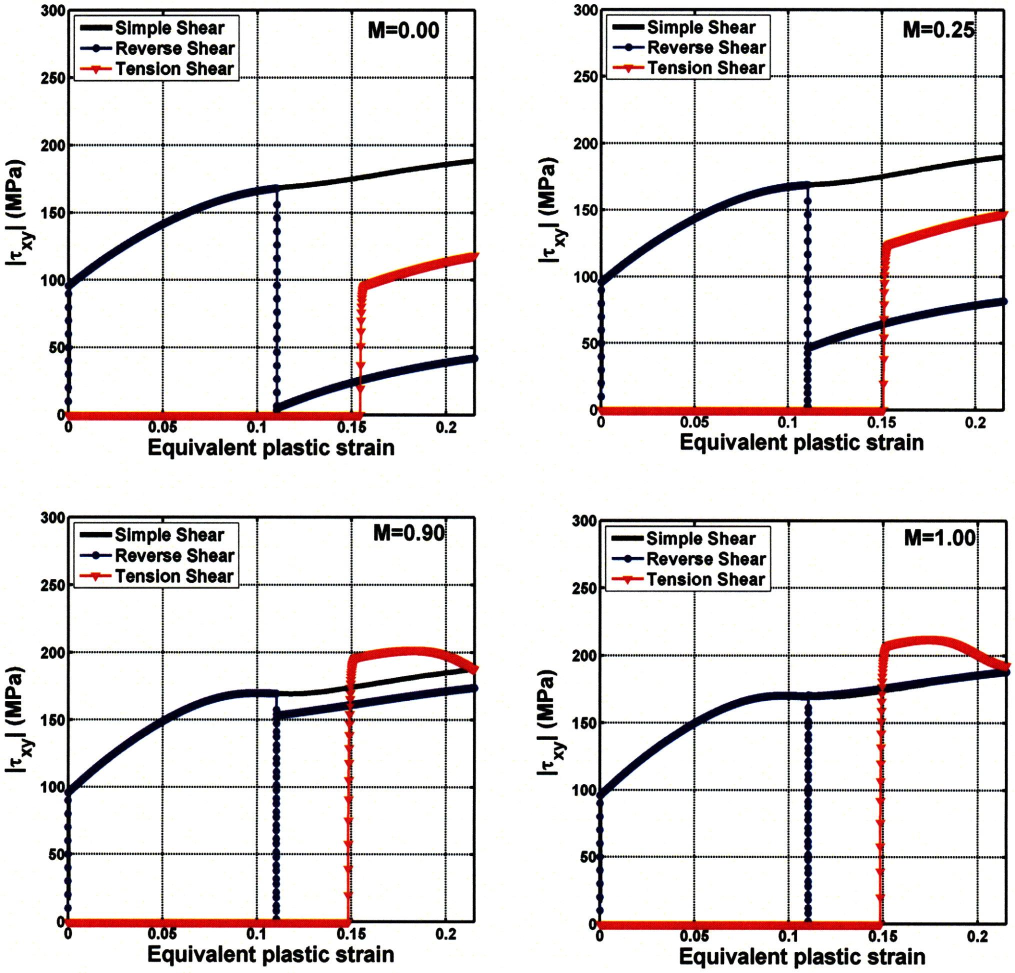

Figure 3-17: An effect of the mixed hardening parameter (M) on the cross effect. ($h_a^E = h_b^E = 1.2$, $h_c^E = 0.6$, $h_{ab}^G = h_{ac}^G = h_{bc}^G = 0.5$)

Conclusions

The present thesis work contributes to the anisotropic elasto-plastic analysis of shells by addressing key issues in obtaining reliable and efficient shell elements for the finite element analysis and a better constitutive model for large strain anisotropic elasto-plasticity.

First, we presented a 4-node 3D-shell element which is a 3D extension of the MITC4 shell element. The element is designed to model the three-dimensional effects of thickness changes and tractions applied on the top and bottom surfaces of the shell by adding appropriate displacement degrees of freedom in a hierarchical way. An important attribute is that the element does not result in undue ill-conditioning as seen when shell surface top and bottom nodes are used in the kinematic description of 3D-shell elements. The element, with additional pressure degrees of freedom, can be used when the material is incompressible. This feature is crucial in large strain elasto-plastic analysis because metallic materials usually become almost incompressible as plastic strains develop.

Second, we presented a 6-node triangular shell element which represents a significant improvement over the earlier published element, called the MITC6 shell element. The formulation of the improved element addresses the peculiar unstable behavior observed with the original MITC6 shell element in the solution of certain shell problems. The improved MITC6 shell element does not show this behavior and performs as well as the original element in the other test problems. In particular, the element formulation does not use any factor to be set by a user as seen in conventional stabilization procedures.

Finally, an anisotropic elasto-plasticity model that considers the rotation of anisotropy axes has been studied. The model provides a general framework for large strain anisotropic elasto-plasticity where the elastic anisotropy is used to model the rotation of the material axes. Our studies of the model have given physical insight into it, particularly regarding the material parameters used to describe the evolution of the anisotropy directions, their effect on the predictions obtained by the model, and the proper choice of the parameters. The studies also identified the predictability of the model for the evolution of the Lankford R-values and for the crossing effect in nonproportional loading conditions.

While some key points of research in the anisotropic elasto-plastic analysis of shells are addressed in this thesis, there are still a number of outstanding improvements - even in the developments addressed herein - that should be pursued in future work. For example, we still need more efficient shell elements, in particular triangular elements, that show uniformly optimal behavior in all problems, a property that is extremely difficult to reach. A mathematical analysis of the presented shell elements would also be very valuable and could yield insight into how the elements might be further improved. Regarding the elasto-plasticity model we considered in this work, we need to continue a full validation as more experimental data, including anisotropic elastic material parameters, become available. It would also be valuable to design an efficient experimental testing procedure to identify the material parameters used in the model.

These would be important developments in the specific topics addressed in this thesis. However, there are of course many more research areas of developments considering the general anisotropic elasto-plastic analysis of shells. These areas include the large strain analysis of shells, the analysis of composite shells, the modeling of contact conditions, and the analysis of shells in multi-physics conditions.

Appendix A

The analytic solution for the cantilever beam subjected to in-plane tractions

We consider the cantilever beam subjected to in-plane tractions described in Table 1.3, and use the Airy stress function method to solve for the stresses.

The stress equilibrium and strain compatibility conditions are satisfied by solving the equation

$$\frac{\partial^4 \phi}{\partial x^4} + 2\frac{\partial^4 \phi}{\partial x^2 \partial z^2} + \frac{\partial^4 \phi}{\partial z^4} = 0 \tag{A.1}$$

where

$$\tau_{xx} = \frac{\partial^2 \phi}{\partial z^2}, \quad \tau_{zz} = \frac{\partial^2 \phi}{\partial x^2}, \quad \tau_{xz} = -\frac{\partial^2 \phi}{\partial x \partial z}, \tag{A.2}$$

The boundary conditions are

$$\tau_{xz}\Big|_{z=\frac{t}{2}} = q_t \tag{A.3a}$$

$$\tau_{xz}\Big|_{z=-\frac{t}{2}} = -q_b \tag{A.3b}$$

$$\tau_{zz}\Big|_{z=\frac{t}{2}} = \tau_{zz}\Big|_{z=-\frac{t}{2}} = 0 \tag{A.3c}$$

where q_t and q_b are in-plane tractions applied on top and bottom surfaces in the positive x-direction, respectively. The trial stress function used is

$$\phi = c_0 \left(1 + a_1 x\right) \left(1 + b_1 z + b_2 z^2 + b_3 z^3\right) \tag{A.4}$$

which satisfies Eq. (A.1). Then the corresponding stresses are

$$\tau_{xx} = \frac{\partial^2 \phi}{\partial z^2} = c_0 \left(1 + a_1 x\right) \left(2b_2 + 6b_3 z\right) \tag{A.5a}$$

$$\tau_{zz} = \frac{\partial^2 \phi}{\partial x^2} = 0 \tag{A.5b}$$

$$\tau_{xz} = -\frac{\partial^2 \phi}{\partial x \partial z} = -c_0 a_1 \left(b_1 + 2b_2 z + 3b_3 z^2\right) \tag{A.5c}$$

From the force and moment equilibrium, the resultant shear force, axial force and bending moment at each section of the beam are

$$V(x) = \int_{-t/2}^{t/2} \tau_{xz} dz = 0 \tag{A.6a}$$

$$N(x) = \int_{-t/2}^{t/2} \tau_{xx} dz = \left(q_t + q_b\right)\left(L - x\right) \tag{A.6b}$$

$$M(x) = \int_{-t/2}^{t/2} \tau_{xx} z dz = \frac{t}{2}\left(q_t - q_b\right)\left(L - x\right) \tag{A.6c}$$

Substituting Eqs. (A.5) into Eqs. (A.6) and applying the boundary conditions given in Eqs. (A.3), we obtain

$$\begin{aligned} a_1 &= -\frac{1}{L} \\ c_0 b_1 &= -\frac{L}{4}\left(q_t - q_b\right) \\ c_0 b_2 &= \frac{L}{2t}\left(q_t + q_b\right) \\ c_0 b_3 &= \frac{L}{t^2}\left(q_t - q_b\right) \end{aligned} \tag{A.7}$$

Therefore the solution is

$$\tau_{xx} = (L - x)\left[(q_t + q_b)\frac{1}{t} + 6\,(q_t - q_b)\frac{z}{t^2}\right] \tag{A.8a}$$

$$\tau_{zz} = 0 \tag{A.8b}$$

$$\tau_{xz} = -\,(q_t - q_b)\frac{1}{4} + (q_t + q_b)\frac{z}{t} + 3\,(q_t - q_b)\frac{z^2}{t^2} \tag{A.8c}$$

Appendix B

Mapping tensors from quadratic to logarithmic strain space

We present here the mapping tensors used in the Montáns-Bathe model presented in Chapter 3. During the integration procedure, having the logarithmic strain, $\boldsymbol{E}^e = \frac{1}{2}\ln \boldsymbol{C}^e$, we obtain the generalized Kirchhoff stress tensor, $\boldsymbol{T} = \mathbb{A} : \boldsymbol{E}^e$, which is work conjugate to the logarithmic strain. Therefore, in general, we need to convert the obtained stress tensor to the Mandel stress tensor, $\boldsymbol{\Xi}$, because the dissipation inequality is given in terms of the Mandel stress tensors and we assume the yield functions to hold for them, see for example Eq. (3.17).

We define a mapping tensor

$$\boldsymbol{E}^e = \mathbb{M}_{\boldsymbol{A}}^{\boldsymbol{E}} : \boldsymbol{A}^e \tag{B.1}$$

where $\boldsymbol{E}^e$ and $\boldsymbol{A}^e$ are the logarithmic strain tensor and the quadratic strain tensor respectively and their spectral forms are

$$\boldsymbol{E}^e = \sum_{i=1}^{3} \ln \lambda_i^e \boldsymbol{N}_i \otimes \boldsymbol{N}_i \tag{B.2a}$$

$$\boldsymbol{A}^e = \sum_{i=1}^{3} \frac{1}{2}\left(\lambda_i^{e2} - 1\right) \boldsymbol{N}_i \otimes \boldsymbol{N}_i \tag{B.2b}$$

where λ_i^e are principal stretches and $\boldsymbol{N}_i$ are principal directions. The above mapping tensor in Eq. (B.1) can be written as

$$\mathbb{M}_{\boldsymbol{A}}^{\boldsymbol{E}} = \sum_{i=1}^{3} \frac{2 \ln \lambda_i^e}{\lambda_i^{e2} - 1} \boldsymbol{N}_i \otimes \boldsymbol{N}_i \otimes \boldsymbol{N}_i \otimes \boldsymbol{N}_i \tag{B.3}$$

Similarly we can obtain the mapping tensor between the deformation rate tensor, $\boldsymbol{D}^e$, and the time-derivative of the logarithmic strain, $\dot{\boldsymbol{E}}^e$.

$$\mathbb{M}_{\boldsymbol{D}}^{\dot{\boldsymbol{E}}} = \frac{\partial \boldsymbol{E}^e}{\partial \boldsymbol{A}^e} = \sum_{i=1}^{3} \frac{1}{\lambda_i^{e2}} \boldsymbol{M}_i \otimes \boldsymbol{M}_i + \sum_{i=1}^{3} \sum_{j \neq i} 2 \frac{\ln \lambda_j^e - \ln \lambda_i^e}{\lambda_j^{e2} - \lambda_i^{e2}} \boldsymbol{M}_i \overset{s}{\odot} \boldsymbol{M}_j \tag{B.4}$$

where

$$\boldsymbol{M}_i := \boldsymbol{N}_i \otimes \boldsymbol{N}_i \tag{B.5a}$$

$$\boldsymbol{M}_i \overset{s}{\odot} \boldsymbol{M}_j := \frac{1}{4} \left(\boldsymbol{N}_i \otimes \boldsymbol{N}_j + \boldsymbol{N}_j \otimes \boldsymbol{N}_i \right) \otimes \left(\boldsymbol{N}_i \otimes \boldsymbol{N}_j + \boldsymbol{N}_j \otimes \boldsymbol{N}_i \right) \equiv \boldsymbol{M}_j \overset{s}{\odot} \boldsymbol{M}_i \tag{B.5b}$$

such that

$$\dot{\boldsymbol{E}}^e = \mathbb{M}_{\boldsymbol{D}}^{\dot{\boldsymbol{E}}} : \boldsymbol{D}^e \tag{B.6}$$

In the rotation-frozen configuration Eq. (B.6) can be written as

$$\underleftarrow{\dot{\boldsymbol{E}}}^e = \underleftarrow{\mathbb{M}}_{\boldsymbol{D}}^{\dot{\boldsymbol{E}}} : \underleftarrow{\boldsymbol{D}}^e \tag{B.7}$$

Now we define two fourth order mapping tensors

$$\underleftarrow{\mathbb{W}}^M := \frac{1}{2} \left(\underleftarrow{\boldsymbol{C}}^e \overset{3}{\cdot} \underleftarrow{\mathbb{M}}_{\boldsymbol{D}}^{\dot{\boldsymbol{E}}} - \underleftarrow{\boldsymbol{C}}^e \overset{4}{\cdot} \underleftarrow{\mathbb{M}}_{\boldsymbol{D}}^{\dot{\boldsymbol{E}}} \right) \tag{B.8}$$

and

$$\underleftarrow{\mathbb{S}}^M := \frac{1}{2} \left(\underleftarrow{\boldsymbol{C}}^e \overset{3}{\cdot} \underleftarrow{\mathbb{M}}_{\boldsymbol{D}}^{\dot{\boldsymbol{E}}} + \underleftarrow{\boldsymbol{C}}^e \overset{4}{\cdot} \underleftarrow{\mathbb{M}}_{\boldsymbol{D}}^{\dot{\boldsymbol{E}}} \right) \tag{B.9}$$

where it is implied by $\left(\overset{n}{\cdot}\right)$ that the contraction of the *n-index* of the fourth order tensor with the second index of the second order tensor such that

$$\begin{aligned}
\underleftarrow{\boldsymbol{C}}^{e} \overset{3}{\cdot} \underleftarrow{\mathbb{M}^{\dot{\boldsymbol{E}}}_{\boldsymbol{D}}} &= \sum_{i,j,\ldots,d}^{3} \left(\underleftarrow{\boldsymbol{C}}^{e}_{ij} \boldsymbol{N}_i \otimes \boldsymbol{N}_j\right) \overset{3}{\cdot} \left(\underleftarrow{\mathbb{M}^{\dot{\boldsymbol{E}}}_{\boldsymbol{D}}}_{abcd} \boldsymbol{N}_a \otimes \boldsymbol{N}_b \otimes \boldsymbol{N}_c \otimes \boldsymbol{N}_d\right) \\
&= \sum_{i,j,\ldots,d}^{3} \underleftarrow{\boldsymbol{C}}^{e}_{ij} \underleftarrow{\mathbb{M}^{\dot{\boldsymbol{E}}}_{\boldsymbol{D}}}_{abcd} \delta_{jc} \boldsymbol{N}_a \otimes \boldsymbol{N}_b \otimes \boldsymbol{N}_i \otimes \boldsymbol{N}_d \qquad \text{(B.10)} \\
&= \sum_{i,j,\ldots,c}^{3} \underleftarrow{\boldsymbol{C}}^{e}_{ij} \underleftarrow{\mathbb{M}^{\dot{\boldsymbol{E}}}_{\boldsymbol{D}}}_{abjc} \boldsymbol{N}_a \otimes \boldsymbol{N}_b \otimes \boldsymbol{N}_i \otimes \boldsymbol{N}_c
\end{aligned}$$

and

$$\begin{aligned}
\underleftarrow{\boldsymbol{C}}^{e} \overset{4}{\cdot} \underleftarrow{\mathbb{M}^{\dot{\boldsymbol{E}}}_{\boldsymbol{D}}} &= \sum_{i,j,\ldots,d}^{3} \left(\underleftarrow{\boldsymbol{C}}^{e}_{ij} \boldsymbol{N}_i \otimes \boldsymbol{N}_j\right) \overset{4}{\cdot} \left(\underleftarrow{\mathbb{M}^{\dot{\boldsymbol{E}}}_{\boldsymbol{D}}}_{abcd} \boldsymbol{N}_a \otimes \boldsymbol{N}_b \otimes \boldsymbol{N}_c \otimes \boldsymbol{N}_d\right) \\
&= \sum_{i,j,\ldots,d}^{3} \underleftarrow{\boldsymbol{C}}^{e}_{ij} \underleftarrow{\mathbb{M}^{\dot{\boldsymbol{E}}}_{\boldsymbol{D}}}_{abcd} \delta_{jd} \boldsymbol{N}_a \otimes \boldsymbol{N}_b \otimes \boldsymbol{N}_c \otimes \boldsymbol{N}_i \qquad \text{(B.11)} \\
&= \sum_{i,j,\ldots,c}^{3} \underleftarrow{\boldsymbol{C}}^{e}_{ij} \underleftarrow{\mathbb{M}^{\dot{\boldsymbol{E}}}_{\boldsymbol{D}}}_{abcj} \boldsymbol{N}_a \otimes \boldsymbol{N}_b \otimes \boldsymbol{N}_c \otimes \boldsymbol{N}_i
\end{aligned}$$

Then it can be shown that

$$\underleftarrow{\boldsymbol{S}} := \underleftarrow{\boldsymbol{T}} : \underleftarrow{\mathbb{M}^{\dot{\boldsymbol{E}}}_{\boldsymbol{D}}} \qquad \text{(B.12)}$$

where $\boldsymbol{S}$ is the pull-back of the Kirchhoff stress $\boldsymbol{\tau}$ to the stress-free configuration. Therefore we obtain

$$\underleftarrow{\boldsymbol{\Xi}} := \underleftarrow{\boldsymbol{C}}^{e} \underleftarrow{\boldsymbol{S}} = \underleftarrow{\boldsymbol{C}}^{e} \left(\underleftarrow{\boldsymbol{T}} : \underleftarrow{\mathbb{M}^{\dot{\boldsymbol{E}}}_{\boldsymbol{D}}}\right) = \underleftarrow{\boldsymbol{T}} : \left(\underleftarrow{\mathbb{S}}^{M} + \underleftarrow{\mathbb{W}}^{M}\right) \qquad \text{(B.13)}$$

and

$$\underleftarrow{\boldsymbol{T}}_{w} := \underleftarrow{\boldsymbol{T}} : \underleftarrow{\mathbb{W}}^{M} = \underleftarrow{\boldsymbol{E}}^{e} \underleftarrow{\boldsymbol{T}} - \underleftarrow{\boldsymbol{T}} \underleftarrow{\boldsymbol{E}}^{e} \equiv \underleftarrow{\boldsymbol{\Xi}}_{w} \qquad \text{(B.14a)}$$

$$\underleftarrow{\boldsymbol{\Xi}}_{s} = \underleftarrow{\boldsymbol{T}} : \underleftarrow{\mathbb{S}}^{M} \qquad \text{(B.14b)}$$

Appendix C

A stress integration algorithm

We present a simple stress integration algorithm that can be used to solve a set of equations, given in Eqs. 3.19 and 3.26, of the Montáns-Bathe model in Chapter 3. Note that the model consists of two parts, the symmetric part and the skew symmetric part, and one can adopt the specific computational algorithm which can be either staggered/split or fully coupled.

Here we assume that elastic strains are moderate and split the symmetric part and the skew part in the integration procedure, which yield a simple algorithm. First the iterations are performed for the symmetric part to obtain the consistency parameter, t or ζ, assuming the symmetric axes do not change during this step. Then the consistency parameter of the skew part, γ or ξ, is simply obtained by the proposed relationship in Eq. (3.26). All necessary variables including the principal directions of anisotropic axes are updated from the flow rules with the computed consistency parameters. The consequences of the assumptions used are as follows.

- For moderate elastic strains,
    - $\mathbb{S}^M \simeq \mathbb{I}$
    - $\|\boldsymbol{T}_w\| \ll \|\boldsymbol{T}\|$
    - $\boldsymbol{\Xi}_s = \boldsymbol{T} : \mathbb{S}^M \simeq \boldsymbol{T} : \mathbb{I} = \boldsymbol{T}$
    - $\boldsymbol{\Xi} = \boldsymbol{\Xi}_s + \boldsymbol{\Xi}_w = \boldsymbol{T} : \mathbb{S}^M + \boldsymbol{T}_w \simeq \boldsymbol{T} + \boldsymbol{T}_w \simeq \boldsymbol{T}$

- During the stress integration phase, we assume that the principal directions of the anisotropic tensors are fixed, i.e. ${}^{t+\Delta t}\underleftarrow{\mathbb{A}} \simeq {}^{t}\mathbb{A}$. After reaching convergence on the consistency parameter of the symmetric part, t or ζ, the skew part can be easily calculated and then the principal directions are updated for the next step.

For convenience, we rewrite the given functions and the flow rules.

$$f_s = \frac{3}{2\kappa^2}\left(\underleftarrow{\boldsymbol{\Xi}}_s - \underleftarrow{\boldsymbol{B}}_s\right) : \underleftarrow{\mathbb{A}}^p_s : \left(\underleftarrow{\boldsymbol{\Xi}}_s - \underleftarrow{\boldsymbol{B}}_s\right) - 1 \tag{C.1}$$

$$f_w = \left\|\underleftarrow{\boldsymbol{\Xi}}_w\right\| - \sqrt{2}\kappa_w \tag{C.2}$$

$$\underleftarrow{\boldsymbol{D}}^p = \dot{t}\frac{\partial f_s}{\partial \underleftarrow{\boldsymbol{\Xi}}_s} = \frac{3}{\kappa^2}\underleftarrow{\mathbb{A}}^p_s : \left(\underleftarrow{\boldsymbol{\Xi}}_s - \underleftarrow{\boldsymbol{B}}_s\right)\dot{t} \tag{C.3}$$

$$\underleftarrow{\boldsymbol{W}}^d = \dot{\gamma}\frac{\partial f_w}{\partial \underleftarrow{\boldsymbol{\Xi}}_w} = \dot{\gamma}\frac{\underleftarrow{\boldsymbol{\Xi}}_w}{\left\|\underleftarrow{\boldsymbol{\Xi}}_w\right\|} \tag{C.4}$$

$$\dot{\zeta} = -\dot{t}\frac{\partial f_s}{\partial \kappa} = \frac{2}{\kappa}\left(f_s + 1\right)\dot{t} = \frac{2}{\kappa}\dot{t} \quad \text{(using at yield, } f_s = 0\text{)} \tag{C.5}$$

$$\dot{\xi} = -\dot{\gamma}\frac{\partial f_w}{\partial \kappa_w} = \sqrt{2}\dot{\gamma} \tag{C.6}$$

$$\dot{\xi} = \left(\frac{\langle f_w \rangle}{\eta}\right)^m \dot{\zeta} \quad \text{or} \quad \dot{\gamma} = \frac{\sqrt{2}}{\kappa}\left(\frac{\langle f_w \rangle}{\eta}\right)^m \dot{t} \tag{C.7}$$

$$\kappa = (1 - M)\kappa_0 + M\left[\kappa_\infty - (\kappa_\infty - \kappa_0)\exp\left(-\delta\zeta\right) + \bar{h}\zeta\right] \tag{C.8}$$

$$\dot{\underleftarrow{\boldsymbol{B}}}_s = \frac{2}{3}(1 - M)\left[(\kappa_\infty - \kappa_0)\,\delta\exp\left(-\delta\zeta\right) + \bar{h}\right]\underleftarrow{\mathbb{H}} : \underleftarrow{\boldsymbol{D}}^p \tag{C.9}$$

In the integration algorithm, we need to have the following quantities to be provided and returned at each step.

- Given: ${}^{t+\Delta t}_{0}\boldsymbol{X}, \left({}^{t}_{0}\boldsymbol{X}^p\right)^{-1}, {}^{t}\zeta, {}^{t}\underleftarrow{\boldsymbol{B}}_s, {}^{t}\boldsymbol{p}_i$

- Returned: $\left({}^{t+\Delta t}_{0}\boldsymbol{X}^p\right)^{-1}, {}^{t+\Delta t}\zeta, {}^{t+\Delta t}\underleftarrow{\boldsymbol{B}}_s, {}^{t+\Delta t}\boldsymbol{p}_i, {}^{t+\Delta t}\boldsymbol{\tau}$

where $\boldsymbol{p}_i$ represent the principal directions.

A single step consists of the following iteration procedure.

1. Compute trial state variables

    (a) Compute ${}^t\mathbb{A}$, ${}^t\mathbb{A}^p_s$ and ${}^t\mathbb{H}$ from ${}^t\boldsymbol{p}_i$.

    (b) Compute trial stress tensors

$$\boldsymbol{X}^e_* = {}^{t+\Delta t}_{\ \ 0}\boldsymbol{X}\left({}^t_0\boldsymbol{X}^p\right)^{-1} \tag{C.10}$$

$$\underleftarrow{\boldsymbol{C}}^e_* = \boldsymbol{X}^{eT}_*\boldsymbol{X}^e_* \tag{C.11}$$

$$\underleftarrow{\boldsymbol{E}}^e_* = \frac{1}{2}\log\underleftarrow{\boldsymbol{C}}^e_* \tag{C.12}$$

$$\boldsymbol{R}^e_* = \boldsymbol{X}^e_*\left(\underleftarrow{\boldsymbol{U}}^e_*\right)^{-1} \quad \text{from the polar decomposition} \tag{C.13}$$

$$\underleftarrow{\boldsymbol{\Xi}}_{s*} \simeq \underleftarrow{\boldsymbol{T}}_* = {}^{t+\Delta t}\underleftarrow{\mathbb{A}} : \underleftarrow{\boldsymbol{E}}^e_* = {}^t\mathbb{A} : \underleftarrow{\boldsymbol{E}}^e_* \tag{C.14}$$

$$\underleftarrow{\boldsymbol{B}}_{s*} = {}^t\underleftarrow{\boldsymbol{B}}_s \tag{C.15}$$

$${}^t\kappa = (1-M)\kappa_0 + M\left[\kappa_\infty - (\kappa_\infty - \kappa_0)\exp\left(-\delta\,{}^t\zeta\right) + \bar{h}\,{}^t\zeta\right] \tag{C.16}$$

2. Check yield condition.

$$\begin{aligned} f_{s*} &= \frac{3}{2\,{}^t\kappa^2}\left(\underleftarrow{\boldsymbol{\Xi}}_{s*} - \underleftarrow{\boldsymbol{B}}_{s*}\right) : {}^{t+\Delta t}\underleftarrow{\mathbb{A}}^p_s : \left(\underleftarrow{\boldsymbol{\Xi}}_{s*} - \underleftarrow{\boldsymbol{B}}_{s*}\right) - 1 \\ &= \frac{3}{2\,{}^t\kappa^2}\left(\underleftarrow{\boldsymbol{\Xi}}_{s*} - \underleftarrow{\boldsymbol{B}}_{s*}\right) : {}^t\mathbb{A}^p_s : \left(\underleftarrow{\boldsymbol{\Xi}}_{s*} - \underleftarrow{\boldsymbol{B}}_{s*}\right) - 1 \end{aligned} \tag{C.17}$$

3. If $f_{s*} < 0$ (the elastic region), update variables and go to the next time(integration) step.

$$\left({}^{t+\Delta t}_{\ \ 0}\boldsymbol{X}^p\right)^{-1} = \left({}^t_0\boldsymbol{X}^p\right)^{-1} \tag{C.18}$$

$${}^{t+\Delta t}\zeta = {}^t\zeta \tag{C.19}$$

$${}^{t+\Delta t}\underleftarrow{\boldsymbol{B}}_s = {}^t\underleftarrow{\boldsymbol{B}}_s \tag{C.20}$$

$${}^{t+\Delta t}\boldsymbol{p}_i = {}^t\boldsymbol{p}_i \tag{C.21}$$

$${}^{t+\Delta t}\boldsymbol{\tau} = \boldsymbol{R}^e_*\underleftarrow{\boldsymbol{T}}_*\boldsymbol{R}^{eT}_* \tag{C.22}$$

4. Otherwise, perform the plastic correction (the return mapping) loop for the symmetric part.

   (a) Assume Δt and find $\Delta\zeta^{(i)}$ and ${}^{t+\Delta t}\kappa^{(i)}$ that satisfy Eqs. (C.5) and (C.8). Compute

   $$R\left(\zeta^{(i)}\right) = \kappa\left(\zeta^{(i)}\right)\Delta\zeta^{(i)} - 2\Delta t \tag{C.23}$$

   where $\zeta^{(i)} = {}^{t}\zeta + \Delta\zeta^{(i)}$.

   If $\left|R\left(\zeta^{(i)}\right)\right| \leq \textit{tolerance}$, go to the next step of the plastic correction loop. Otherwise calculate a new $\Delta\zeta^{(i+1)}$ using Newton's method

   $$\Delta\zeta^{(i+1)} = \Delta\zeta^{(i)} - \frac{R\left(\zeta^{(i)}\right)}{\left(dR\left(\zeta^{(i)}\right)/d\zeta^{(i)}\right)} \tag{C.24}$$

   where $\frac{dR\left(\zeta^{(i)}\right)}{d\zeta^{(i)}} = \frac{d\kappa\left(\zeta^{(i)}\right)}{d\zeta^{(i)}}\Delta\zeta^{(i)} + \kappa\left(\zeta^{(i)}\right)$ and do iterations.

   (b) Compute ${}^{t+\Delta t}\underleftarrow{\boldsymbol{D}}^{p}$.

   From Eq. (C.3),

   $$\begin{aligned} {}^{t+\Delta t}\underleftarrow{\boldsymbol{D}}^{p} &= \frac{3}{{}^{t+\Delta t}\kappa^{2}}\,{}^{t+\Delta t}\underleftarrow{\mathbb{A}}^{p}_{s} : \left({}^{t+\Delta t}\underleftarrow{\boldsymbol{\Xi}}_{s} - {}^{t+\Delta t}\underleftarrow{\boldsymbol{B}}_{s}\right) \\ &= \frac{3}{{}^{t+\Delta t}\kappa^{2}}\,{}^{t}\mathbb{A}^{p}_{s} : \left({}^{t+\Delta t}\underleftarrow{\boldsymbol{\Xi}}_{s} - {}^{t+\Delta t}\underleftarrow{\boldsymbol{B}}_{s}\right) \end{aligned} \tag{C.25}$$

   From Eq. (3.9) and substituting Eq. (C.25),

   $$\begin{aligned} {}^{t+\Delta t}\underleftarrow{\boldsymbol{\Xi}}_{s} &= \underleftarrow{\boldsymbol{\Xi}}_{s*} - \Delta t\,{}^{t+\Delta t}\underleftarrow{\mathbb{A}} : {}^{t+\Delta t}\underleftarrow{\boldsymbol{D}}^{p} \\ &= \underleftarrow{\boldsymbol{\Xi}}_{s*} - \frac{3\Delta t}{{}^{t+\Delta t}\kappa^{2}}\,{}^{t+\Delta t}\underleftarrow{\mathbb{A}} : {}^{t+\Delta t}\underleftarrow{\mathbb{A}}^{p}_{s} : \left({}^{t+\Delta t}\underleftarrow{\boldsymbol{\Xi}}_{s} - {}^{t+\Delta t}\underleftarrow{\boldsymbol{B}}_{s}\right) \\ &= \underleftarrow{\boldsymbol{\Xi}}_{s*} - \frac{3\Delta t}{{}^{t+\Delta t}\kappa^{2}}\,{}^{t}\mathbb{A} : {}^{t}\mathbb{A}^{p}_{s} : \left({}^{t+\Delta t}\underleftarrow{\boldsymbol{\Xi}}_{s} - {}^{t+\Delta t}\underleftarrow{\boldsymbol{B}}_{s}\right) \end{aligned} \tag{C.26}$$

From Eq. (C.9) and substituting Eq. (C.25),

$$\begin{aligned}
{}^{t+\Delta t}\underleftarrow{\boldsymbol{B}}_s &= {}^{t}\underleftarrow{\boldsymbol{B}}_s + \Delta t\, {}^{t+\Delta t}H\, {}^{t+\Delta t}\underleftarrow{\mathbb{H}} : {}^{t+\Delta t}\underleftarrow{\boldsymbol{D}}^p \\
&= {}^{t}\underleftarrow{\boldsymbol{B}}_s + \frac{3\Delta t}{{}^{t+\Delta t}\kappa^2}\, {}^{t+\Delta t}H\, {}^{t+\Delta t}\underleftarrow{\mathbb{H}} : {}^{t+\Delta t}\underleftarrow{\mathbb{A}}^p_s : \left({}^{t+\Delta t}\underleftarrow{\boldsymbol{\Xi}}_s - {}^{t+\Delta t}\underleftarrow{\boldsymbol{B}}_s\right) \\
&= {}^{t}\underleftarrow{\boldsymbol{B}}_s + \frac{3\Delta t}{{}^{t+\Delta t}\kappa^2}\, {}^{t+\Delta t}H\, {}^{t}\mathbb{H} : {}^{t}\mathbb{A}^p_s : \left({}^{t+\Delta t}\underleftarrow{\boldsymbol{\Xi}}_s - {}^{t+\Delta t}\underleftarrow{\boldsymbol{B}}_s\right)
\end{aligned} \tag{C.27}$$

where ${}^{t+\Delta t}H = \frac{2}{3}(1 - M)\left[(\kappa_\infty - \kappa_0)\,\delta \exp\left(-\delta\, {}^{t+\Delta t}\zeta\right) + \bar{h}\right]$.

Subtracting Eq. (C.27) from Eq. (C.26) and rearranging it leads to

$$\begin{aligned}
&{}^{t+\Delta t}\underleftarrow{\boldsymbol{\Xi}}_s - {}^{t+\Delta t}\underleftarrow{\boldsymbol{B}}_s = \\
&\qquad \left\{\mathbb{I} + \frac{3\Delta t}{{}^{t+\Delta t}\kappa^2}\left({}^{t}\mathbb{A} + {}^{t+\Delta t}H\, {}^{t}\mathbb{H}\right) : {}^{t}\mathbb{A}^p_s\right\}^{-1} : \left(\underleftarrow{\boldsymbol{\Xi}}_{s*} - {}^{t}\underleftarrow{\boldsymbol{B}}_s\right)
\end{aligned} \tag{C.28}$$

Then, by substituting Eq. (C.28) into Eq. (C.25), we finally have

$$\begin{aligned}
&{}^{t+\Delta t}\underleftarrow{\boldsymbol{D}}^p = \\
&\quad \frac{3}{{}^{t+\Delta t}\kappa^2}\, {}^{t}\mathbb{A}^p_s : \left\{\mathbb{I} + \frac{3\Delta t}{{}^{t+\Delta t}\kappa^2}\left({}^{t}\mathbb{A} + {}^{t+\Delta t}H\, {}^{t}\mathbb{H}\right) : {}^{t}\mathbb{A}^p_s\right\}^{-1} : \left(\underleftarrow{\boldsymbol{\Xi}}_{s*} - {}^{t}\underleftarrow{\boldsymbol{B}}_s\right)
\end{aligned} \tag{C.29}$$

Note that all components in Eq. (C.29) are known values from the previous steps.

(c) Compute the yield function.

$${}^{t+\Delta t}f_s = \frac{3}{2\, {}^{t+\Delta t}\kappa^2}\left({}^{t+\Delta t}\underleftarrow{\boldsymbol{\Xi}}_s - {}^{t+\Delta t}\underleftarrow{\boldsymbol{B}}_s\right) : {}^{t}\mathbb{A}^p_s : \left({}^{t+\Delta t}\underleftarrow{\boldsymbol{\Xi}}_s - {}^{t+\Delta t}\underleftarrow{\boldsymbol{B}}_s\right) - 1 \tag{C.30}$$

where ${}^{t+\Delta t}\underleftarrow{\boldsymbol{\Xi}}_s - {}^{t+\Delta t}\underleftarrow{\boldsymbol{B}}_s$ can be obtained from Eq. (C.28).

(d) If $\left|{}^{t+\Delta t}f_s\right| \leq$ *tolerance*, stop iteration and go to the next step.

(e) Otherwise, compute a new Δt guess and do iterate. If we use Newton's method, a new Δt guess is

$$\Delta t^{new} = \Delta t^{old} - \frac{{}^{t+\Delta t}f_s}{{}^{t+\Delta t}\dot{f}_s} \tag{C.31}$$

where, from Eq. (C.30),

$$\begin{aligned} {}^{t+\Delta t}\dot{f}_s = {} & \frac{3}{{}^{t+\Delta t}\kappa^2}\left({}^{t+\Delta t}\underleftarrow{\boldsymbol{\Xi}}_s - {}^{t+\Delta t}\underleftarrow{\boldsymbol{B}}_s\right) : {}^t\mathbb{A}^p_s : \left({}^{t+\Delta t}\underleftarrow{\dot{\boldsymbol{\Xi}}}_s - {}^{t+\Delta t}\underleftarrow{\dot{\boldsymbol{B}}}_s\right) \\ & - \frac{2}{{}^{t+\Delta t}\kappa}\,{}^{t+\Delta t}\dot{\kappa}\left({}^{t+\Delta t}f_s + 1\right) \end{aligned} \tag{C.32}$$

with ${}^{t+\Delta t}\underleftarrow{\dot{\boldsymbol{\Xi}}}_s - {}^{t+\Delta t}\underleftarrow{\dot{\boldsymbol{B}}}_s$ being calculated.
From Eqs. (C.26) and (C.27),

$$\begin{aligned} {}^{t+\Delta t}\underleftarrow{\dot{\boldsymbol{\Xi}}}_s &= \frac{d}{dt}\left({}^{t+\Delta t}\underleftarrow{\mathbb{A}} : {}^{t+\Delta t}_{\;0}\underleftarrow{\boldsymbol{E}}^e\right) = {}^t\mathbb{A} : \frac{d}{dt}\left({}^{t+\Delta t}_{\;0}\underleftarrow{\boldsymbol{E}}^e\right) \\ &= {}^t\mathbb{A} : \frac{d}{dt}\left(\underleftarrow{\boldsymbol{E}}^e_* - \Delta t\,{}^{t+\Delta t}\underleftarrow{\boldsymbol{D}}^p\right) = -{}^t\mathbb{A} : \left({}^{t+\Delta t}\underleftarrow{\boldsymbol{D}}^p + \Delta t\,{}^{t+\Delta t}\underleftarrow{\dot{\boldsymbol{D}}}^p\right) \end{aligned} \tag{C.33}$$

$$\begin{aligned} {}^{t+\Delta t}\underleftarrow{\dot{\boldsymbol{B}}}_s &= \frac{d}{dt}\left({}^t\underleftarrow{\boldsymbol{B}}_s + \Delta t\,{}^{t+\Delta t}H\,{}^{t+\Delta t}\underleftarrow{\mathbb{H}} : {}^{t+\Delta t}\underleftarrow{\boldsymbol{D}}^p\right) \\ &= \frac{d}{dt}\left({}^t\underleftarrow{\boldsymbol{B}}_s + \Delta t\,{}^{t+\Delta t}H\,{}^t\mathbb{H} : {}^{t+\Delta t}\underleftarrow{\boldsymbol{D}}^p\right) \\ &= \left({}^{t+\Delta t}H + \Delta t\,{}^{t+\Delta t}\dot{H}\right){}^t\mathbb{H} : {}^{t+\Delta t}\underleftarrow{\boldsymbol{D}}^p + \Delta t\,{}^{t+\Delta t}H\,{}^t\mathbb{H} : {}^{t+\Delta t}\underleftarrow{\dot{\boldsymbol{D}}}^p \end{aligned} \tag{C.34}$$

Now the only unknown value is ${}^{t+\Delta t}\underleftarrow{\dot{\boldsymbol{D}}}^p$. From Eq. (C.25),

$$\begin{aligned} {}^{t+\Delta t}\underleftarrow{\dot{\boldsymbol{D}}}^p &= \frac{d}{dt}\left[\frac{3}{{}^{t+\Delta t}\kappa^2}\,{}^t\mathbb{A}^p_s : \left({}^{t+\Delta t}\underleftarrow{\boldsymbol{\Xi}}_s - {}^{t+\Delta t}\underleftarrow{\boldsymbol{B}}_s\right)\right] \\ &= -\frac{6}{{}^{t+\Delta t}\kappa^3}\,{}^{t+\Delta t}\dot{\kappa}\,{}^t\mathbb{A}^p_s : \left({}^{t+\Delta t}\underleftarrow{\boldsymbol{\Xi}}_s - {}^{t+\Delta t}\underleftarrow{\boldsymbol{B}}_s\right) \\ &\quad + \frac{3}{{}^{t+\Delta t}\kappa^2}\,{}^t\mathbb{A}^p_s : \left({}^{t+\Delta t}\underleftarrow{\dot{\boldsymbol{\Xi}}}_s - {}^{t+\Delta t}\underleftarrow{\dot{\boldsymbol{B}}}_s\right) \end{aligned} \tag{C.35}$$

Subtracting Eq. (C.34) from Eq. (C.33) yields

$$\begin{aligned} {}^{t+\Delta t}\dot{\underleftarrow{\boldsymbol{\Xi}}}_s - {}^{t+\Delta t}\dot{\underleftarrow{\boldsymbol{B}}}_s = & -\left[{}^t\mathbb{A} + \left({}^{t+\Delta t}H + \Delta t\,{}^{t+\Delta t}\dot{H}\right){}^t\mathbb{H}\right] : {}^{t+\Delta t}\underleftarrow{\boldsymbol{D}}^p \\ & - \Delta t\left({}^t\mathbb{A} + {}^{t+\Delta t}H\,{}^t\mathbb{H}\right) : {}^{t+\Delta t}\dot{\underleftarrow{\boldsymbol{D}}}^p \end{aligned} \tag{C.36}$$

Finally by solving Eqs. (C.35) and Eq. (C.36), we can compute ${}^{t+\Delta t}\dot{\underleftarrow{\boldsymbol{\Xi}}}_s - {}^{t+\Delta t}\dot{\underleftarrow{\boldsymbol{B}}}_s$ and consequently we can obtain ${}^{t+\Delta t}\dot{f}_s$ and Δt^{new}.

5. Compute the skew part and update variables.

   Using ${}^{t+\Delta t}\underleftarrow{\boldsymbol{D}}^p$ given in Eq. (C.29), we can update

$$\begin{aligned} {}^{t+\Delta t}\zeta &= {}^t\zeta + \Delta\zeta && \text{(C.37)} \\ {}^{t+\Delta t}\underleftarrow{\boldsymbol{\Xi}}_s &\simeq {}^{t+\Delta t}\underleftarrow{\boldsymbol{T}} = {}^{t+\Delta t}\underleftarrow{\mathbb{A}} : {}^{t+\Delta t}_{\;\;0}\underleftarrow{\boldsymbol{E}}^e = {}^t\mathbb{A} : \left(\underleftarrow{\boldsymbol{E}}^e_* - \Delta t\,{}^{t+\Delta t}\underleftarrow{\boldsymbol{D}}^p\right) && \text{(C.38)} \\ {}^{t+\Delta t}\underleftarrow{\boldsymbol{B}}_s &= {}^t\underleftarrow{\boldsymbol{B}}_s + \Delta t\,{}^{t+\Delta t}H\,{}^{t+\Delta t}\underleftarrow{\mathbb{H}} : {}^{t+\Delta t}\underleftarrow{\boldsymbol{D}}^p && \text{(C.39)} \\ &= {}^t\underleftarrow{\boldsymbol{B}}_s + \Delta t\,{}^{t+\Delta t}H\,{}^t\mathbb{H} : {}^{t+\Delta t}\underleftarrow{\boldsymbol{D}}^p \\ {}^{t+\Delta t}\tau &= \boldsymbol{R}^e_*\,{}^{t+\Delta t}\underleftarrow{\boldsymbol{T}}\,\boldsymbol{R}^{eT}_* = \boldsymbol{R}^e_*\,{}^{t+\Delta t}\underleftarrow{\boldsymbol{\Xi}}_s\boldsymbol{R}^{eT}_* && \text{(C.40)} \end{aligned}$$

   Then for the skew part, we can calculate

$$\begin{aligned} {}^{t+\Delta t}\underleftarrow{\boldsymbol{\Xi}}_w &= {}^{t+\Delta t}\underleftarrow{\boldsymbol{T}}_w = {}^{t+\Delta t}_{\;\;0}\underleftarrow{\boldsymbol{E}}^e\,{}^{t+\Delta t}\underleftarrow{\boldsymbol{T}} - {}^{t+\Delta t}\underleftarrow{\boldsymbol{T}}\,{}^{t+\Delta t}_{\;\;0}\underleftarrow{\boldsymbol{E}}^e && \text{(C.41)} \\ {}^{t+\Delta t}f_w &= \left\|{}^{t+\Delta t}\underleftarrow{\boldsymbol{\Xi}}_w\right\| - \sqrt{2}\,{}^{t+\Delta t}\kappa_w && \text{(C.42)} \end{aligned}$$

   From Eq. (C.4),

$${}^{t+\Delta t}\underleftarrow{\boldsymbol{W}}^d = \frac{\sqrt{2}}{{}^{t+\Delta t}\kappa}\left(\frac{\langle f_w\rangle}{\eta}\right)^m \frac{{}^{t+\Delta t}\underleftarrow{\boldsymbol{\Xi}}_w}{\left\|{}^{t+\Delta t}\underleftarrow{\boldsymbol{\Xi}}_w\right\|} \tag{C.43}$$

   From Eqs. (3.28) and (3.29),

$$\begin{aligned} {}^{t+\Delta t}\underleftarrow{\boldsymbol{W}}^p &= \frac{1}{2}(1-\rho)\,{}^{t+\Delta t}\underleftarrow{\boldsymbol{W}}^d && \text{(C.44)} \\ {}^{t+\Delta t}\underleftarrow{\boldsymbol{W}}^A &= -\frac{1}{2}(1+\rho)\,{}^{t+\Delta t}\underleftarrow{\boldsymbol{W}}^d && \text{(C.45)} \end{aligned}$$

Therefore we have

$$\begin{aligned} {}^{t+\Delta t}_{t}\boldsymbol{R}^{w} &= {}^{t+\Delta t}_{t}\underleftarrow{\boldsymbol{R}}^{w} = \exp\left(\Delta t\, {}^{t+\Delta t}\underleftarrow{\boldsymbol{W}}^{p}\right) && \text{(C.46)} \\ {}^{t+\Delta t}_{t}\boldsymbol{R}^{A} &= {}^{t+\Delta t}_{t}\underleftarrow{\boldsymbol{R}}^{A} = \exp\left(\Delta t\, {}^{t+\Delta t}\underleftarrow{\boldsymbol{W}}^{A}\right) && \text{(C.47)} \end{aligned}$$

Finally we can update the principal directions and the plastic deformation gradient.

$${}^{t+\Delta t}\boldsymbol{p}_i = {}^{t+\Delta t}_{t}\boldsymbol{R}^{w}\, {}^{t+\Delta t}_{t}\boldsymbol{R}^{A}\, {}^{t}\boldsymbol{p}_i \qquad \text{(C.48)}$$

$$\begin{aligned} \left({}^{t+\Delta t}_{0}\boldsymbol{X}^{p}\right)^{-1} &= \left({}^{t}_{0}\boldsymbol{X}^{p}\right)^{-1} \exp\left(-\Delta t\, {}^{t+\Delta t}\boldsymbol{W}^{p}\right) \exp\left(-\Delta t\, {}^{t+\Delta t}\boldsymbol{D}^{p}\right) \\ &= \left({}^{t}_{0}\boldsymbol{X}^{p}\right)^{-1} \left({}^{t+\Delta t}_{t}\boldsymbol{R}^{w}\right)^{T} \exp\left(-\Delta t\, {}^{t+\Delta t}\boldsymbol{D}^{p}\right) && \text{(C.49)} \\ &= \left({}^{t}_{0}\boldsymbol{X}^{p}\right)^{-1} \exp\left(-\Delta t\, {}^{t+\Delta t}\underleftarrow{\boldsymbol{D}}^{p}\right) \left({}^{t+\Delta t}_{t}\boldsymbol{R}^{w}\right)^{T} \end{aligned}$$

Bibliography

[1] Lee PS and Bathe KJ. Development of MITC isotropic triangular shell finite elements. *Computers & Structures*, 82:945–962, 2004.

[2] Chapelle D and Bathe KJ. *The finite element analysis of shells - fundamentals.* Springer, 2003.

[3] Montáns FJ and Bathe KJ. *Towards a model for large strain anisotropic elasto-plasticity*, pages 13–36. Computational Plasticity. Onate E and Owen R eds. Springer-Verlag, 2007.

[4] Kim KH and Yin JJ. Evolution of anisotropy under plane stress. *Journal of the Mechanics and Physics of Solids*, 45:841–851, 1997.

[5] Choi Y, Walter ME, Lee JK, and Han C-S. Observations of anisotropy evolution and identification of plastic spin parameters by uniaxial tensile tests. *Journal of Mechanics of Materials and Structures*, 1:303–324, 2006.

[6] Bathe KJ. *Finite element procedures.* Prentice Hall, 1996.

[7] Dvorkin EN and Bathe KJ. A continuum mechanics based four-node shell element for general non-linear analysis. *Engineering Computations*, 1:133–144, 1984.

[8] Bathe KJ and Dvorkin EN. A formulation of general shell elements - the use of mixed interpolation of tensorial components. *International Journal for Numerical Methods in Engineering*, 22:697–722, 1986.

[9] Bathe KJ, Iosilevich A, and Chapelle D. An evaluation of the MITC shell elements. *Computers & Structures*, 75:1–30, 2000.

[10] Pitkäranta J. Mathematical and historical reflections on the lowest-order finite element models for thin structures. *Computers & Structures*, 81:895–909, 2003.

[11] Bucalem ML and Bathe KJ. Higher-order MITC general shell elements. *International Journal for Numerical Methods in Engineering*, 36:3729–3754, 1993.

[12] Bathe KJ, Lee PS, and Hiller JF. Towards improving the MITC9 shell element. *Computers & Structures*, 81:477–489, 2003.

[13] Chapelle D and Bathe KJ. The mathematical shell model underlying general shell elements. *International Journal for Numerical Methods in Engineering*, 48:289–313, 2000.

[14] Lee PS and Bathe KJ. Insight into finite element shell discretizations by use of the basic shell mathematical model. *Computers & Structures*, 83:69–90, 2005.

[15] Bischoff M and Ramm E. Shear deformable shell elements for large strains and rotations. *International Journal for Numerical Methods in Engineering*, 40:4427–4449, 1997.

[16] Hauptmann R and Schweizerhof K. A systematic development of 'solid-shell' element formulations for linear and non-linear analyses employing only displacement degrees of freedom. *International Journal for Numerical Methods in Engineering*, 42:49–69, 1998.

[17] El-Abbasi N and Meguid SA. A new shell element accounting for through-thickness deformation. *Computer Methods in Applied Mechanics and Engineering*, 189:841–862, 2000.

[18] Klinkel S, Gruttmann F, and Wagner W. A robust non-linear solid-shell element based on a mixed variational formulation. *Computer Methods in Applied Mechanics and Engineering*, 195:179–201, 2006.

[19] Chapelle D, Ferent A, and Bathe KJ. 3D-Shell elements and their underlying mathematical model. *Mathematical Models and Methods in Applied Sciences*, 14:105–142, 2004.

[20] Wall WA, Gee M, and Ramm E. The challenge of a three-dimensional shell formulation - the conditioning problem. *Computational Methods for Shell and Spatial Structures, IASS-IACM*, 2000.

[21] Chapelle D, Mardare C, and Munch A. Asymptotic considerations shedding light on incompressible shell models. *Journal of Elasticity*, 76:199–246, 2004.

[22] Fontes Valente RA, Alves de Sousa RJ, and Natal Jorge RM. An enhanced strain 3D element for large deformation elastoplastic thin-shell applications. *Computational Mechanics*, 34:38–52, 2004.

[23] Vu-Quoc L and Tan XG. Optimal solid shells for non-linear analyses of multilayer composites - I. Statics. *Computer Methods in Applied Mechanics and Engineering*, 192:975–1016, 2003.

[24] Wriggers P and Reese S. A note on enhanced strain methods for large deformations. *Computer Methods in Applied Mechanics and Engineering*, 135:201–209, 1996.

[25] Pantuso D and Bathe KJ. On the stability of mixed finite elements in large strain analysis of incompressible solids. *Finite Elements in Analysis and Design*, 28:83–104, 1997.

[26] Toscano RG and Dvorkin EN. A shell element for finite strain analyses: Hyperelastic material models. *Engineering Computations*, 24:514–535, 2007.

[27] Bathe KJ. Adina system. *Encyclopedia of Mathematics, www.adina.com*, 11:33–35, 1997.

[28] Betsch P and Stein E. An assumed strain approach avoiding artificial thickness straining for a non-linear 4-node shell element. *Communications in Numerical Methods in Engineering*, 11:899–909, 1995.

[29] Chapelle D, Ferent A, and Tallec PL. The treatment of pinching locking in 3D-shell elements. *Mathematical Modeling and Numerical Analysis*, 37:143–158, 2003.

[30] Sussman T and Bathe KJ. A finite element formulation for nonlinear incompressible elastic and inelastic analysis. *Computers & Structures*, 26:357–409, 1987.

[31] Bathe KJ. The inf-sup condition and its evaluation for mixed finite element methods. *Computers & Structures*, 79:243–252, 2001.

[32] Sussman T and Bathe KJ. Studies of finite element procedures - On mesh selection. *Computers & Structures*, 21:257–264, 1985.

[33] Pantuso D and Bathe KJ. A four-node quadrilateral mixed-interpolated element for solids and fluids. *Mathematical Models and Methods in Applied Sciences*, 5:1113–1128, 1995.

[34] Lovadina C. Analysis of strain-pressure finite element methods for the Stokes problem. *Numerical Methods for Partial Differential Equations*, 13:717–730, 1997.

[35] Chapelle D and Bathe KJ. Fundamental considerations for the finite element analysis of shell structures. *Computers & Structures*, 66:19–36, 1998.

[36] Hiller JF and Bathe KJ. Measuring convergence of mixed finite element discretizations: An application to shell structures. *Computers & Structures*, 81:639–654, 2003.

[37] Montáns FJ and Bathe KJ. Computational issues in large strain elasto-plasticity: An algorithm for mixed hardening and plastic spin. *International Journal for Numerical Methods in Engineering*, 63:159–196, 2005.

[38] Bischoff JE, Arruda EM, and Grosh K. A rheological network model for the continuum anisotropic and viscoelastic behavior of soft tissue. *Biomechanics and Modeling in Mechanobiology*, 3:56–65, 2004.

[39] Zhang Y, Dunn ML, Drexler ES, McCowan CN, Slifca AJ, Ivy DD, and Shandas R. A microstructural hyperelastic model of pulmonary arteries under normo- and hypertensive conditions. *Annals of Biomedical Engineering*, 33:1042–1052, 2005.

[40] Lee PS, Noh HC, and Bathe KJ. Insight into 3-node triangular shell finite elements: the effects of element isotropy and mesh patterns. *Computers & Structures*, 85:404–418, 2007.

[41] Bathe KJ. *The finite element method*, pages 1253–1264. Chapter in Encyclopedia of Computer Science and Engineering, Wah E(ed.). J. Wilely and Sons, 2009.

[42] Bucalem ML and Bathe KJ. Finite element analysis of shell structures. *Archives of Computational Methods in Engineering*, 4:3–61, 1997.

[43] Kim DN and Bathe KJ. A 4-node 3D-shell element to model shell surface tractions and incompressible behavior. *Computers & Structures*, 86:2027–2041, 2008.

[44] Bathe KJ, Iosilevich A, and Chapelle D. An inf-sup test for shell finite elements. *Computers & Structures*, 75:439–456, 2000.

[45] Bathe KJ and Dvorkin EN. A four-node plate bending element based on Mindlin/Reissner plate theory and a mixed interpolation. *International Journal for Numerical Methods in Engineering*, 21:367–383, 1985.

[46] Brezzi F, Bathe KJ, and Fortin M. Mixed-interpolated elements for Reissner/Mindlin plates. *International Journal for Numerical Methods in Engineering*, 28:1787–1801, 1989.

[47] Bathe KJ, Brezzi F, and Cho SW. The MITC7 and MITC9 plate bending elements. *Computers & Structures*, 32:797–814, 1989.

[48] Iosilevich A, Bathe KJ, and Brezzi F. On evaluating the inf-sup condition for plate bending elements. *International Journal for Numerical Methods in Engineering*, 40:3639–3663, 1997.

[49] Lyly M, Niiranen J, and Stenberg R. A refined error analysis of MITC plate elements. *Mathematical Models and Methods in Applied Sciences*, 16:967–977, 2006.

[50] Lyly M, Niiranen J, and Stenberg R. Superconvergence and postprocessing of MITC plate elements. *Computer Methods in Applied Mechanics and Engineering*, 196:3110–3126, 2007.

[51] Beirao da Veiga L, Chapelle D, and Paris Suarez I. Towards improving the MITC6 triangular shell element. *Computers & Structures*, 85:1589–1610, 2007.

[52] Chapelle D and Paris Suarez I. Detailed reliability assessment for triangular MITC elements for thin shells. *Computers & Structures*, 86:2192–2202, 2008.

[53] Simo J and Rifai MS. A class of mixed assumed strain methods and the method of incompatible modes. *International Journal for Numerical Methods in Engineering*, 29:1595–1638, 1990.

[54] Wilson EL and Ibrahimbegovic A. Use of incompatible displacement modes for the calculation of element stiffness and stresses. *Finite Elements in Analysis and Design*, 7:229–241, 1990.

[55] Güzey S, Stolarski HK, Cockburn B, and Tamma KK. Design and development of a discontinuous Galerkin method for shells. *Computer Methods in Applied Mechanics and Engineering*, 195:3528–3548, 2006.

[56] Güzey S, Cockburn B, and Stolarski HK. The embedded discontinuous Galerkin method: application to linear shell problems. *International Journal for Numerical Methods in Engineering*, 70:757–790, 2007.

[57] Pitkäranta J and Sanchez Palencia E. On the asymptotic behavior of sensitive shells with small thickness. *Comptes Rendus de l'Academie des Sciences Serie II Fascicule B-Mechanique Physique Chimie*, 325:127–134, 1997.

[58] Kojić M and Bathe KJ. *Inelastic analysis of solids and structures.* Berlin: Springer, 2005.

[59] Bathe KJ and Montáns FJ. On modeling mixed hardening in computational plasticity. *Computers & Structures*, 82:535–539, 2004.

[60] Eterović AL and Bathe KJ. A hyperelastic-based large strain elasto-plastic constitutive formulation with combined isotropic-kinematic hardening using logarithmic stress and strain measures. *International Journal for Numerical Methods in Engineering*, 30:1099–1115, 1990.

[61] Lee EH. Elastic-plastic deformations at finite strains. *Journal of Applied Mechanics*, 36:1–6, 1967.

[62] Weber G and Anand L. Finite deformation constitutive equations and time integration procedure for isotropic hyperelastic-viscoelastic solids. *Computer Methods in Applied Mechanics and Engineering*, 79:173–202, 1990.

[63] Bathe KJ, Ramm E, and Wilson EL. Finite element formulations for large deformation dynamic analysis. *International Journal for Numerical Methods in Engineering*, 9:353–386, 1975.

[64] Snyder MD and Bathe KJ. A solution procedure for thermo-elastic-plastic and creep problems. *Nuclear Engineering and Design*, 64:49–80, 1981.

[65] Simó JC and Ortiz M. A unified approach to finite deformation elastoplasticity based on the use of hyperelastic constitutive equations. *Computer Methods in Applied Mechanics and Engineering*, 49:221–245, 1985.

[66] Simó JC and Hughes TJR. *Computational Inelasticity.* New York: Springer-Verlag, 1998.

[67] Kojić M and Bathe KJ. Studies of finite element procedures - Stress solution of a closed elastic strain path with stretching and shearing using the updated Lagrangian Jaumann formulation. *Computers & Structures*, 26:175–179, 1987.

[68] Gabriel G and Bathe KJ. Some computational issues in large strain elasto-plastic analysis. *Computers & Structures*, 56:249–267, 1995.

[69] Anand L. On H. Hencky's approximate strain-energy function for moderate deformations. *Journal of Applied Mechanics*, 46:78–82, 1979.

[70] Anand L. Moderate deformations in extension-torsion of incompressible isotropic elastic materials. *Journal of the Mechanics and Physics of Solids*, 34:293–304, 1986.

[71] Papadopoulus P and Lu J. A general framework for the numerical solution of problems in finite elasto-plasticity. *Computer Methods in Applied Mechanics and Engineering*, 159:1–18, 1998.

[72] Miehe C, Apel N, and Lambrecht M. Anisotropic additive plasticity in the logarithmic strain space: modular kinematic formulation and implementation based on incremental minimization principles for standard materials. *Computer Methods in Applied Mechanics and Engineering*, 191:5383–5426, 2002.

[73] Eidel B and Gruttmann F. *On the theory and numerics of orthotropic elasto-plasticity at finite plastic strains*, pages 246–248. Computational Fluid and Solid Mechanics, Bathe KJ(ed.). Oxford: Elsevier, 2003.

[74] Han CS, Choi Y, Lee JK, and Wagoner RH. A FE formulation for elasto-plastic materials with planar anisotropic yield functions and plastic spin. *International Journal of Solids and Structures*, 39:5123–5141, 2002.

[75] Han CS, Chung K, Wagoner RH, and Oh SI. A multiplicative finite elasto-plastic formulation with anisotropic yield functions. *International Journal of Plasticity*, 19:197–211, 2003.

[76] Menzel A and Steinmann P. On spatial formulation of anisotropic multiplicative elasto-plasticity. *Computer Methods in Applied Mechanics and Engineering*, 192:3431–3470, 2003.

[77] Haupt P and Kersten Th. On the modelling of anisotropic material behavior in viscoplasticity. *International Journal of Plasticity*, 19:1885–1915, 2003.

[78] Wu PD, Neale KW, and Van der Giessen E. Simulation of the behaviour of FCC polycrystals during reversed torsion. *International Journal of Plasticity*, 12:1199–1219, 1996.

[79] Sansour C, Karsaj I, and Soric J. On anisotropic flow rules in multiplicative elastoplasticity at finite strains. *Computer Methods in Applied Mechanics and Engineering*, 196:1264–1309, 2007.

[80] Schmidt I. Some comments on formulations of anisotropic plasticity. *Computational Materials Science*, 32:518–523, 2000.

[81] Kowalewski ZL and Sliwowski M. Effect of cyclic loading on the yield surface evolution of 18G2A low-alloy steel. *International Journal of Mechanical Sciences*, 39:51–68, 1997.

[82] Bunge HJ and Nielsen I. Experimental determination of plastic spin in polycrystalline materials. *International Journal of Plasticity*, 13:435–446, 1997.

[83] Truong Qui HK and Lippmann H. Plastic spin and evolution of an anisotropic yield condition. *International Journal of Mechanical Sciences*, 43:1969–1983, 2001.

[84] Boheler JP and Koss S. *Evolution of anisotropy in sheet steels subjected to off-axes large deformation.* Advances in Continuum Mechanics, Brueler O, Mannl V and Najar J (eds.). Berlin; Springer, 1991.

[85] Bunge HJ. *Texture Analysis in Materials Science.* Butterworths, 1982.

[86] Kocks U, Tomé C, and Wenk H. *Texture and Anisotropy.* Cambridge University Press, 1998.

[87] Peeters B, Hoferlin E, Van Houtte P, and Aernouldt E. Assessment of crystal plasticity based calculation of the lattice spin of polycrystalline metals for FE implementation. *International Journal of Plasticity*, 17:819–836, 2001.

[88] Van Houtte P, Li S, Seefeldt M, and Delannay L. Deformation texture prediction: from Taylor model to the advanced Lamel model. *International Journal of Plasticity*, 21:589–624, 2005.

[89] Buchheit TE, Wellman GW, and Battaile CC. Investigating the limits of polycrystal plasticity modeling. *International Journal of Plasticity*, 21:221–249, 2005.

[90] Nakamachi E, Tam NN, and Morimoto H. Multiscale finite element analysis of sheet metals by using SEM-EBSD measured crystallographic RVE models. *International Journal of Plasticity*, 23:450–489, 2007.

[91] Duchene L, Houdaigui F, and Habraken AM. Length changes and texture prediction during free end torsion test of copper bars with FEM and remeshing techniques. *International Journal of Plasticity*, 23:1417–1438, 2007.

[92] Raabe D and Roters F. Using texture in crystal plasticity finite element simulations. *International Journal of Plasticity*, 20:339–361, 2004.

[93] Raabe D, Wang Y, and Roters F. Crystal plasticity simulation study on the influence of texture on earing in steel. *Computational Materials Science*, 34:221–234, 2005.

[94] Delaire F, Raphanel JL, and Rey C. Plastic heterogeneities of a copper multicrystal deformed in uniaxial tension: Experimental study and finite element simulations. *Acta Materialia*, 48:1075–1087, 2000.

[95] Choi Y, Han C-S, Lee JK, and Wagoner RH. Modeling multi-axial deformation of planar anisotropic elasto-plastic materials, part i: Theory. *International Journal of Plasticity*, 22:1745–1764, 2006.